

DISS. ETH NO. 22154

A Self-Consistent Particle-In-Cell Time-Domain Solver Incorporating Radiative Interaction

A dissertation submitted to
ETH ZURICH

for the degree of
DOCTOR OF SCIENCES

presented by
CHRISTOF JOHAN METZGER
Dipl. Phys. ETH
born October 1st, 1978
citizen of Meilen ZH

accepted on the recommendation of
Prof. Dr. Peter Arbenz, examiner
Prof. Dr. Klaus Kirch, co-examiner
Prof. Dr. Christoph Pflaum, co-examiner
Dr. Andreas Adelmann, co-examiner

Abstract

Charged particles that are accelerated emit electromagnetic waves. This effect grows stronger the faster the particles become and the stronger they are accelerated. The production of synchrotron radiation as these electromagnetic waves are called is the sole aim of some particle accelerators. Mostly electrons are used for this purpose since less energy is needed to accelerate light particles to high speeds compared to heavy particles. Current particle accelerators for the production of synchrotron radiation have a circular shape. The particles are first accelerated to high speeds and then injected into the so called storage ring where the electrons spin around many times. There is not a constant particle flow but instead they are grouped in small bunches with some distance between bunches. A particle moves on a straight path if no force is applied on it. Thus it has to be accelerated to keep it on a circular path. A storage ring doesn't have the shape of a perfect circle but consists of many bends and straight sections in-between.

Next generation synchrotron light sources require a particle beam with higher quality to produce coherent synchrotron radiation. The machines are designed in such a way that a high particle density is gained at the end of the machine in order to increase the production of synchrotron radiation. However charged particles at low kinetic energies tend to repulse each other strongly. This prevents the generation of a high particle density at the beginning of the machine. Therefore so called bunch compressors are inserted. They consist of several dipole magnets that force the particles on paths that depend on their kinetic energy. The

faster a particle is the shorter is its path. A compression of the bunch can be achieved with clever distribution of the energies within the bunch.

The disadvantage of this bunch compressors is that the particles emit synchrotron radiation when they are forced from their straight path. Particles ahead will then interact with this radiation. Even coherent synchrotron radiation can occur in these compressors if certain criteria are met. However the action of coherent radiation on the quality of the beam is much more severe. In the design of such machines one aims at suppressing coherent radiation in order to deliver the required quality at the end of the machine. For this purpose specialized simulation tools exist but all have constraints.

The difficulty for the simulation of radiative interaction is the fact that the emission of electromagnetic radiation and the interaction with it are not simultaneous. Furthermore the size of one particle bunch is in the order of micrometers while the total length of a bunch compressors is in the range of ten meters. Thus a simulation code has to allow for huge difference in scales. The original aim of this thesis was to develop a self-consistent 3-dimensional code that updates the electromagnetic fields using a finite-difference time-domain (FDTD) method. It became soon evident that this goal is too ambitious. Instead a 2-dimensional code was developed which serves as a good basis for further development towards the original goal. We discuss different strategies for the parallelization of both particles and fields. We also compare timings and discuss the results with respect to future development.

The reduction to two dimensions has the disadvantage that the electromagnetic fields behave differently than in three dimensions. For validation a second code was developed since for the two dimensional case no other code exists to compare results with. This second code is based on the Liénard-Wiechert potential formulation. It is not self-consistent and does not simulate individual particles but a rigid charge distribution. This approach is easy enough to implement, yields results fast enough and is not directly connected to the first method to serve its purpose. We show that the results match well up to small differences.

Finally we compare results with a code that has a simple solver for the 3-dimensional case incorporated although we know that the fields behave differently in two dimensions. Not surprisingly we find that the solutions differ considerably.

Zusammenfassung

Geladene Teilchen, die beschleunigt werden, emittieren elektromagnetische Wellen. Dieser Effekt wird stärker je schneller die Teilchen werden und je stärker die Beschleunigung ist. Die Produktion von Synchrotronstrahlung, wie diese elektromagnetischen Wellen genannt werden, ist die einzige Aufgabe einiger Teilchenbeschleuniger. Meist werden Elektronen für diesen Zweck eingesetzt, da weniger Energie benötigt wird um leichte statt schwere Teilchen zu beschleunigen. Teilchenbeschleuniger, die zur Zeit für die Produktion von Synchrotronstrahlung eingesetzt werden, haben eine runde Form. Die Teilchen werden zuerst auf hohe Geschwindigkeiten beschleunigt und dann in den sogenannten Speicherring eingeschossen, wo die Teilchen lang herum kreisen. Statt eines konstanten Teilchenstroms werden die Teilchen in kleine Pakete formiert, die einen gewissen Abstand haben zum nächsten Paket. Wenn keine Kraft auf ein Teilchen ausgeübt wird, dann fliegt es geradeaus. Es muss daher beschleunigt werden, damit es auf einer kreisförmigen Bahn fliegt. Ein Speicherring ist also nicht ein perfekter Kreis sondern besteht aus vielen kreisförmigen Segmenten mit geraden Stücken dazwischen.

Synchrotronlichtquellen der nächsten Generation benötigen Teilchenströme von viel besserer Qualität um kohärente Synchrotronstrahlung zu produzieren. Die Maschinen werden so geplant, dass am Ende der Maschine eine hohe Teilchendichte entsteht, um damit die Produktion von Synchrotronstrahlung zu verstärken. Geladene Teilchen tendieren jedoch dazu sich gegenseitig abzustossen, was eine Produktion hoher Teilchendichten am Anfang der Maschinen verhindert. Deshalb werden sogenannte magnetische Schikanen,

die den Teilchenpuls komprimieren, in die Maschine eingebaut. Sie bestehen aus mehreren Dipolmagneten, die die Teilchen auf Bahnen ablenken, die von der kinetischen Energie abhängen. Je schneller ein Teilchen ist, desto kürzer ist der Weg, den es zurücklegen muss. Mit einer klugen Energieverteilung innerhalb des Pulses kann eine Kompression erzeugt werden.

Der Nachteil dieser Magnetschikanen liegt darin, dass die geladenen Teilchen Synchrotronstrahlung emittieren, wenn sie vom geraden Pfad abgelenkt werden, und Teilchen davor werden mit der Strahlung wechselwirken. Unter gewissen Umständen kann sogar kohärente Synchrotronstrahlung auftreten, die einen viel schwerwiegenderen Einfluss auf die Qualität des Teilchenstroms hat. Beim Entwurf solcher Maschinen wird daher versucht kohärente Synchrotronstrahlung zu unterdrücken, damit der Teilchenstrom am Ende der Maschine die benötigte Qualität aufweist. Zur Unterstützung stehen spezialisierte Werkzeuge für die Simulation zur Verfügung, alle haben jedoch Einschränkungen.

Die Schwierigkeit bei der Simulation von Interaktion mittels Strahlung liegt darin, dass der Zeitpunkt der Emission nicht mit dem Zeitpunkt der Interaktion zusammenfällt. Des weiteren weist der Teilchenpuls eine Ausdehnung im Bereich von Mikrometern auf, während die ganze Schikane eine Länge im Bereich von zehn Metern aufweist. Ein Code muss daher Simulationen mit sehr grossen Skalenunterschieden zulassen. Die Absicht dieser Dissertation war es, einen in sich konsistenten dreidimensionalen Code zu entwickeln, der die Felder mit einer Finitendifferenzen Methode im Zeitbereich aufdatiert. Es wurde bald klar, dass dieses Ziel zu ambitioniert war. Stattdessen wurde ein zweidimensionaler Code entwickelt der sich gut eignet für die Weiterentwicklung hin zum ursprünglichen Ziel. Zu diesem Zweck stellen wir verschiedene Strategien zur Parallelisierung von sowohl Teilchen wie auch Feldern. Ebenso werden diese Strategien miteinander verglichen bezüglich Zeitverbrauch.

Die Reduktion auf zwei Dimension hat allerdings den Nachteil, dass sich die Felder anders verhalten als im dreidimensionalen Fall. Da keine weiterer zweidimensionaler Code existiert, mit dem die Resultate hätten verglichen werden können, wurde zusätzlich ein Code zur Validierung entwickelt. Dieser zweite Code basiert auf der Formulierung der Liénard-Wiechert Potentialen. Er ist nicht in sich konsistent und er simuliert nicht einzelne Teilchen sondern eine unverformbare Ladungsverteilung. Dieser Ansatz ist einfach genug umzusetzen, liefert schnell Resultate und ist genug verschieden von der ersten Methode um seinen Zweck zu erfüllen. Wir zeigen, dass die Resultate bis auf kleine Abweichungen gut übereinstimmen.

Schlussendlich vergleichen wir Resultate mit einem Code der einen einfachen Löser für den dreidimensionalen Fall zur Verfügung stellt, obwohl wir wissen, dass sich die Felder verschieden verhalten. Die Resultate unterscheiden sich dann auch in erheblichem Mass, was nicht weiter überrascht.

Acknowledgment

I would like to thank my supervisors Andreas Adelmann and Peter Arbenz for their continuous support and scientific advise. This dissertation would not have been possible without their support, understanding and encouragement.

Notation

Vectors, Fields, Operators

$h, \tilde{\phi}_{i,j}$	scalars
$\mathbf{e}, \tilde{\mathbf{E}}_{i,j}$	vectors
\mathcal{M}	a matrix
$\tilde{\rho}, \tilde{\phi}$	continuous or discrete scalar fields
$\tilde{\mathbf{E}}, \tilde{\mathbf{B}}, \tilde{\mathbf{J}}$	continuous or discrete vector fields
$a = \mathbf{b} \cdot \mathbf{d}$	the scalar product of two vectors
$\mathbf{a} = \mathbf{b} \times \mathbf{d}$	the vector product of two vectors
$\tilde{\mathbf{a}} = \nabla \tilde{b}$	the gradient of a scalar field
$\tilde{\mathbf{a}} = \nabla \times \tilde{\mathbf{b}}$	the curl of a vector field
$\tilde{a} = \nabla \cdot \tilde{\mathbf{b}}$	the divergence of a vector field
$\tilde{a} = \Delta \tilde{b} = \nabla \cdot \nabla \tilde{b}$	the Laplacian of a scalar field
$\mathrm{d}_t X = \frac{\mathrm{d}X}{\mathrm{d}t}$	total derivative of X with respect to t
$\partial_t X = \frac{\partial X}{\partial t}$	partial derivative of X with respect to t

Physics Abbreviations

$\beta = v/c$	a velocity normalized by the speed of light in vacuum
$\gamma = \sqrt{1/(1-\beta^2)}$	the relativistic factor

Constants

ϵ_0	vacuum permittivity
μ_0	vacuum permeability
$c = 1/\sqrt{\epsilon_0 \cdot \mu_0}$	the speed of light in vacuum
$Z_0 = \sqrt{\mu_0/\epsilon_0}$	vacuum impedance
$i = \sqrt{-1}$	imaginary unit

Other Abbreviations

$\eta_\nu = \frac{c\Delta t}{\Delta\nu}$	ratio between covered distance by light in one time step and grid cell dimension
$\mathbb{N}^+ = \{1, 2, 3, \dots\}$	set of positive integers

Contents

1	Introduction	1
1.1	Particle Accelerators	1
1.1.1	Relativistic Effects	3
1.1.2	Beam Dynamics	5
1.1.3	Synchrotron Radiation	6
1.1.4	X-Ray Free Electron Lasers	12
1.2	Computational Particle Dynamics	16
1.3	Goal of Thesis	20
2	Initial Conditions	23
2.1	Simple Geometries	28
2.1.1	Boundary Conditions	29
2.2	Complicated Geometries	33
2.2.1	Boundary Conditions	33
3	Propagation of Particles	37
3.1	Interpolation of Electromagnetic Fields	37
3.2	Temporal Integration	39
3.2.1	Störmer-Verlet Method	40
3.2.2	Symplectic Runge-Kutta Methods	41
3.3	Calculation of Current	42
3.3.1	Enforcing Gauss's Law	42
3.3.2	Charge Conserving Current	43
4	Finite-Difference Time-Domain	47
4.1	Yee Scheme	48
4.2	Alternating-Direction Implicit Schemes	52
4.2.1	Divergence Preserving Scheme	54
4.3	TE/TM Schemes	57
4.3.1	Implicit Scheme	57
4.3.2	Explicit Scheme	60
4.4	Boundary Conditions	62
4.4.1	Perfect Electric Conductor	62
4.4.2	Absorbing Boundary Conditions	64
5	Implementation	67
5.1	Parallelization	68
5.2	Geometry and Boundary Conditions	72
5.3	Poisson Solver	74
5.4	Particle Bunch	75
5.5	Output	76

6 Results	79
6.1 Validation	79
6.2 Scalability	97
6.3 Application to Simple Bend	101
7 Conclusions	103
A Appendices	107
A.1 Dispersion Relation of Divergence Preserving ADI	107
A.2 Installation	109
A.3 Run Examples	111
Bibliography	113

Chapter One

Introduction

The goal of this work is to develop a better computational model for the simulation of magnetic bunch compressors in free electron lasers (FELs). This first chapter will give a short introduction to particle accelerators and FELs in particular and the the simulation thereof. In the first section a few physical effects from *special relativity* will be briefly explained since at speeds close to the speed of light some laws of classical physics have to be revised. The phenomenon of radiating charged particles is studied in some detail including the property of coherence. This then leads to the introduction of FELs.

The scope of the second section the simulation of particle accelerators in general and of FELs in particular. The difficulty for simulations of retarded interaction is discussed and implementations of solutions to this problem are presented.

1.1 Particle Accelerators

As their name indicates particle accelerators are used to accelerate charged particles. The first accelerators were simple glass tubes with low air-pressure inside. In these so-called cathode ray tubes electrons are released and accelerated by applying a DC voltage between two metallic surfaces. To steer the beam electric or magnetic fields are used. The forces that

act on the particles are described by the Lorentz force,

$$\mathbf{F}_{\text{tot}}(\mathbf{r}, \mathbf{v}, t) = q \left(\tilde{\mathbf{E}}_{\text{tot}}(\mathbf{r}, t) + \mathbf{v} \times \tilde{\mathbf{B}}_{\text{tot}}(\mathbf{r}, t) \right) = m \frac{d\gamma \mathbf{v}}{dt}, \quad (1.1)$$

where q is the charge, \mathbf{r} is the position and \mathbf{v} is the velocity of the particle at time t and $\tilde{\mathbf{E}}_{\text{tot}} = \tilde{\mathbf{E}}_{\text{ext}} + \tilde{\mathbf{E}}_{\text{sc}}$ is the combination of external electric fields and the Coulomb repulsion of other particles, which is also called space charge. Finally $\tilde{\mathbf{B}}_{\text{tot}} = \tilde{\mathbf{B}}_{\text{ext}} + \tilde{\mathbf{B}}_{\text{ind}}$ is the combination of external magnetic fields and magnetic fields induced by other particles.

Static electric fields are not well suited to accelerate charged particles to high energies. Instead time-varying electromagnetic fields are used. The fields oscillate with a frequency such that only the accelerating half period of the electric field acts on the particles. As a consequence the current of particles is not constant but grouped into bunches. The distance between two bunches is at least one period long, often more. The electron sources have slightly changed as well. To increase the current in practice not only a voltage is applied to the cathodes but they are also either heated in thermionic cathodes or irradiated with a suitable laser in photocathodes. Instead of glass tubes metallic tubes are used to achieve a good vacuum inside. A good vacuum reduces the scattering of the accelerated particles with molecules in the air.

Static and oscillating electromagnetic fields to accelerate, steer and focus charged particles are still all the basic ingredients that are needed for a particle accelerator today. Of course there is more equipment needed to control the beams but the basic principles can be explained with these few ingredients.

Particle accelerators were originally invented to investigate the structure of matter. This is still one of the driving forces in this field. Large machines such as the Large Hadron Collider (LHC) at CERN near Geneva or the Tevatron at Fermilab near Chicago are devoted to investigate the smallest particles known today. Nowadays particle accelerators in various sizes are used for a broad spectrum of applications: from old television sets and computer displays, X-ray tubes at the dentists and the physicians, linear accelerators and so called cyclotrons in hospitals to large scale scientific facilities. In the following a short description of modern scientific accelerators is given:

Accelerators for Fixed-Target Experiments accelerate electrons, their anti-particles (positrons), ionized hydrogen atoms (protons and H^-) and other (heavier) ionized atoms. When the particles reach the energy the accelerator was designed for then they are shot at a target. This target can be cancer cells of a patient for radiotherapy or a solid, liquid or gaseous material. In the latter case the beam is used either to probe the characteristics of the target material itself or to produce other particles such as neutrons, muons, other elementary particles or various antiparticles. These new particles can then in turn be used to accelerate them further if they carry charge, to investigate their characteristics, or for research in material science.

The accelerators can be constructed in different ways. They range from relatively small circular shapes with diameters of a few meters or less to medium sized rings with circumferences of a few hundred meters or less. Finally there exist also a few linear accelerators in this field.

Particle Colliders accelerate two beams and have them collide. Compared to the fixed-target accelerators they reach much higher energies. Higher energies are needed

to produce heavier particles due to the mass-energy equivalence, $E = m c^2$, where E is the energy, m is the rest mass of the produced particle and c is the speed of light. The quest is the discovery of the particles that are predicted by theories and from which all matter and antimatter and their interactions are constituted.

The voltage along accelerating devices is limited due to voltage breakdown. Particle colliders therefore tend to be large machines and of circular shape. The LHC is the largest machine with a circumference of roughly 27 km.

Synchrotron Light Sources are used to produce strong electromagnetic radiation (light) in a broad spectrum. This radiation was first an undesired side effect of early circular electron accelerators, so called synchrotrons, because charged particles emit electromagnetic radiation when they are accelerated.

The particles lose energy when radiating which is why this was not desired in the beginning. But soon it was discovered that this light has some extraordinary properties such as its polarization, intensity and adjustability. Nowadays synchrotron light sources are built to investigate surfaces of crystalline materials. So far synchrotron sources were designed as rings where the particles are stored for hours in so-called storage rings. The latest development are Free Electron Lasers (FELs) which are linear accelerators with long undulators, a device that forces the electrons to oscillate in transverse direction, at the end. They produce very short but very intensive bursts of light. Light with these characteristics can be used to study new classes of materials in detail.

1.1.1 Relativistic Effects

While the laws of classical mechanics are perfectly valid for macroscopic and slowly moving objects they fail for the extremely fast particles as found in particle accelerators. To transform the mathematical description of physical phenomena in classical mechanics from one system to another system that is in constant linear motion relative to the first the Galilean transformation

$$\begin{aligned} t' &= t, \\ \mathbf{x}' &= \mathbf{x} - \mathbf{v} t, \end{aligned} \tag{1.2}$$

is applied, where t, t' are the times and \mathbf{x}, \mathbf{x}' are positions in the first and second system respectively and \mathbf{v} is the relative speed of the second to the first system. Though “*Maxwell's electrodynamics applied to moving bodies leads to asymmetries which do not seem to inhere in the phenomenon*” as Einstein stated it [1]. This led him to formulate two postulates,

- I. The laws of electrodynamics are valid in all coordinate systems in which also the laws of classical mechanics are valid,
- II. Light in empty space propagates with speed c independent of the state of motion of the emitting body,

which have profound consequences. Instead of the simple transformation (1.2) one gets the Lorentz transformation,

$$\begin{aligned} ct' &= \gamma(ct - \beta \cdot \mathbf{x}), \\ \mathbf{x}' &= \mathbf{x} + \frac{\gamma - 1}{\beta^2}(\beta \cdot \mathbf{x})\beta - \gamma\beta ct, \end{aligned} \quad (1.3)$$

where $\beta = v/c$, $\gamma = |\beta|$ and $\gamma = (1 - \beta^2)^{-1/2}$. This transformation is well approximated by (1.2) for speeds $v \ll c$. With (1.3) one cannot only show that Maxwell's equations,

$$\begin{aligned} \nabla \times \tilde{\mathbf{E}} &= -\frac{\partial \tilde{\mathbf{B}}}{\partial t}, & \nabla \cdot \tilde{\mathbf{E}} &= \frac{\tilde{\rho}}{\varepsilon_0}, \\ \nabla \times \tilde{\mathbf{B}} &= \mu_0 \tilde{\mathbf{J}} + \frac{1}{c^2} \frac{\partial \tilde{\mathbf{E}}}{\partial t}, & \nabla \cdot \tilde{\mathbf{B}} &= 0, \end{aligned} \quad (1.4)$$

with current density $\tilde{\mathbf{J}}$, charge density $\tilde{\rho}$, vacuum permittivity ε_0 and vacuum permeability μ_0 , keep their form in any system that is not accelerated but it also explains some important phenomena:

- o For an observer a clock in a system which is in constant linear motion to himself appears to run slower than his own clock. The time with which the clock ticks in the moving system is called its *proper time*. This effect can be measured [2] by comparing the number of muons which reach sea level with the number in higher altitudes.¹ Muons are produced by cosmic rays in the upper atmosphere and have a speed close to the speed of light. They decay through a radioactive process with a half-time of only 1.5 μs . Due to their proper time more particles reach sea level than what one would expect.
- o The *length contraction* is similar to the proper time but in 3-dimensional space. For an observer at rest the length of an object in constant linear motion appears to be shorter in the direction of motion than what a second, co-moving observer would measure. A direct verification of this effect with macroscopic objects is very hard to achieve since the speed has to be close to the speed of light for a measurable effect. Though there exist a few indications that the length contraction is valid.

In the context of particle accelerator design the following fact is of considerable importance. The longitudinal distance between two particles which are moving approximately in the same direction and with the same relativistic speed seems to be larger by a factor γ than what one measures in a system at rest. If the particles are charged then this leads to lower Coulomb rejections. An observer in a system in which the charged particles are moving measures not only an electric field. He measures also a magnetic field that seems to alleviate the repulsive force. By means of the Lorentz transformation one finds that the electric and magnetic fields are representations of the same phenomenon. They can be transformed into one another.

¹The muon is an elementary particle described by the *Standard Model* of physics. It is ~ 200 times heavier than the electron and has the same charge and spin.

- Finally the description of momentum and total energy of a moving particle in classical mechanics does not hold under Lorentz transformation. Though *relativistic momentum and energy* of a particle have to be well approximated for low speeds. With the help of a thought experiment on elastic scattering of particles [3, Sect. 11.5, p. 533] one finds

$$\begin{aligned} E &= \gamma m_0 c^2 \quad \text{and} \\ \mathbf{p} &= \beta \gamma m_0 \mathbf{c}, \end{aligned} \tag{1.5}$$

where $m_0 c^2$ is the rest energy of the particle, \mathbf{p} is the momentum and E is the total energy. The relativistic momentum and energy diverge to infinity as the speed of the particle converges to the speed of light. Therefore the speed a particle can gain is limited to the speed of light and it is always less if the particle carries mass.

1.1.2 Beam Dynamics

The particles in a bunch do not only interact with external fields and the space charge field but also with the surrounding vacuum tubes and possibly fields induced by neighboring bunches. The electric field on the surface of a perfectly conducting material has no transverse components. This is due to the infinitely high mobility of electrons in these materials. Any residual transverse electric field would cause the electrons to be pushed away, notably without resistance and hence energy loss. Real vacuum tubes are made of metals with relatively low but not vanishing electric resistance. The electrons on the surface of vacuum tubes lose energy to the atoms of the metal which scatter the electrons. This happens even in the case of superconducting tubes. This interaction heats up the material, thus the energy of the bunch is reduced due to energy conservation. The fields due to the finite conductivity and due to changes of the tube geometry are called wake fields. Wake fields cannot only reduce the mean energy of the bunch but also the energy distribution inside it. Particles at the head of a bunch can influence particles behind it. Furthermore wake fields can also excite electromagnetic modes inside cavities that last long enough such that following bunches are influenced.

A particle bunch is characterized by its 6-dimensional phase space composed of longitudinal and transverse charge and momentum distribution. An important measure for the quality of a beam is its normalized emittance, $\epsilon_{n,\eta}$ with components given by

$$\epsilon_{n,\eta} = \sqrt{\langle r_\eta^2 \rangle \langle p_\eta^2 \rangle - \langle r_\eta p_\eta \rangle^2}, \quad \eta = x, y, z, \tag{1.6}$$

where $\langle \cdot \rangle$ is the mean value over the bunch and \mathbf{r} , \mathbf{p} are the position and momentum respectively of a particle. The projected emittance is proportional to the area of the ellipsoid of phase space in the corresponding direction. To achieve a high brilliance and luminosity a low emittance is needed but transporting a low emittance from the source to the location where it is needed is challenging.

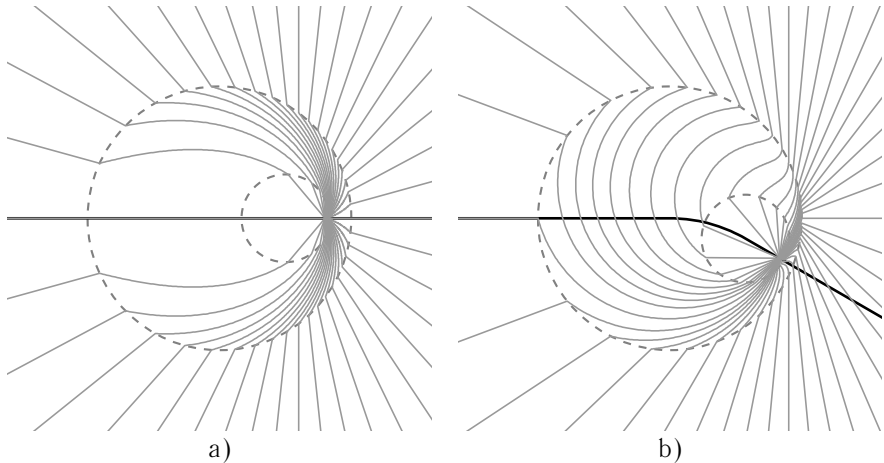


Figure 1.1: Visualization of a charged particle emitting an electromagnetic wave under a longitudinal and b) transverse acceleration, see also [4, 5]. The thick black lines are the paths of the particles, the thin solid gray lines are the electric field lines and the dashed lines are the horizons of the beginning and end of acceleration. To be correct the field lines should have a direction, either inward for a negative charge or outward for a positive charge. The field lines are computed using (1.10).

1.1.3 Synchrotron Radiation

Synchrotron radiation is produced by charged particles when they are accelerated. The reason why they emit electromagnetic waves is found in the finite speed of light. The electric field lines of a charged particle moving with constant velocity spread radially. They move in the same direction and with the same speed as the particle. If the particle is accelerated then this information does not spread instantaneously but with the speed of light. A circular horizon beyond which the information has not reached forms and expands with the speed of light. All field lines beyond the horizon point to the position where the particle would be if it hadn't been accelerated. This is depicted in Fig. 1.1 for a particle under longitudinal acceleration on the left hand side and under transverse acceleration on the right hand side. The thick black line in the figures are the paths of the particles. The outer circles are the horizons of the start of acceleration. The field lines beyond these horizons are straight. The inner circles are the horizons of the end of acceleration within which the field lines are also straight. Between the horizons the field lines are distorted. This causes energy to be transported in terms of radiation.

To derive a mathematical formula for the electromagnetic field of an accelerated charged

particle [3, Sect. 14.1] one has to transform the retarded vector and scalar potential

$$\begin{aligned}\tilde{\mathbf{A}}(\mathbf{r}, t) &= \frac{\mu_0}{4\pi} \int_{\Omega} \frac{\tilde{\mathbf{J}}(\mathbf{r}', t - |\mathbf{r} - \mathbf{r}'|/c)}{|\mathbf{r} - \mathbf{r}'|} d^3\mathbf{r}', \\ \tilde{\phi}(\mathbf{r}, t) &= \frac{1}{4\pi\epsilon_0} \int_{\Omega} \frac{\tilde{\rho}(\mathbf{r}', t - |\mathbf{r} - \mathbf{r}'|/c)}{|\mathbf{r} - \mathbf{r}'|} d^3\mathbf{r}'.\end{aligned}\quad (1.7)$$

From these potentials we then get the electromagnetic fields with

$$\begin{aligned}\tilde{\mathbf{E}} &= -\nabla \tilde{\phi} - \frac{\partial \tilde{\mathbf{A}}}{\partial t}, \\ \tilde{\mathbf{B}} &= \nabla \times \tilde{\mathbf{A}}.\end{aligned}\quad (1.8)$$

For a single particle the current and charge density are not continuous functions in space and time but delta functions which for any time are zero everywhere except at the position of the particle. With this in mind the potentials can be simplified to

$$\begin{aligned}\tilde{\mathbf{A}}(\mathbf{r}, t) &= \frac{\mu_0 c}{4\pi} \frac{q \beta_s}{(1 - \mathbf{n}_s \cdot \boldsymbol{\beta}_s) |\mathbf{r} - \mathbf{R}_s|}, \\ \tilde{\phi}(\mathbf{r}, t) &= \frac{1}{4\pi\epsilon_0} \frac{q}{(1 - \mathbf{n}_s \cdot \boldsymbol{\beta}_s) |\mathbf{r} - \mathbf{R}_s|},\end{aligned}\quad (1.9)$$

where q is the charge, $\mathbf{R}_s = \mathbf{R}(t_s)$ is the retarded position of the particle at time t_s in the past with the constraint that $c(t - t_s) = |\mathbf{r} - \mathbf{R}_s|$, $\boldsymbol{\beta}_s$ is the velocity of the particle at the retarded position and \mathbf{n}_s is the unit vector pointing from the retarded position to where the field is to be determined, $\mathbf{n}_s = \mathbf{r} - \mathbf{R}_s / |\mathbf{r} - \mathbf{R}_s|$. These potentials are called the *Liénard-Wiechert potentials*. For the electromagnetic field we then get

$$\begin{aligned}\tilde{\mathbf{E}}(\mathbf{r}, t) &= \frac{q}{4\pi\epsilon_0} \left(\frac{(\mathbf{n}_s - \boldsymbol{\beta}_s)}{\gamma^2 (1 - \mathbf{n}_s \cdot \boldsymbol{\beta}_s)^3 |\mathbf{r} - \mathbf{R}_s|^2} + \frac{\mathbf{n}_s \times ((\mathbf{n}_s - \boldsymbol{\beta}_s) \times \dot{\boldsymbol{\beta}}_s)}{c (1 - \mathbf{n}_s \cdot \boldsymbol{\beta}_s)^3 |\mathbf{r} - \mathbf{R}_s|} \right), \\ \tilde{\mathbf{B}}(\mathbf{r}, t) &= \frac{\mathbf{n}_s}{c} \times \tilde{\mathbf{E}}(\mathbf{r}, t),\end{aligned}\quad (1.10)$$

where $\dot{\boldsymbol{\beta}}_s$ is the acceleration of the particle at the retarded position. From the expression for the electric field we see that there are two terms inside the outer parentheses. In the first term the acceleration does not appear and it decays as the inverse of the distance squared. This is the velocity contribution to the field. The second term on the other hand vanishes if the charge is not accelerated. Furthermore for longer distances this term becomes dominant since its strength only decays as the inverse of the distance.

When applying the same accelerating force the radiation power of a relativistic charged particle accelerated in transverse direction is much stronger than for one accelerated in longitudinal direction. This can be quantified by integrating the Poynting vector,

$$\tilde{\mathbf{S}} = \mu_0^{-1} (\tilde{\mathbf{E}} \times \tilde{\mathbf{B}}), \quad (1.11)$$

over a closed surface containing the charged particle [6, Sect. 21.2]. For longitudinal acceleration one then gets

$$P_{\parallel} = \frac{q^2 c}{6\pi\epsilon_0} \frac{1}{(mc^2)^2} \left(\frac{d\mathbf{p}_{\parallel}}{dt} \right)^2, \quad (1.12)$$

with $d_t \mathbf{p}_{\parallel}$ the change of the momentum in longitudinal direction. The radiation of longitudinal accelerated particles for accelerators made with current technology is very weak. For a given particle (1.12) only depends on the applied force. In contrast for transverse acceleration the radiated power greatly depends on the speed of the particle:

$$P_{\perp} = \frac{q^2 c}{6\pi\epsilon_0} \frac{\gamma^2}{(mc^2)^2} \left(\frac{d\mathbf{p}_{\perp}}{dt} \right)^2, \quad (1.13)$$

where $d_t \mathbf{p}_{\perp}$ is the change of the momentum in transverse direction. Another fact which is not directly obvious from (1.13) is its dependence on the rest mass. For a given total energy (1.5) the radiation of an electron under transverse acceleration is much stronger than for heavier charged particles.

The kinematic energy of a particle has to decrease by the same amount as it emits energy as electromagnetic waves due to energy conservation. For relativistic particles the Lorentz force (1.1) can be extended [7, 8],

$$m \frac{d\gamma \mathbf{v}}{dt} - \frac{2q^2 \gamma}{3c^3} \left(\frac{d^2 \gamma \mathbf{v}}{dt^2} + \frac{\gamma^3}{c^2} \left(\left(\mathbf{v} \cdot \frac{d\mathbf{v}}{dt} \right) \frac{d\mathbf{v}}{dt} - \left(\frac{d\mathbf{v}}{dt} \right)^2 \mathbf{v} \right) \right) = \mathbf{F}_{\text{ext}}(\mathbf{r}, \mathbf{v}, t), \quad (1.14)$$

where \mathbf{F}_{ext} is the Lorentz force (1.1) without corrections for the radiation. (1.14) is the Lorentz-Abraham-Dirac force which unfortunately has the fundamental problem of “run-away” solutions. There is a solution for \mathbf{v} different from zero even in the absence of any exterior force which contradicts causality.

If the energy of particles in a circular accelerator is to be kept constant or increasing then the losses due to radiation have to be compensated. This sets an economical limit on the kinematic energy one can achieve with a circular electron accelerator.

An accelerated charged particle does not emit its radiation uniformly into all directions. Instead the radiation is confined to a cone around the particles instantaneous tangent in forward direction with an opening angle proportional to $1/\gamma$, see Fig. 1.2 and Fig. 1.3. In an instantaneously co-moving frame the radiation pattern of the particle resembles a horn torus² with its axis in the direction of acceleration. By proper transformation to a system in which the particle is not at rest this pattern is transformed to a highly directed radiation pattern, for details see [3, 6].

The electromagnetic waves that are emitted by accelerated charged particles are partially polarized. About 90 % of the radiated power is polarized in the plane of propagation (σ polarization) while the rest is polarized in perpendicular direction (π polarization). The polarization depends both on the angle of observation and on the frequency [9, 10]. This is illustrated in Fig. 1.4. The spectrum of synchrotron radiation is very broad. Its fundamental frequency is given by $\omega_0 = |\beta| c / \varrho = |d_t \mathbf{p}_{\perp}| / |\mathbf{p}|$, where ϱ is the radius of the circular path, \mathbf{p}

²A torus is called a horn torus if the surface touches the axis of revolution.

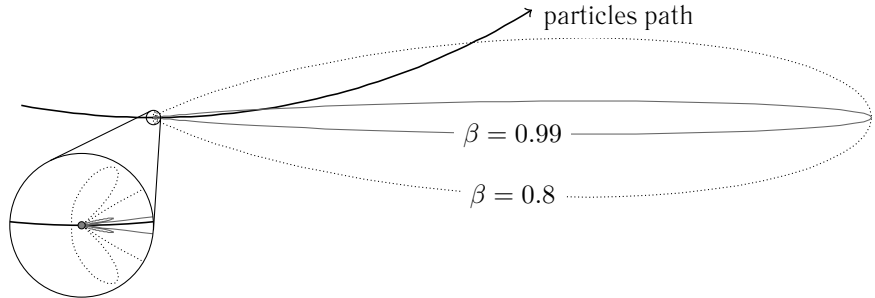


Figure 1.2: The pattern of total radiation power by a particle at $\beta = 0.8$ and $\beta = 0.99$ in the plane of motion. The particle that propagates on a circular path is visualized by the gray filled circle in the center of the zoomed part. The total radiation power for a given angle is proportional to the distance between the particle and the lobes under that angle.

is the momentum and β is the relative velocity of the particle. The spectrum consists of whole multiples of the fundamental frequency. The bandwidth of the spectrum is determined by the duration of the light pulse. Its temporal length is $T \simeq \frac{\varrho}{2\gamma^3 c}$. This corresponds to a spectral width of

$$\omega_c \sim \frac{1}{T} \sim \omega_0 \gamma^3, \quad (1.15)$$

where ω_c is called the critical frequency. Thus the spectrum for a circular accelerator with a total particle energy of 200 MeV ranges from ~ 300 MHz to $\sim 1.8 \cdot 10^{16}$ Hz or equivalently from wavelengths of ~ 1 m to ~ 500 Å. However the radiated power is not spread uniformly in this range. Instead it exhibits a complicated dependency on the frequency. For low frequencies it scales as

$$S \left(\frac{\omega}{\omega_c} \right) \propto 1.33 \left(\frac{\omega}{\omega_c} \right)^{1/3}, \quad (1.16)$$

whereas for high frequencies beyond the critical frequency it scales as

$$S \left(\frac{\omega}{\omega_c} \right) \propto 0.77 \left(\frac{\omega}{\omega_c} \right)^{1/2} e^{-\frac{\omega}{\omega_c}}. \quad (1.17)$$

The exact dependency of the radiated power on the frequency can be found in Fig. 1.5.

The results so far are only valid for charged particles in free space. However the particles in accelerators propagate inside metallic tubes which sustain a good vacuum inside. The electrons inside the metallic walls interact with the electromagnetic fields which are induced by the particles. The tangent fields on the surfaces have to vanish for a perfect conductor or have to be very small for real metals. The consequence is that not all frequencies emitted by accelerated charged particles fit into the pipes. Waves with wavelengths of the order of the transverse dimensions of the pipes and longer are therefore suppressed.

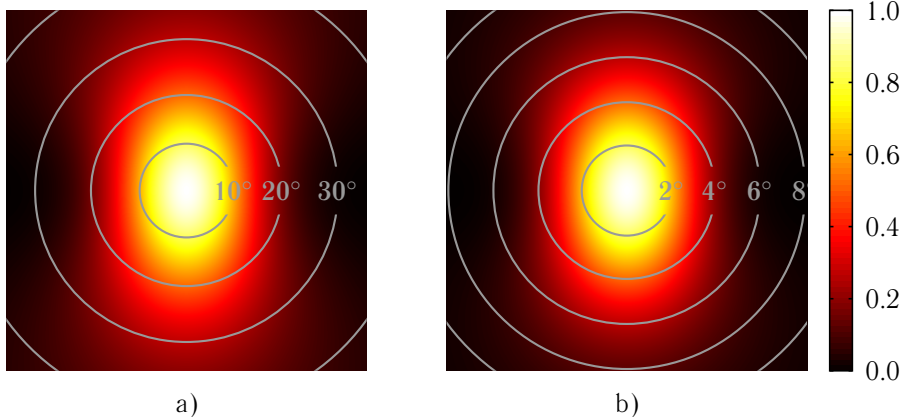


Figure 1.3: The radiation power in arbitrary units in a plane perpendicular to the tangent of the particle path for a) $\beta = 0.8$, $\gamma = 1.67$, $\theta \leq 40^\circ$ and b) $\beta = 0.99$, $\gamma = 7.09$, $\theta \leq 10^\circ$. θ is the angle between the tangent of the particle and the ray from the particle to the point in this plane of observation. The higher the speed of the particle the narrower is the cone to which the radiation is confined.

Incoherent Synchrotron Radiation

So far in this section only the radiation of a single charged particle was treated. The total power radiated by multiple particles scales only linearly with the number of particles [11]. From the definition of the energy flow (1.11) one could expect a quadratic dependence on the number of particles. This would indeed be the case if all emitted electromagnetic waves were in phase for all frequencies. The waves have to be in phase to interfere constructively. The radiation features a quadratic dependence on the number of particles only with constructive interfering waves. The constriction on the phase for all frequencies implies that the particles are concentrated within a volume with dimensions smaller than the shortest wavelength. We have seen that the critical frequency (1.15) scales as γ^3 thus the critical wavelength scales as $1/\gamma^3$. Even for moderately high speeds it is beyond limits to squeeze all the particles into such a small volume.

The electron bunches in particle accelerators are much larger than the shortest wavelength in the radiation they emit. Thus only radiation with wavelengths longer than the bunch can exhibit constructive interference. For most current machines the part of the frequency spectrum that could exhibit constructive interference has still longer wavelength than the dimensions of the vacuum pipe and is thus effectively suppressed.

Coherent Synchrotron Radiation

Some machines feature very short bunches that are shorter than the transverse dimensions of the vacuum pipes. A limited range of the spectrum emitted by accelerated particles in

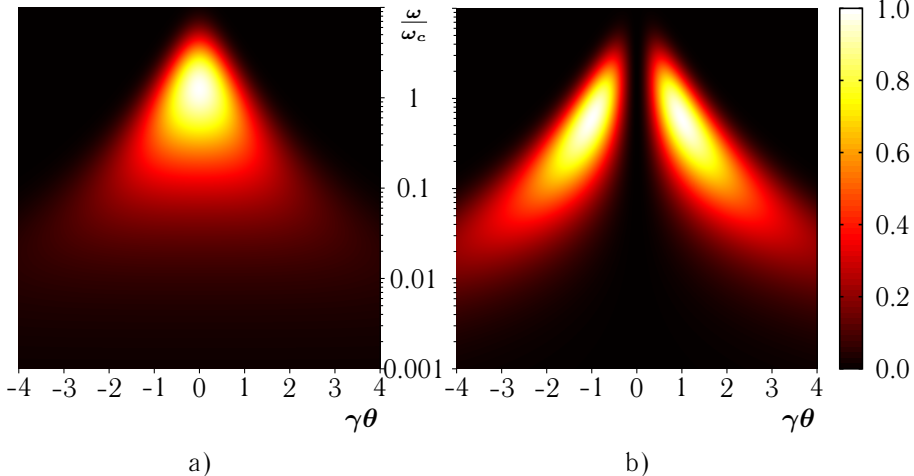


Figure 1.4: The energy radiated in dependence of the frequency and the angle of observation for a) σ polarization and b) π polarization.

these machines can interfere constructively. This part of the radiation is said to be temporally coherent. The coherence is not perfect due to the finite length of the bunch and the resulting phase shift. Thus the transition from incoherent to coherent radiation is not abrupt but smooth. The degree of coherence is not only determined by the length of the bunch but also by the charge distribution inside the bunch. For a bunch of length σ_z with Gaussian distribution the spectrum of the coherent part of radiation inside a bend is given by [6, 11]

$$S_{\text{coh.}}(\omega, N) = N^2 \exp\left(-\frac{\sigma_z^2 \omega^2}{2c^2}\right) S(\omega), \quad (1.18)$$

where N is the number of particles and $S(\omega)$ is the spectrum of a single particle, see Fig. 1.4. The incoherent part of the radiation is on the other hand given by

$$S_{\text{inc.}}(\omega, N) = N \left(1 - \exp\left(-\frac{\sigma_z^2 \omega^2}{2c^2}\right)\right) S(\omega). \quad (1.19)$$

The coherent radiation becomes very powerful for typical bunch population sizes in the range $10^8 - 10^{10}$ and for low frequencies. It thus outperforms strongly the incoherent radiation in the lower range of the spectrum.

Inside undulators particle bunches can also emit spatially coherent radiation. Spatial coherence characterizes the transverse size and divergence of the photon beam which is connected to the emittance of a particle beam. The upper limit of spatial coherence is determined by the diffraction of the photon beam. The transverse emittance (1.6) of a particle bunch has to satisfy the condition

$$\epsilon_{x,y} \leq \frac{\lambda}{4\pi} \quad (1.20)$$

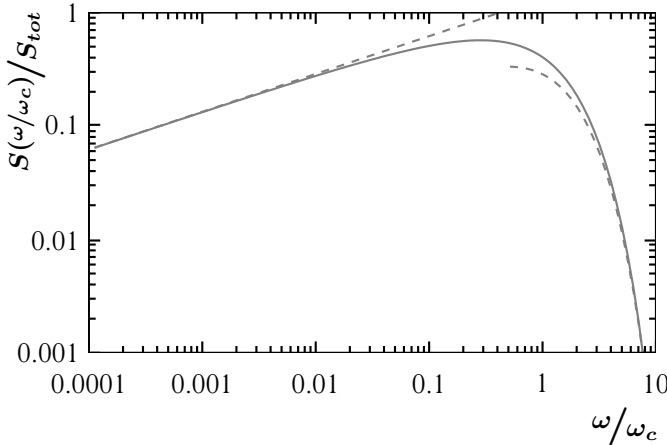


Figure 1.5: The dependency of the radiation power on the frequency of the emitted waves [9, 10]. The radiation power is normalized by the total radiation power. The approximations for the low frequency and high frequency ranges are indicated with dashed lines.

to produce a diffraction-limited photon beam at a given wavelength.

1.1.4 X-Ray Free Electron Lasers

The characteristics of relativistic particles as listed in Section 1.1.1 are necessary to understand the design of particle accelerators and of Free Electron Lasers [12] in particular. They aim for extremely bright, short and spatially coherent light pulses with a very narrow spectral bandwidth. Synchrotron radiation with these characteristics enables research of materials that so far were out of reach for the light produced at storage rings. Furthermore FELs will allow observations of dynamical probes owing to the short pulses.

The light pulses are generated by accelerating electron bunches to high energies and then sending them through undulators. Inside an undulator with period length $\lambda_u = 2\pi/k_u$ and amplitude B_u the velocity of the bunch can approximately be described by

$$\begin{pmatrix} \beta_x \\ \beta_z \end{pmatrix} = \begin{pmatrix} \frac{K}{\gamma} \cos(k_u ct) \\ \beta - \frac{K^2}{4\gamma^2} (1 - \cos(2k_u ct)) \end{pmatrix}, \quad (1.21)$$

where $K = eB_u\lambda_u/2\pi m c$. If there is a co-propagating linearly polarized electromagnetic plane wave with its electric field parallel to the x -axis then the bunch and the plane wave can interact. The electrons are accelerated or decelerated by the wave depending on the relative phase between wave and bunch. For most frequencies of the plane wave the total energy transferred from the bunch to the wave and vice versa vanishes. But if the wave

length of the plane wave is matched to the period length of the oscillation of the bunch then energy is transferred. This wave length is given by

$$\lambda_n = \frac{\lambda_u}{2n\gamma^2} (1 + K^2), \quad n = 1, 3, 5, \dots \quad (1.22)$$

Only the case for which the bunch loses energy to the field is interesting for synchrotron light sources.

FELs are separated into low-gain and high-gain machines depending on the amount of energy transferred to the field. Low-gain machines use mirrors at both ends of the undulator to accumulate field energy. Thus the electromagnetic wave passes the undulator several times. Every time the wave passes the undulator only a fraction of the energy is coupled out until an equilibrium is reached. For the vacuum ultraviolet and the X-ray regime no mirrors with sufficient reflectivity at normal incident exist. Therefore other means of amplification have to be used.

In high-gain machines the wave passes the undulator only once. In this class of machine the amplification is due to modulation of the charge density. Electrons gain or lose energy to the field depending on the position within the bunch. But the path length of a charged particle in an undulator depends on its energy. Faster particles have a shorter path, see also Fig. 1.6. Thus the electrons are concentrated into micro-bunches which are shorter than the wave length. Finally the temporal coherence of the emitted radiation increases and so does its power.

Micro-bunches can be induced with a conventional laser with appropriate wave length. Alternatively one can rely on self-amplification of the radiation [13]. The initial radiation has a broad spectrum. The process of concentration is initiated by the part of this radiation that happens to match (1.22). This mode of operation is called Self-Amplified Spontaneous Emission (SASE).

Linear accelerators are used for high-gain FELs in order to achieve the beam quality and the peak current that is needed for strong amplification. The spectral brightness [14] of the light pulse in a FEL is controlled by two factors: by the numbers of electrons in the bunch and by the coherence with which they emit the light. The spatial and temporal coherence determine not only the number of photons but also the divergence of the light beam. The necessary peak current on the other hand is achieved by compressing a large number of charged particles into a small volume. The charge density that is required for the operation of FELs is not feasible at low energies due to Coulomb repulsion of the particles. At higher speeds this repulsion is alleviated due to the length contraction. FELs therefore have relatively long bunches at low energies which are then compressed in one or more stages at higher energies.

Magnetic chicanes are inserted into the linear accelerators for the compression of a bunch, see Fig. 1.6. They consist of three or more magnets in plane with magnetic fields perpendicular to the direction of propagation of the bunch. The bunch is deflected in the magnetic field due to the Lorentz force (1.1). The angle of deflection in a magnet depends on the energy of the particle: the higher the energy the smaller is the angle. The magnets are in such a configuration that the path length of a particle depends on its energy. Slower electrons have to cover a longer distance in these configurations. The bunch has to feature an energy chirp before the chicane in order to achieve compression. Particles in the head of

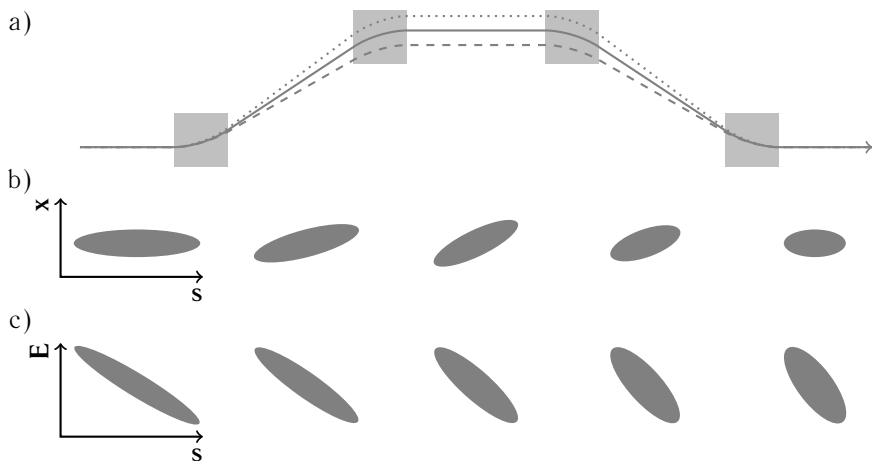


Figure 1.6: One example of a magnetic chicane used to compress particle bunches, other configurations of the magnets exist. a) shows the paths of a particle at the nominal energy (solid line), at lower energy (dotted line) and at higher energy (dashed line). b) shows the bunch in the plane of propagation while c) shows the energy distribution along the bunch.

the bunch have to have a lower energy than those in the tail with an approximately linear increase in-between. In this way particles at the head need longer to pass the chicane which results in a compression of the bunch.

The main technical challenge of magnetic chicanes is the emission of coherent synchrotron radiation (CSR). It occurs in the last magnet where the bunch is shorter than the surrounding vacuum tubes. CSR in this part of a machine has a negative effect on beam quality. It increases the emittance of the bunch [15] on one hand and it enhances charge density modulations [16] that may be present in particle bunches. The increase of emittance can be alleviated by the layout of a machine [17–19]. However the amplification of density modulations can not so easily be suppressed.

Amplitude modulations of lasers in photocathodes and shot noise cause density modulations in particle bunches. These initial density modulations are then transformed into energy modulations through longitudinal space charge forces [20]. The longitudinal space charges act mainly at low energies since at higher energies the longitudinal motions get frozen due to the length contraction. Dispersive sections of particle accelerators can then transform the energy modulation back into a density modulation.³ Coherent synchrotron radiation can then not only occur at wavelengths longer than the bunch but also at wavelengths comparable to the length of the period of modulation. The radiation then enhances the amplitude of the modulation. This process of amplification of an initial density modulation is called microbunching instability. It has negative effects on the performance of FELs.

Microbunching can be eliminated or reduced by the use of smoother laser pulses [21] or

³The path length of a particle in dispersive sections depends on the particles energy.

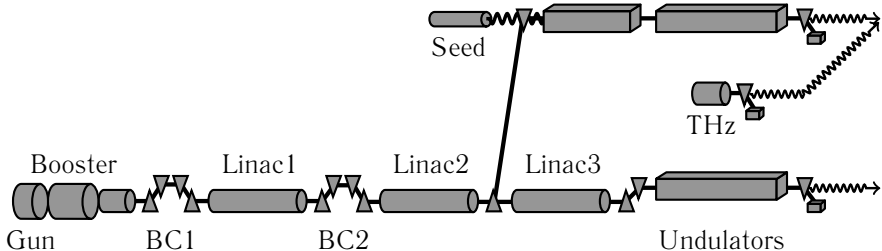


Figure 1.7: The layout of SwissFEL featuring two beamlines providing synchrotron radiation of different ranges of wave length [25].

by elimination of the laser through the use of thermionic cathodes instead of photocathodes [22]. If the remaining laser modulations are still too large then devices, so-called heaters, that introduce an uncorrelated energy spread to the bunch can be added to the machine [20, 23, 24]. The amplification of density modulations is strongly suppressed by the presence of uncorrelated energy spread.

SwissFEL

The Paul Scherrer Institute in Villigen, Switzerland, plans to build its own FEL in the X-ray regime [25]. It will provide coherent synchrotron radiation with wave lengths in the range 0.1 nm–7 nm. Two beamlines operating at different energies are used to cover this broad range, see Fig. 1.7. The range 0.1 nm–0.7 nm is covered by a linear undulator, called Aramis, whereas the upper range is covered by a helical undulator with adjustable geometric magnet configuration, called Athos. SASE is used in both beamlines though for Athos a seed laser and an additional undulator, d'Artagnan, is foreseen at a later stage. This upgrade will increase the temporal coherence of the light. Furthermore a THz pump source is foreseen for Athos. With the pump source chemical processes can be initiated.

The photocathode gun provides electron bunches with a charge of 200 pC and a current of 22 A at a repetition rate of 100 Hz. The beam is accelerated using normal conducting cavities to 3.4 GeV. The beam is then switched to Athos or to Aramis. In the latter case the beam is further accelerated to 5.8 GeV. The bunches are compressed when they have an energy of 410 MeV by a factor of ~ 12 in BC1 and when they have an energy of 2.1 GeV by another factor of ~ 8 in BC2. The magnetic chicanes are D-shaped as in Fig. 1.6. A beam heater will be installed at an energy of 170 MeV to reduce microbunching.

1.2 Computational Particle Dynamics

Particle accelerators are complex systems for simulations due to the large number of particles and their interaction with each other, electromagnetic fields and the surrounding vacuum tubes. The dynamics of the particles is described by the collision-less relativistic Vlasov equation,

$$\frac{\partial f}{\partial t} + \mathbf{v} \cdot \nabla_{\mathbf{x}} f + q (\tilde{\mathbf{E}}_{\text{tot}} + \mathbf{v} \times \tilde{\mathbf{B}}_{\text{tot}}) \cdot \nabla_{\mathbf{p}} f = 0, \quad (1.23)$$

where $f(t, \mathbf{x}, \mathbf{p})$ describes at time t the distribution of particles in the 6-dimensional space (\mathbf{x}, \mathbf{p}) of position \mathbf{x} and momentum \mathbf{p} . The velocity and relativistic momentum are connected through

$$\mathbf{v} = \frac{c \mathbf{p}}{\sqrt{(mc)^2 + |\mathbf{p}|^2}}, \quad (1.24)$$

where m is the rest mass of the particle. $\tilde{\mathbf{E}}_{\text{tot}}$ and $\tilde{\mathbf{B}}_{\text{tot}}$ combine external fields which originate from accelerator devices and internal fields due to space charge and wake fields. The internal fields are described by Maxwell's equations (1.4). The source for Maxwell's equations, the charge and current distribution, is given by

$$\tilde{\rho} = q \int_{\mathbb{R}^3} f \, d^3 p, \quad \tilde{\mathbf{J}} = q \int_{\mathbb{R}^3} \mathbf{v} f \, d^3 p. \quad (1.25)$$

The combination of relativistic Vlasov and Maxwell's (RVM) equations including appropriate boundary conditions describe the system self-consistently.

For large systems such as particle accelerators the full description of the system of Vlasov-Maxwell's equations at sufficient resolution is beyond the capabilities of current computer clusters. The main difficulties stem from the nonlinear interaction of the particles and the scaling behavior of a 6-dimensional space. Hence, different strategies to simplify the full RVM system have been investigated. The strategies can consist of a reduction of dimensions, sampling of the 6-dimensional space by a discrete number of particles, linearizing Maxwell's equations and combinations thereof.

The external fields can also be approximated in different ways, e.g. they can be described by a sampling or by their action on particles. For a particle in 6-dimensional phase space the action of external fields can be approximated by a multiplication of a 6×6 matrix with the 6-dimensional vector [26].

Self-consistency is often neglected when dealing with discrete particles. Instead of solving Maxwell's equations a Poisson problem is solved. The problem can be transformed to a system for which the average speed of the particles of one bunch vanishes. The relative speeds of the individual particles are assumed to be very small such that they can be neglected. Finally Poisson's equation for electrostatics,

$$-\Delta \tilde{\phi} = \nabla \cdot \tilde{\mathbf{E}}_{\text{tot}} = \frac{\tilde{\rho}}{\epsilon_0}, \quad (1.26)$$

is solved for the electrostatic potential $\tilde{\phi}$ with open or periodic boundary conditions. For discrete particles and open boundaries this yields

$$\tilde{\phi}(\mathbf{r}) = \sum_{i=1}^{N_p} \frac{1}{4\pi\epsilon_0} \frac{q_i}{|\mathbf{r} - \mathbf{r}_i|}. \quad (1.27)$$

This approach of transforming to a co-moving system and solving Poisson's equation neglects any effect due to the finite speed of light. The speed of light in this system is, as we know from Section 1.1.1, also c but the transformation includes a scaling in longitudinal direction by a factor γ due to length contraction. Thus propagating information about changes in charge density is slower in longitudinal direction. If charge densities change slowly then this effect can be neglected.

If (1.27) is solved directly then the cost scales as N_p^2 with the number of particles N_p . Usually, to overcome this strong scaling a fast Fourier method (FFT) is applied [27]. The charge distribution is scattered onto a mesh, then this charge distribution is convoluted with the appropriate Green's function depending on the chosen boundary condition. The cost of this particle-mesh scheme scales as $N_p + N_g \log N_g$ where N_g is the number of grid points.

Instead of a fast Fourier transform an implicit finite-difference method can be applied. This allows simulations including perfect electric conducting boundaries on rectangular and cylindrical domains [28] and also irregular domains [29, 30].

Wake fields due to the vacuum pipes can be described by a frequency dependent impedance. The exact impedance depends on the material and the geometry of the pipe. The voltage that a source particle exerts on a particle behind it is then

$$V(\omega) = -Z(\omega)I(\omega), \quad (1.28)$$

where Z is the impedance and I is the current of the source. Thus in time domain (1.28) is a convolution of the impedance and the current of the bunch. For simulations the 3-dimensional charge distribution is reduced to a line density, then binned and smoothed with filters before the FFT is applied. The transformed current density is then multiplied with the impedance and the result is transformed back to the time domain. The resulting electric field is a function of the longitudinal position within the bunch. It is then calculated for every particle in the bunch according to its position.

For CSR one often relies on a similar approach. The electromagnetic field due to a particle moving on a circle in free space can be calculated exactly with (1.10). The field has been calculated for all points on the same circle [10, 31]. For high particle energies the radiated power is almost exclusively emitted in forward direction, whereas for low energies a fraction is also emitted in transverse and backward direction, see Fig. 1.3. For the case of high-energetic particles an impedance in forward direction can be calculated [32]. The procedure is then the same as for a regular wake with the important difference that wakes exert forces on trailing particles only. The electromagnetic fields of a particle propagating on the mid-plane between two parallel metallic plates that stretch to infinity [10] and for finite plates [33] can also be calculated. For the infinite plates an impedance can be calculated [32].

All of these approaches for CSR neglect any transient effects due to the finite length of the bend. Instead they describe the steady state case of a bunch circling infinitely long in the field of a dipole magnet. In [34] the four different stages of a bunch passing a bending magnet are treated separately and for each a corresponding wake function is derived. This model for CSR is still actively developed [35–37].

The 1-dimensional approach also neglects any influence of the transverse dimensions and of changes in current density between retarded and current time. On the other hand it

gives a good approximation of effects due to CSR in short time.

In the following a short list given of simulation codes for particle accelerators that include routines to model coherent synchrotron radiation, see also [38]:

elegant [39] uses the matrix formulation to describe the action of accelerator devices. Space charge forces are calculated using the same approach as for wake fields but with the impedance for a round beam with uniform transverse distribution [23]. The positions at which space charge is calculated is given by the user. It uses the 1-dimensional algorithm for CSR including also the drifts following a bend [40].

Parmela_B [41], *Astra* [42], *Impact-T* [43] and *OPAL* [44] integrate the equation of motion (1.1) of particles. For this, different algorithms are used, among others Runge-Kutta and the Boris pusher [45]. The field induced by the particles are evaluated in the coordinate system that is co-moving with the center of mass of the bunch. The intervals between two solutions of the Poisson problem are determined by the codes. Some of the codes listed have adaptive time steps or space charge intervals implemented. For CSR the 1-dimensional algorithm is used with different levels of accuracy such as transient effects or inclusions of drifts following the bend.

The accelerator devices are represented by field maps containing a (uniform) sampling of their fields. The samplings are imported from other codes.

Bmad [46] provides both methods for the matrix formalism and for tracking. An improved algorithm for CSR calculations is implemented [35, 36] including image charges on parallel plates above and below the plane of propagation.

CSRtrack, *TraFiC⁴* [47] CSRtrack is based on TraFiC⁴ with some improvements and additions. They too integrate the paths of the particles but use a different approach for CSR. The basic idea of both is to store the history of the positions of the particles and to calculate the retarded fields (1.10) directly. This has two main difficulties: storing the history requires a lot of memory and, as noted before, this algorithm scales as N_p^2 with the number of particles N_p . The difficulty of storing much data is alleviated in CSRtrack by not storing every time step but at larger intervals and interpolating in-between. The conducting walls are simulated by images charges too.

A code by *Li* [48, 49] uses the same basic idea as CSRtrack and TraFiC⁴ but the particles propagate in a plane only, thus reducing the algorithm to two dimensions.

A code by *Agoh* [50] makes the assumptions that the transverse dimension of the beam pipe is much smaller than the radius of the bend and that the CSR acts in forward direction only. With these assumptions Maxwell's equations are transformed to the frequency domain and then integrated on a mesh for

And finally a code by *Warnock et al.* [51] couples Maxwell's equations with Vlasov's equations in two dimensions. They model CSR by its impedance.

The difficulty for all algorithms for CSR simulations is the finiteness of the speed of light. This finiteness results in electromagnetic fields emitted in the past being propagated to the present. Thus information in the form of electromagnetic waves is being transported

and arrives with a delay which depends on the distance between location of emission and detection. The easiest and fastest solution is to reduce the dimensions of the problem. The 1-dimensional algorithm is widely used and gives reasonable results. The algorithm is based on an analytic solution with some simplifications. Its core consists of a non-trivial convolution of the charge density with a wake function.

The second solution that is implemented in some codes is the storage of the history of the particles. Then for every time step and for every particle i any charge j at time t' in the past for which $c(t - t') = |\mathbf{r}_i - \mathbf{r}_j|$ is searched. The electromagnetic field at the position of particle i is then calculated from the positions, speeds and accelerations of all particles fulfilling this condition. This yields very accurate results for the electromagnetic field. But it limits the number of particles that can be tracked due to limitations of memory and compute time. Conducting walls are modeled by several layers of image charges. For every particle inside the vacuum pipe one particle is added in every layer, thus multiplying the number of particles.

The particles are a representation of the 6-dimensional phase space of Vlasov–Maxwell's equations. The accuracy of this representation is reduced when reducing the number of particles. Furthermore the particle method introduces noise which possibly is not present in the phase space. This artificial noise can be lowered by an increasing number of particles.

The third approach is a clever transformation of Maxwell's equations into the frequency domain and integrating them on a grid. The size of the mesh can be drastically reduced in forward direction compared to a grid in the time domain. The assumptions and simplifications that are made may reduce the applicability of this method.

The last approach is to integrate Vlasov's equation (1.23) coupled with Maxwell's equations in two dimensions. For a full 6-dimensional phase space the computational requirements are big. Therefore only a 4-dimensional phase space is simulated.

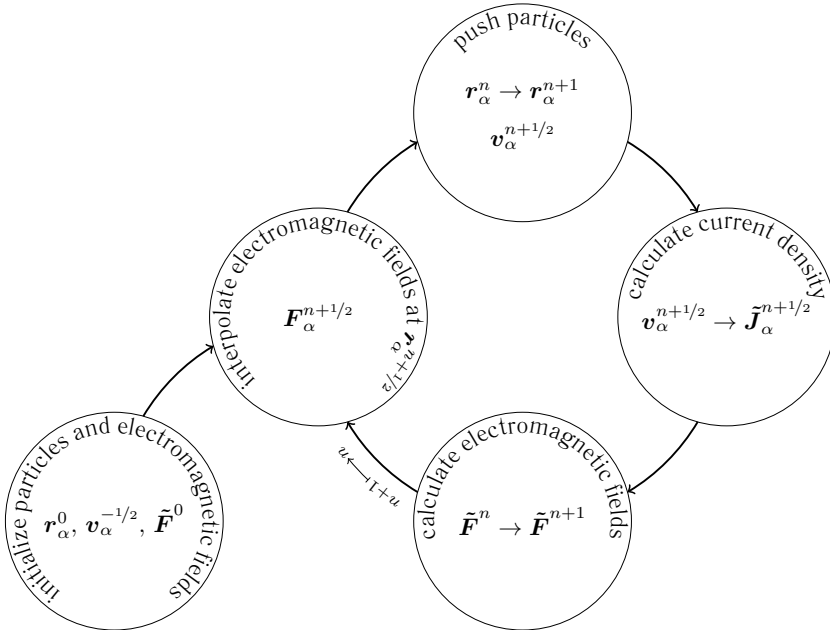


Figure 1.8: Diagram of Particle-in-Cell codes that integrate the electromagnetic fields.

1.3 Goal of Thesis

Many approaches have been implemented and shown their advantages as well as disadvantages. The goal of this thesis was to write an application with which one can simulate self-consistently a single bend of a magnetic chicane in two dimensions. First, the electromagnetic fields should be updated using a finite-difference method. Second, the validity of the produced results should be shown and, third, a simple example should be simulated and compared to results produced with the 1-dimensional model of *OPAL* [44].

The steps in a code such as envisioned are depicted in Fig. 1.8. Every simulation starts with the determination of positions and momenta of the particles. From these the initial electromagnetic field can be calculated. Then the temporal integration of the field and the paths of the particles can start. For the latter the field has to be interpolated at the positions of the particles. Then the force on the particles can be determined and their positions and momenta can be updated. The propagation of the particles causes an electric current which is the source term for the integration of the electromagnetic field. The loop is then closed and is repeated for a specified number of times or until the particles have traversed the domain.

The computational requirements for a 3-dimensional implementation of such a code are big considering that for one wave length approximately 20 mesh cells are needed. For the full magnetic chicane BC1 of SwissFEL a mesh with approximately $320 \cdot 10^{12}$ mesh cells with equal side lengths are needed. This number is estimated from the values in Table 1.1.

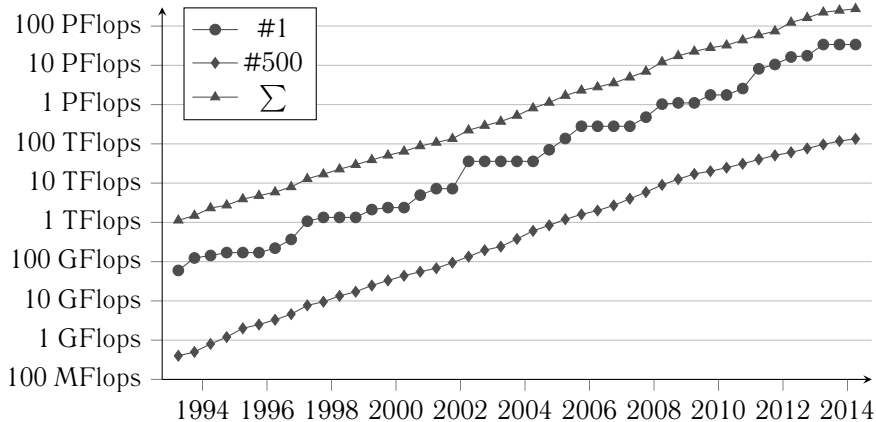


Figure 1.9: The maximum LINPACK [52] performance in the course of the last 20 years of the fastest computer system on the Top500 list [53], number 500 and the sum of all systems on that list.

Table 1.1: Parameters of the magnetic chicane BC1 of SwissFEL [25]

bunch length after last bend	70 µm
particle energy	400 MeV
length bends	0.25 m
bending angle	3.82°
total length chicane	14 m
vacuum pipe width in the order of	0.07 m
vacuum pipe height in the order of	14 mm

The initial goal of this thesis was to solve the 3-dimensional problem by using several layers of finer grids in the vicinity of the particle bunch. We came soon to the understanding that the complexity of this approach was beyond the feasibility of this thesis. Thus it was decided to reduce the dimension of the problem. A reduction to two dimensions reduces the problem size by several orders of magnitude to approximately $80 \cdot 10^9$ mesh cells. Thus a time domain simulation of the full chicane in two dimensions is still very challenging. Instead of the full chicane only parts of it could be simulated.

For a simulation of the full chicane in two dimensions one would have to implement non-uniform meshes or sub-gridding schemes could be used to further reduce the problem size. However non-uniform meshes and sub-gridding introduce new complexities and problems such as reflections at boundaries between mesh cells of different size.

A 3-dimensional simulation or a 2-dimensional of the whole chicane in time domain may not be feasible today but as the number of transistors on a computer chip doubles approximately every two years and the performance of High Performance Computer (HPC) systems scales even faster, see Fig. 1.9, it may become feasible in the future. Due to the

large meshes involved an efficient and not overly complex method is needed to integrate Maxwell's equations. Thus a method based on the Finite-Difference Time-Domain (FDTD) is preferred to one based on finite-elements or unstructured grids.

When a regular grid is used to simulate a bend then many cells are outside the domain. To reduce the size of the mesh one could instead use body fitted grids. The two advantages that such grids provide are first that field samplings only occur where they are needed and, second, to model the boundaries that are imposed by the metallic vacuum pipe is trivial. However the use of body fitted grids also has disadvantages. First, to determine the cell in which a particle is located is trivial when a regular grid is used whereas it is slightly more complicated with body fitted meshes. Furthermore to interpolate the electromagnetic field at the position of a particle and to calculate a charge preserving current through the faces of a cell is less complex in a regular grid. These three operations are performed several times for every particle and every time step. Second, it is not *a priori* clear how numerical dispersion behaves in body fitted grids. As we will see a low numerical dispersion is crucial for the simulation of relativistic charged particles. Third, the library *Independent Parallel Particle Layer* (IPPL) [54], which we intend to use for both electromagnetic fields and particles, does not provide any methods for body fitted grids. The utilization of body fitted grids for the simulation of magnetic bunch chicanes seems promising for a future thesis.

The advantage of simulating a bunch compressor using a self-consistent Maxwell solver coupled with a Particle-in-Cell (PIC) method is, that the history of the 6-dimensional phase space is stored in the electromagnetic fields. The positions, velocities and accelerations of the particles do not have to be stored and the algorithm does not scale as N_p^2 with the number of particles but only linearly.

In this thesis we used a Transverse Electric / Transverse Magnetic (TE/TM) method [55] that is based on finite-differences. This method does not exhibit dispersion in one space dimension contrary to the standard Yee method [56] that suffers from dispersion in all directions. For the calculation of the currents we used higher order shape functions that preserve the charge [57]. To compute the initial electromagnetic field we applied a Poisson solver based on the conjugate gradient method that is preconditioned by a smoothed aggregation based algebraic multigrid method [30].

New is the adaption of the TE/TM method to a self-consistent PIC method using a moving mesh that is embedded in a larger mesh. The mesh moves synchronously with the particle bunch and updates the current density that is induced by the particles. A master-slave scheme was applied to balance the computational load among the compute cores. Finally for the validation a code that is based on Liénard-Wiechert potentials on a mesh was developed.

Chapter Two

Initial Conditions

In general at the start of a simulation only some parameters describing the initial positions and momenta of a bunch as well as the computational domain are known. However to simulate the electromagnetic field one also has to have an initial solution for it. Thus the initial solution for the electric and magnetic field has to be calculated from the positions and momenta of the particles. For this one transforms to a system in which the average of the particles are at rest. The relative speeds of the individual particles are then so small that they can be neglected. It remains to solve an electrostatic problem. This problem can be solved in two steps. Instead of the electric field one computes the electric potential first,

$$\nabla \cdot \tilde{\mathbf{E}} = \nabla \cdot (-\nabla \tilde{\phi}) = -\Delta \tilde{\phi} = \frac{\tilde{\rho}}{\epsilon_0},$$

where the Coulomb gauge, $\nabla \cdot \tilde{\mathbf{A}} = 0$, is assumed, where $\tilde{\mathbf{A}}$ is the vector potential, see (1.8).

The electric field in the co-moving system is then obtained by calculating the gradient of the potential. The initial electromagnetic field in the coordinate system in which the computational domain is at rest can be calculated from the solution in the co-moving system. The transformation of the electromagnetic fields between two systems which are in

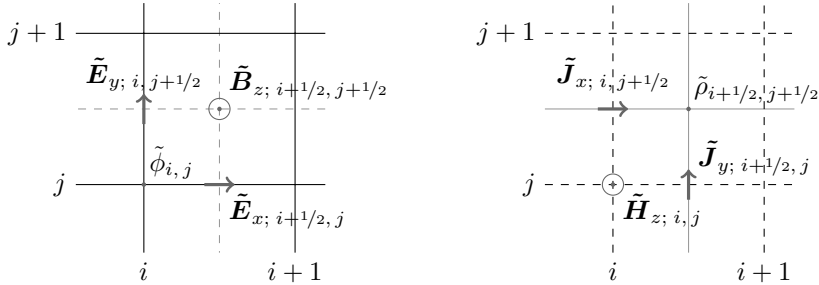


Figure 2.1: The sampling points of all scalar and vector fields in 2-dimensional finite-difference simulations of Maxwell's equations. The primal grid is drawn with a solid line while a dashed line is used for the dual grid. All entities residing on the primal mesh are drawn in the left part while the ones residing on the dual mesh are drawn on the right.

constant motion relative to each other is given by

$$\begin{aligned}\tilde{\mathbf{E}}' &= \gamma (\tilde{\mathbf{E}} + \boldsymbol{\beta} \times \tilde{\mathbf{B}}) - \frac{\gamma^2}{\gamma + 1} \boldsymbol{\beta} (\boldsymbol{\beta} \cdot \tilde{\mathbf{E}}) = \gamma \tilde{\mathbf{E}} - \frac{\gamma^2}{\gamma + 1} \boldsymbol{\beta} (\boldsymbol{\beta} \cdot \tilde{\mathbf{E}}), \\ \tilde{\mathbf{B}}' &= \gamma (\tilde{\mathbf{B}} - \boldsymbol{\beta} \times \tilde{\mathbf{E}}) - \frac{\gamma^2}{\gamma + 1} \boldsymbol{\beta} (\boldsymbol{\beta} \cdot \tilde{\mathbf{B}}) = -\gamma \boldsymbol{\beta} \times \tilde{\mathbf{E}},\end{aligned}$$

where $\boldsymbol{\beta}$ is the normalized relative velocity between the two systems and $\tilde{\mathbf{B}} = 0$ in the co-moving system.

The finite-difference method does not work directly with smooth continuous fields. Instead it discretizes the fields at sampling points. For the simulation of Maxwell's equations in time domain two meshes are used: the primal mesh and the dual mesh that is shifted by half a cell size in each dimension, see Fig. 2.1. For the various fields different sampling points are used on the mesh: $\tilde{\mathbf{E}}$ and $\tilde{\mathbf{H}}$ are edge based, $\tilde{\phi}$ is node based, $\tilde{\mathbf{J}}$ and $\tilde{\mathbf{B}}$ are face centered and $\tilde{\rho}$ is cell centered. For rectilinear grid as used in FDTD the separation into fields residing on primal or dual grid is not important since the factors, that are needed to relate the fields, often reduce to unity or are easy to calculate. The separation is more important for other discretization methods [58, 59].

To be able to determine the charge density on the mesh one has to define the shape of the charged particles. The shape $S(\mathbf{r})$ can be chosen freely with the only restriction that $\int_{\mathbb{R}^d} S(\mathbf{r}) d\mathbf{r} = 1$. A very simple choice is to describe the particles as point sources. By far the most common choice though is to describe them by a charge cloud with constant density over the area or volume of a cell depending on the dimensionality of the problem. Beyond this area or volume, respectively, the density vanishes abruptly. In one dimension and for a mesh with cell size $\Delta x = 1$ this shape function is

$$S(x) = \begin{cases} 1 & \text{for } -1/2 \leq x < 1/2, \\ 0 & \text{otherwise.} \end{cases}$$

In the following this shape function will be denoted by S^0 .

Higher-dimensional shape functions can be constructed by a tensor product from any 1-dimensional shape function. A 3-dimensional shape function could be given e.g. by $S^{3D}(x, y, z) = S(x)S(y)S(z)$. The 1-dimensional shape functions that are used for the tensor product do not even have to be identical.

Higher order shape functions can be gained by repeated convolutions of S^0 with itself, each time increasing the order by one. If one denotes these shape functions by S^m , where m is the order of the function, then this procedure is described by

$$S^m(x) = \int_{-\infty}^{\infty} S^{m-1}(x - x') S^0(x') dx' \quad \text{for } m \geq 1.$$

The support of these shape functions is enlarged with every repetition. The benefit of higher order shape functions is a reduction in noise since changes in the charge density are smoother. On the other hand they increase the computational costs since more mesh nodes are touched by a particle and the functions are more complex to calculate. This is of no serious consequence for the initialization of the fields since the initialization is carried out once at the beginning of the simulation. Though the same shape function will be used throughout the simulation for the calculation of the current. Thus the function evaluation is carried out many times and increased computational costs does influence the time to solution considerably.

Finally the shape functions can be adapted to the actual mesh size by

$$S_{\Delta x}^m = \frac{1}{\Delta x} S^m \left(\frac{x}{\Delta x} \right).$$

The global charge density is then $\tilde{\rho}(\mathbf{r}) = q \sum_{\alpha=0}^{N_p-1} S_{\alpha}(\mathbf{r}) = q \sum_{\alpha=0}^{N_p-1} S(\mathbf{r}_{\alpha} - \mathbf{r})$.

The charge density is integrated over a cell of the dual grid and averaged by the cell area or volume, respectively, to calculate the charge density on the node at the center of the cell. This is repeated for every cell of the dual mesh. The integration and averaging can be done for every particle individually, the results are then accumulated:

$$\begin{aligned} \tilde{\rho}_{i,j} &= q \sum_{\alpha=0}^{N_p-1} \int_{x_{i-1/2}}^{x_{i+1/2}} \int_{y_{j-1/2}}^{y_{j+1/2}} S_{\Delta x}^m(x_{\alpha} - x) S_{\Delta y}^m(y_{\alpha} - y) dx dy \\ &= q \sum_{\alpha=0}^{N_p-1} \int_{\mathbb{R}} S^0(x_i - x) S_{\Delta x}^m(x_{\alpha} - x) dx \int_{\mathbb{R}} S^0(y_j - y) S_{\Delta y}^m(y_{\alpha} - y) dy. \end{aligned}$$

Thus the charge density on the mesh node due to a single particle of shape $S(x, y) = S_{\Delta x}^m(x_{\alpha} - x) S_{\Delta y}^m(y_{\alpha} - y)$ is given by

$$\tilde{\rho}_{i,j} = q S_{\Delta x}^{m+1}(x_{\alpha} - x_i) S_{\Delta y}^{m+1}(y_{\alpha} - y_j).$$

The charge of a particle is assigned to the mesh nodes by interpolation using the functions S^m . Nearest grid point (NGP) interpolation, where the charge is assigned to the nearest node, is achieved with $m = 0$. A bilinear or trilinear interpolation respectively is achieved with $m = 1$. In general m is equivalent to the order of the interpolation.

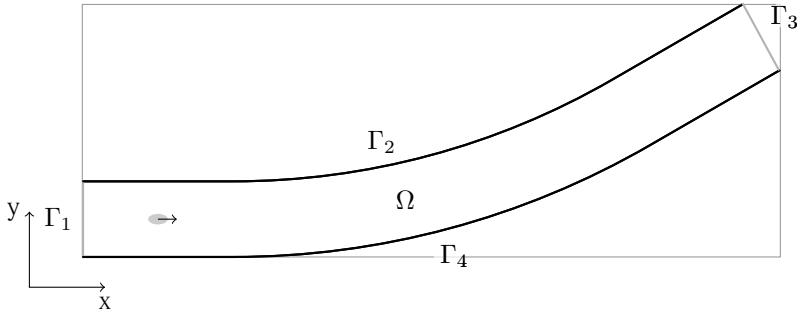


Figure 2.2: Example of a 2-dimensional domain for a bend. The initial position of the particle bunch is indicated by the gray ellipse and its velocity by the vector.

For the assignment of the charge density to the mesh nodes this perspective is more useful. On the other hand when the current density or the electromagnetic field at the position of the particles has to be calculated it is favorable to envision the particles having a shape of finite size.

Now that it is settled how to calculate the charge density on the mesh nodes one can start to tackle the initialization of the electromagnetic field. This starts by choosing an appropriate domain. The first step towards a simulation of a relativistic bunch that passes through a magnetic chicane could be to replace the 3-dimensional chicane by a single 2-dimensional bend. A possible domain for this is depicted in Fig. 2.2. The domain Ω is bounded on two sides by perfect electric conducting (PEC) walls, Γ_2 and Γ_4 . The other two boundaries, Γ_1 and Γ_3 , are open in the sense that the electric potential should continue as if Γ_2 and Γ_4 would stretch in straight lines to infinity on both ends. The initial position of the particle bunch is close to the boundary Γ_1 . The velocities of the particles are such that the distance to boundary Γ_1 increases as time passes by.

The further away an open boundary is from the source the more does the solution approach the solution one would get by replacing the open boundary by PEC. Thus the error is small if the open boundary on Γ_3 is replaced by PEC for the calculation of the initial electromagnetic field. Possibly also the open boundary condition on Γ_1 can be replaced by PEC. Though this depends on the distance, D , of the boundary to the bunch and on the speed of the bunch in normal direction. A large relativistic factor of the bunch, γ , implies a large length contraction. Thus the distance between boundary and bunch increases to γD by transforming to the moving frame.

Formally the following system has to be solved:

$$\begin{aligned} \Delta \tilde{\phi} &= -\frac{\tilde{\rho}}{\varepsilon_0} && \text{in } \Omega, \\ \tilde{\phi} &= 0 && \text{on } \Gamma_2 \text{ and } \Gamma_4, \\ \frac{\partial \tilde{\phi}}{\partial \mathbf{n}} + f \tilde{\phi} &= 0 && \text{on } \Gamma_1 \text{ and } \Gamma_3, \end{aligned} \quad (2.1)$$

where \mathbf{n} is the outer normal of the two boundaries. If one assumes that the average velocity is parallel to the x -axis then the (only) effect of transformation to the moving system is that the distances in the x -direction are stretched by the factor γ . This influences both the Laplace operator and the charge density. The charge density in the transformed system is $\tilde{\rho} = \gamma^{-1} \tilde{\rho}_r$ where $\tilde{\rho}_r$ is the charge density in the system at rest. The influence on the Laplace operator is a bit more complicated and depends on the method that is used to calculate the potential.

While the PEC boundary condition is the same in both 2D and 3D this is not true for the open boundary. In 3D the electric potential in free space of a point source located at the origin is given by

$$\tilde{\phi}(\mathbf{r}) = \frac{Q}{4\pi\epsilon_0 |\mathbf{r}|}. \quad (2.2)$$

The derivative along the x -direction is then

$$\frac{\partial \tilde{\phi}}{\partial x} = \frac{x}{\mathbf{r}^2} \tilde{\phi} \approx \frac{1}{|\mathbf{r}|} \tilde{\phi}.$$

Here the approximation is only valid for $|y|, |z| \ll |x|$. This result is valid for any direction since the potential (2.2) is rotational symmetric. In [29] and [30] $f = |\mathbf{r}|^{-1}$ is used in (2.1).

On the other hand the potential for a point source inside an infinitely long cylinder can be described in the form

$$\tilde{\phi}(\varrho, \varphi, x) = \sum_{m=0}^{\infty} \sum_{n=1}^{\infty} A_{mn} \exp(-k_{mn}|x|) J_m(k_{mn}\varrho) \cos(m\varphi),$$

where J_m are the Bessel functions, $k_{mn} = \lambda_{mn}/R$, λ_{mn} is the n th zero of J_m and R is the radius of the cylinder. Thus, the mode with the smallest k_{mn} , that is $k_{01} = 2.4048\cdots/R$, becomes dominant as the distance to the source increases. The derivative of the potential in x -direction is then

$$\frac{\partial \tilde{\phi}}{\partial x} = \sum_{m=0}^{\infty} \sum_{n=1}^{\infty} -k_{mn} A_{mn} \exp(-k_{mn}|x|) J_m(k_{mn}\varrho) \cos(m\varphi) \approx -k_{01} \tilde{\phi}.$$

This approximation is valid for large distances only.

Likewise the potential and its derivative in x -direction for a point source inside an infinitely long rectangular tube with transverse lengths $L_y = 2a$ and $L_z = 2b$ can be described in the form

$$\begin{aligned} \tilde{\phi}(x, y, z) &= \sum_{m=1}^{\infty} \sum_{n=1}^{\infty} A_{mn} \cos(k_m y) \cos(l_n z) \exp(-\kappa_{mn}|x|) \\ \frac{\partial \tilde{\phi}}{\partial x} &= \sum_{m=1}^{\infty} \sum_{n=1}^{\infty} -\kappa_{mn} A_{mn} \cos(k_m y) \cos(l_n z) \exp(-\kappa_{mn}|x|) \\ &\approx -\kappa_{11} \tilde{\phi}, \end{aligned} \quad (2.3)$$

where $k_m = m\pi/2a$, $l_n = n\pi/2b$ and $\kappa_{mn} = \sqrt{k_m^2 + l_n^2}$. Again the approximation for the derivative is only valid for large distances.

In 2D (not $2!/2$ D, the rotational symmetric case) the situation is more complicated. A point charge in 2D in the xy-plane corresponds to a charge line extending to $z \rightarrow \pm\infty$ in 3D. The electric potential in free space diverges:

$$\frac{4\pi\epsilon_0}{Q} \tilde{\phi}(x, y, 0) = \lim_{z' \rightarrow \infty} 2 \int_0^{z'} \frac{dz}{\sqrt{r^2 + z'^2}} = \lim_{z' \rightarrow \infty} 2 \cdot \ln \left(\frac{z' + \sqrt{r^2 + z'^2}}{r} \right),$$

where $r^2 = x^2 + y^2$. Nonetheless its derivative in any direction in the plane does converge:

$$-\frac{\partial \tilde{\phi}}{\partial x} = \lim_{z' \rightarrow \infty} \frac{z'}{r\sqrt{r^2 + z'^2}} \frac{\partial r}{\partial x} = \frac{x}{r^2}, \quad (2.4)$$

but the derivative of the potential can't be related to the potential itself as in the 3D case. On the other hand (2.4) can't be used directly since it is the solution for free space instead of two parallel plates stretching to infinity.

Similarly as in (2.3) one finds that the potential between two parallel plates at $y = \pm a$ can be described in the form

$$\tilde{\phi}(x, y) = \sum_{m=1}^{\infty} A_m \exp(-k_m|x|) \cos(k_m y),$$

where again $k_m = m\pi/2a$. Its derivative far away from the source then approaches

$$\frac{\partial \tilde{\phi}}{\partial x} \approx -k_1 \tilde{\phi}.$$

See also [3, Chapter 2.10] although for a slightly different problem.

2.1 Simple Geometries

Simple and yet fast methods exist for the calculation of the electric potential inside geometries whose boundary coincide with the boundary of the rectangular mesh. They are mainly used with open boundaries in particle trackers which compute the electromagnetic field in the vicinity of the bunch only. But they could also be used to initialize the electromagnetic fields in a domain containing a bend if the relativistic factor is large and the bending angle small. The result is then a possibly crude approximation to a solution with proper boundaries.

In free space the potential due to a collection of charged particles is the superposition of the potentials due to every particle individually,

$$\tilde{\phi}(\mathbf{r}) = \frac{1}{4\pi\epsilon_0} \sum_{\alpha=0}^{N_p-1} \frac{q_\alpha}{|\mathbf{r} - \mathbf{r}_\alpha|}, \quad (2.5)$$

where \mathbf{r}_α and q_α are the position and charge respectively of particle α . To calculate the potential at every mesh node needs $N_g \cdot N_p$ operations, where N_g is the number of cells and

N_p the number of particles. This direct computation of the potential becomes inefficient for increasing mesh sizes and particle numbers. Thus better algorithms are needed.

Instead of treating the collection as individual point sources one can describe them as a charge density. Then the potential at any point in space is

$$\tilde{\phi}(\mathbf{r}) = \frac{1}{4\pi\epsilon_0} \int_{\mathbb{R}^3} G(\mathbf{r} - \mathbf{r}') \tilde{\rho}(\mathbf{r}') d\mathbf{r}', \quad (2.6)$$

with $G(\mathbf{r}) = \frac{1}{|\mathbf{r}|}$. Thus the potential can be described by a convolution. To calculate the convolution in direct space is expensive. But, as is well known, in frequency space a convolution reduces to a simple multiplication,

$$\tilde{\phi} = \mathcal{F}^{-1} (\mathcal{F}(G)(\mathbf{k}) \cdot \mathcal{F}(\tilde{\rho})(\mathbf{k}))(\mathbf{r}), \quad (2.7)$$

where \mathcal{F} denotes the Fourier transformation. The integral in (2.6) reduces to finite sums for a charge density that is discretized on a mesh. Also instead of the continuous Fourier transformation in (2.7) a Discrete Fourier Transform (DFT) is used. Contrary to the continuous Fourier transformation the DFT works only for periodic data. At first glance it seems that this technique is not applicable here since the Gauss function is not periodic. Indeed, as we will see, it is only applicable when the domain is surrounded by open boundaries. Then the computational costs reduce to $N_p + N_g \log N_g$ if the FFT is used.

A more general approach is to discretize the Laplace operator in (2.1) by means of finite-differences, finite-volumes or finite-elements and to solve the resulting system of linear equations iteratively. This technique can of course also be applied to domains that are subject to this section but it will be discussed in more detail in Section 2.2.

2.1.1 Boundary Conditions

Equation (2.1) is a boundary value problem, thus it cannot be solved without appropriate boundary conditions. To simulate charged particles inside metal tubes formulations for the perfect electric conductor and the open boundary are needed.

Open Boundaries

For the approach with the Green function a cyclic convolution has to be applied to obtain open boundaries [27]. For this the domain size is doubled in each dimension. The data of the charge density is then padded with zeros outside of the original domain while the Green function is mirrored. Then the convolution is calculated with help of the FFT. Inside of the original domain this yields the correct result. The result outside of the original domain is not correct though it is also not used any longer.

Pefect Electric Conductor

The effect of a perfectly conducting surface on the electric potential due to a collection of charged particles is the same as that of virtual image charges. For every particle of the collection there is a virtual particle of opposite charge whose position and velocity are

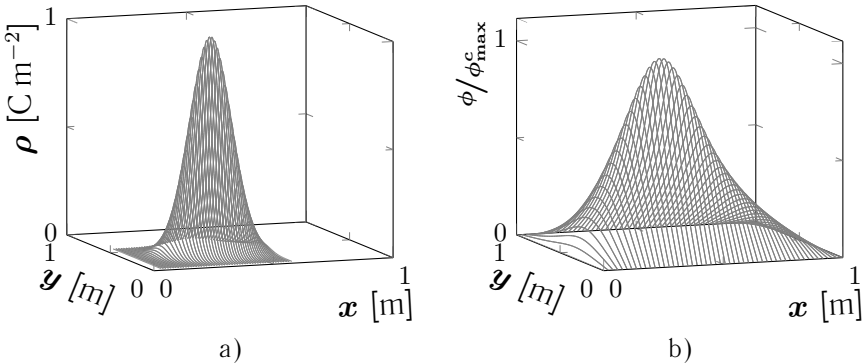


Figure 2.3: The charge density, $\exp(-((x - 0.372)^2 + (y - 0.372)^2)) \text{ C m}^{-2}$, and the resulting electric potential in a 2-dimensional domain with PEC on all four boundaries normalized such that its maximum is 1.

mirrored by the surface. This ensures that the potential on the surface vanishes. Thus there is no gradient along the surface and therefore the tangential electric field also vanishes.

If a domain has PEC surfaces on opposite sides, e.g. at $x = 0$ and $x = L_x$, then the charged particles are mirrored infinitely many times by virtual particles. A particle at position $(x_\alpha, y_\alpha, z_\alpha)$ with charge q causes a virtual particle with charge $-q$ at $(-x_\alpha, y_\alpha, z_\alpha)$ due to the PEC surface at $x = 0$ and one at $(2L_x - x_\alpha, y_\alpha, z_\alpha)$ due to the PEC surface at $x = L_x$. These virtual particles in turn cause virtual particles with charge q at $(-2L_x + x_\alpha, y_\alpha, z_\alpha)$ and at $(2L_x + x_\alpha, y_\alpha, z_\alpha)$. The latter virtual particles cause more virtual particles. Thus an infinite set of particles are caused.

Image charges can be used in combination with the approach with the Green function as long as the domain does not have PEC boundaries on opposite sides. To keep the mesh small a shifted Green function is then used [43]. The contribution due to the original particle collection is calculated with the regular Green function while the one due to the image charges is calculated with the shifted Green function. They are calculated separately each with open boundaries on all sides.

A different technique is needed to compute the potential inside domains with PEC boundaries on opposite sides. For this [3, 60] the electric potential and the charge density are expressed as series of sines $\sin(\alpha_k x)$, where $\alpha_k = k\pi/L$, $k \in \mathbb{N}^+$ and L is the length of the domain. The coefficients for the series can be calculated by the discrete sine transform (DST). The choice of DST ensures that the solution vanishes both at $x = 0$ and at $x = L$. The Poisson equation in one dimension is then formulated as a finite-difference,

$$\frac{\partial^2 \tilde{\phi}(x)}{\partial x^2} \simeq \frac{\tilde{\phi}_{j-1} - 2\tilde{\phi}_j + \tilde{\phi}_{j+1}}{\Delta x^2} = -\frac{1}{\varepsilon_0} \tilde{\rho}_j. \quad (2.8)$$

The coefficients of the DST, $\hat{\phi}$ and $\hat{\rho}$ are calculated by

$$\begin{aligned}\hat{\phi}^k &= \sum_{j=0}^{N-1} \sin\left(\frac{\pi}{N+1}(k+1)(j+1)\right) \tilde{\phi}_j, \quad k = 1 \dots N, \\ \hat{\rho}^k &= \sum_{j=0}^{N-1} \sin\left(\frac{\pi}{N+1}(k+1)(j+1)\right) \tilde{\rho}_j,\end{aligned}$$

The original data is regained by

$$\begin{aligned}\tilde{\phi}_j &= \frac{2}{N+1} \sum_{k=1}^N \sin\left(\frac{\pi}{N+1}k(j+1)\right) \hat{\phi}^{k-1}, \\ \tilde{\rho}_j &= \frac{2}{N+1} \sum_{k=1}^N \sin\left(\frac{\pi}{N+1}k(j+1)\right) \hat{\rho}^{k-1}.\end{aligned}\tag{2.9}$$

By inserting (2.9) into (2.8) one gets

$$\begin{aligned}\sum_{k=1}^N \left(\sin\left(\frac{\pi}{N+1}kj\right) - 2 \sin\left(\frac{\pi}{N+1}k(j+1)\right) + \sin\left(\frac{\pi}{N+1}k(j+2)\right) \right) \hat{\phi}^{k-1} \\ = \sum_{k=1}^N 2 \left(\cos\left(\frac{\pi}{N+1}k\right) - 1 \right) \sin\left(\frac{\pi}{N+1}k(j+1)\right) \hat{\phi}^{k-1} \\ = -\frac{\Delta x^2}{\varepsilon_0} \sum_{k=1}^N \sin\left(\frac{\pi}{N+1}k(j+1)\right) \hat{\rho}^{k-1}.\end{aligned}$$

From this then follows that

$$\hat{\phi}^k = -\frac{\Delta x^2}{\varepsilon_0} \frac{\hat{\rho}^k}{2 \left(\cos\left(\frac{\pi}{N+1}(k+1)\right) - 1 \right)}.$$

The electric potential is then gained by an inverse DST. The same procedure is applicable in two and three dimensions for domains that are surrounded by PEC. An example in two dimensions is shown in Fig. 2.3.

This technique of expansion into series of sines can also be used for the simulation of particle bunches propagating in tubes [28] with open boundaries in the direction of propagation and PEC boundaries on the remaining surfaces. In the case of rectangular tubes in three dimensions a DST is applied in the transverse directions. Instead of (2.9) one then gets

$$\begin{aligned}\tilde{\phi}_{j,k,l} &= \frac{4}{N_x N_y} \sum_{m=1}^{N_x} \sum_{n=1}^{N_y} \sin\left(\frac{\pi}{N_x+1}m(j+1)\right) \sin\left(\frac{\pi}{N_y+1}n(k+1)\right) \hat{\phi}_l^{m-1,n-1}, \\ \tilde{\rho}_{j,k,l} &= \frac{4}{N_x N_y} \sum_{m=1}^{N_x} \sum_{n=1}^{N_y} \sin\left(\frac{\pi}{N_x+1}m(j+1)\right) \sin\left(\frac{\pi}{N_y+1}n(k+1)\right) \hat{\rho}_l^{m-1,n-1}.\end{aligned}$$

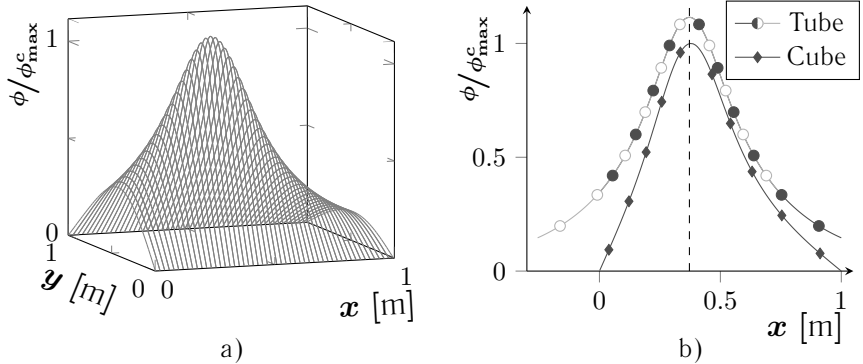


Figure 2.4: a) The electric potential in a 2-dimensional domain with PEC on $y = 0$ and $y = 1$ and open boundaries on the other two boundaries for the same charge density as in Fig. 2.3 and normalized by the same factor, b) comparison of the electric potentials as in a) and Fig. 2.3 b) at $y = 0.372$ m. Furthermore the first graph is mirrored at its maximum, $x = 0.372$ m, to show its symmetry and hence the independence of the solution of the distance to the boundary.

Inserted into the finite-difference representation of the Poisson equation one gets

$$\frac{\hat{\phi}_{l-1}^{m,n} - 2\hat{\phi}_l^{m,n} + \hat{\phi}_{l+1}^{m,n}}{\Delta z^2} - \gamma_{m,n}^2 \hat{\phi}_l^{m,n} = -\frac{1}{\varepsilon_0} \hat{\rho}_l^{m,n}, \quad (2.10)$$

where $\gamma_{m,n}^2 = \frac{2}{\Delta x^2} \left(1 - \cos \left(\frac{\pi}{N_x+1} (m+1) \right) \right) + \frac{2}{\Delta y^2} \left(1 - \cos \left(\frac{\pi}{N_y+1} (n+1) \right) \right)$.

The potential in z-direction has to diminish exponentially as $\exp(-\gamma_{m,n} z)$ outside of the support of the charge density. This can be seen from (2.10) for the case that the right hand side vanishes. In order for the potential to be continuous at the boundary

$$\begin{aligned} \hat{\phi}_{-1}^{m,n} &= \exp(-\gamma_{m,n} \Delta z) \hat{\phi}_0^{m,n}, \\ \hat{\phi}_{N_z}^{m,n} &= \exp(-\gamma_{m,n} \Delta z) \hat{\phi}_{N_z-1}^{m,n}, \end{aligned}$$

has to hold.

Finally the $N_x \cdot N_y$ independent 1-dimensional systems of equations of size N_z have to be solved to receive $\hat{\phi}_l^{m,n}$. It then remains to apply an inverse DST in the transverse directions. The same technique can also be used for the case of two parallel plates in two dimensions. An example is shown in Fig. 2.4 [28].

2.2 Complicated Geometries

For geometries that are not as simple as a cube or a cylinder with constant radius other methods than those introduced in Section 2.1 have to be used. In principle any of the discretization methods such as the finite-element method, the finite-volume method or the finite-difference method will be discussed here due to its simplicity compared to the other methods. Simplicity of computation is a key towards the simulation of a bunch compressor. For this reason an orthogonal equidistant mesh is used. In 3D this yields

$$-\Delta_{\text{FD}} \tilde{\phi}(\mathbf{r}) = \sum_{i=x,y,z} \frac{-\tilde{\phi}(\mathbf{r} - h_i \mathbf{e}_i) + 2\tilde{\phi}(\mathbf{r}) - \tilde{\phi}(\mathbf{r} + h_i \mathbf{e}_i)}{h_i^2} = \frac{\tilde{\rho}(\mathbf{r})}{\varepsilon_0} \quad \forall \mathbf{r} \in \Omega. \quad (2.11)$$

Combined with an appropriate treatment of the boundaries this discretization will result in a system of equations,

$$\mathcal{M}\mathbf{y} = \mathbf{x},$$

that has to be solved. For small mesh sizes this may be solved on a single computer but often the meshes are too big. The sparse matrix \mathcal{M} is symmetric and positive definite. Though the symmetry depends on the treatment of the boundaries. For the solution the conjugate gradient method with smoothed aggregation-based algebraic multigrid preconditioning as in [30] will be used.

2.2.1 Boundary Conditions

At the boundary of the domain the solution has to satisfy the conditions as described in (2.1).

Perfect Electric Conductor

Cells at the boundary are in general neither fully inside nor fully outside of the domain. Thus there is not a single way how to treat them. In (2.11) this case is not handled. The simplest method is the staircase approximation where all boundary cells are treated as if fully inside or fully outside the domain depending on the ratio between the volume inside the domain, v_{ijk} and the total volume of one cell, V . Let \mathbf{r} be the position of a mesh node next to the boundary inside the domain, $\mathbf{r}' = \mathbf{r} + h_i \mathbf{e}_i$ for $i = x, y$ or z the position of a neighboring mesh node located just outside of the domain. Furthermore the location where the cell edge that connects the two positions crosses the boundary is denoted by $\mathbf{r}^* = \mathbf{r} + sh_i \mathbf{e}_i$ where $0 \leq s < 1$. For the staircase approximation one sets $\tilde{\phi}(\mathbf{r}') = 0$ and, if less than half of the cell is inside the domain, then one also sets $\tilde{\phi}(\mathbf{r}) = 0$. This leads to a convergence rate with respect to the cell size, h , that is approximately linear.

A faster convergence is achieved by linear extrapolation of the boundary value:

$$(1 - s)\tilde{\phi}(\mathbf{r}) + s\tilde{\phi}(\mathbf{r}') = 0.$$

With this method the convergence rate is approximately quadratic.

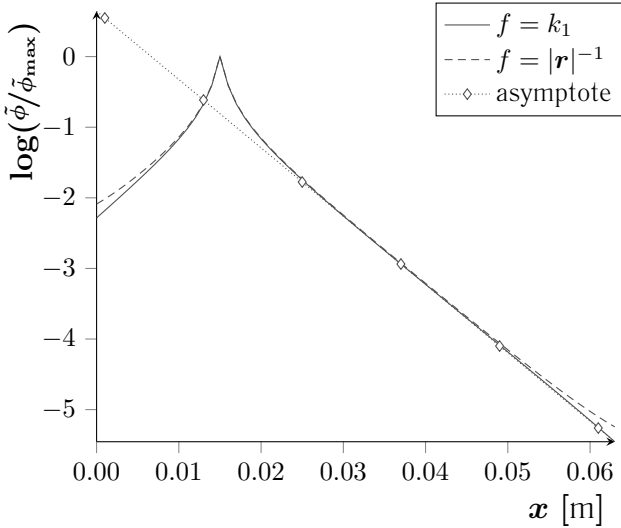


Figure 2.5: The electric potentials for $f = k_1 = \pi/L_y$, $f = |r|^{-1}$ and their asymptote for $x \rightarrow \infty$ along a line of a small electric charge in a 2-dimensional domain bounded by PEC at $y = 0$ and $y = L_y$ and open boundaries at $x = 0$ and $x = L_x$. The ratio of the lengths of the domain is $L_x = 2L_y$.

A third method is the quadratic extrapolation. Let $\mathbf{r}'' = \mathbf{r} - h_i \mathbf{e}_i$ be the position of the cell node next to \mathbf{r} one cell further inside the domain. The quadratic extrapolation is then given by

$$\tilde{\phi}(\mathbf{r}') = ah_i^2 + bh_i + c,$$

where

$$\begin{aligned} c &= \tilde{\phi}(\mathbf{r}), \\ ah_i^2 - bh_i + c &= \tilde{\phi}(\mathbf{r}''), \\ as^2 + bs + c &= 0. \end{aligned}$$

When solved for a , b and c this yields

$$\tilde{\phi}(\mathbf{r}') = \frac{2(s-1)}{s}\tilde{\phi}(\mathbf{r}) - \frac{s-1}{s+1}\tilde{\phi}(\mathbf{r}'').$$

For the case that \mathbf{r}'' is also outside the domain a slightly more complicated solution can be found by the same procedure. Let $\mathbf{r}^{**} = \mathbf{r} - th_i$ be exactly on the boundary between \mathbf{r} and \mathbf{r}'' . The extrapolation is then

$$\begin{aligned}\tilde{\phi}(\mathbf{r}') &= \frac{(s-1)(t+1)}{st} \tilde{\phi}(\mathbf{r}), \\ \tilde{\phi}(\mathbf{r}'') &= \frac{(s+1)(t-1)}{st} \tilde{\phi}(\mathbf{r}).\end{aligned}$$

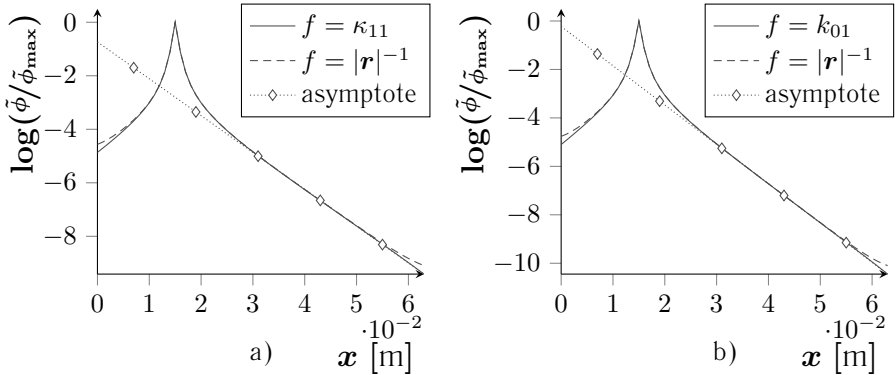


Figure 2.6: The electric potentials of a small electric charge along a line in different domains and for different approximations of the derivative of the potential at the open boundary. a) The domain is a 3-dimensional rectangular tube with open boundaries at $x = 0$ and $x = L_x$ and PEC on the other four boundary faces. Here $L_x = 2L_y = 2L_z$ was used. The asymptote for $x \rightarrow \infty$ is $\exp(s_{rt} - \kappa_{11}x)$ where $\kappa_{11} = \pi\sqrt{1/L_y^2 + 1/L_z^2}$. b) The domain is a 3-dimensional round tube with open boundaries at $x = 0$ and $x = L_x$ and PEC at $y^2 + z^2 = R^2$. Here $L_x = 4R$ was used. The asymptote for $x \rightarrow \infty$ is $\exp(s_{rt} - k_{01}x)$ where $k_{01} = \lambda_{01}/R$ and $\lambda_{01} \sim 2.4048$ is the smallest zero of the Bessel function J_0 .

Unfortunately the quadratic extrapolation renders the matrix \mathcal{M} non-symmetric. The authors of [30] report that the conjugate gradient algorithm still converged. They argue that the matrix is still positiv definite and only ‘mildly’ non-symmetrix. The convergence rate they found using this extrapolation is also approximately quadratic.

Open Boundaries

The finite-difference approximation of the Robin boundary condition on Γ_1 in (2.1) in finite-differences is

$$\frac{\tilde{\phi}(\mathbf{r} - h_x \mathbf{e}_x) - \tilde{\phi}(\mathbf{r} + h_x \mathbf{e}_x)}{2h_x} + f\tilde{\phi}(\mathbf{r}) = 0,$$

where f is best approximated by either $|\mathbf{r}_{\text{bunch}} - \mathbf{r}|^{-1}$ or $k_1 = \frac{\pi}{L}$ depending on the distance to the bunch. Here L is the width of the domain at Γ_1 in Fig. 2.2. The further away from the charges the better becomes the latter approximation. This behavior can be observed in Fig. 2.5 for a 2-dimensional rectangular domain with PEC boundaries on the opposite sides in y -direction and open boundaries on the other two sides. The domain corresponds to a bend as in Fig. 2.2 with bending angle zero. The graph shows the electric potentials of a point source along a line for the two approximations of its derivative. The line runs parallel to the x -axis through the location of the source. The potentials are normalized by the maximum value of the solution gained with $f = k_1$. Both solutions approximate the exponential asymptote $\exp(s - k_1 x)$ for x large enough.

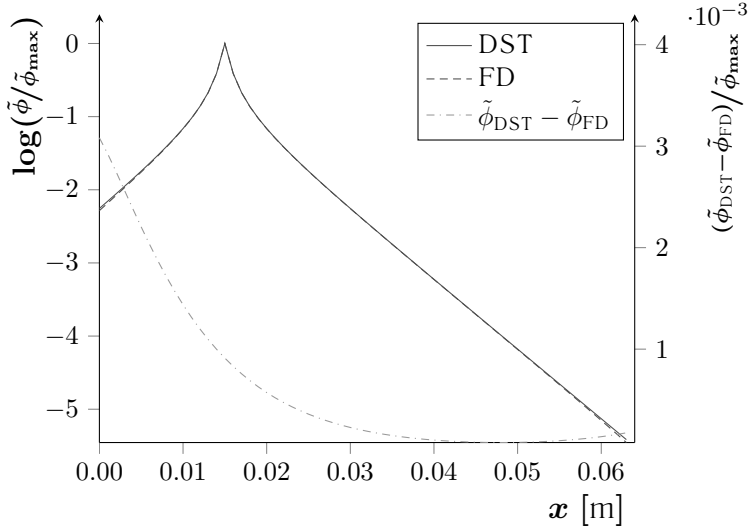


Figure 2.7: The electric potentials of a small electric charge along a line in a 2-dimensional domain bounded by PEC at $y = 0$ and $y = L_y$ and open boundaries at $x = 0$ and $x = L_x$ computed using two different methods. The first method uses a discrete sine transform and is described in Section 2.1. On the other hand the method described in this section was used with $f = k_1$. The ratio of the lengths of the domain is as in Fig. 2.5 $L_x = 2L_y$.

In Fig. 2.5 it is apparent that the solution for $f = |\mathbf{r}_{\text{bunch}} - \mathbf{r}|^{-1}$ is not symmetric with respect to the position of the source. Thus the distances of the charge to the open boundaries have an influence on the solution. The estimation of the derivative is too small. The same behavior can also be observed for a 3-dimensional rectangular tube and for a 3-dimensional cylinder in Fig. 2.6.

The finite-difference method as described in this section applied to the Poisson equation on simple geometries yields results that agree very well with the ones computed with the methods as described in the previous section. For the case of a charge in the 2-dimensional domain as in Fig. 2.5 this can be seen in Fig. 2.7.

Chapter Three

Propagation of Particles

The loop in Fig. 1.8 comprises four steps of which one involves the electromagnetic field only. This step will be discussed in the next chapter. From the three remaining steps one involves the particles only while the two other steps are interfaces between the particles and the fields. The three steps will be discussed in the order of occurrence in a simulation.

3.1 Interpolation of Electromagnetic Fields

An interpolation of the electromagnetic field is needed to receive the fields at the positions of the particles since the fields are calculated only at discrete locations in space. In principle any interpolation,

$$\mathbf{F}(\mathbf{r}_\alpha) = \mathbf{F}_\alpha = \sum_{i,j} w_{i,j}(\mathbf{r}_\alpha) \tilde{\mathbf{F}}_{i,j}, \quad (3.1)$$

can be used, provided $\sum_{i,j} w_{i,j}(\mathbf{r}_\alpha) = 1$. However gravitation-like forces and self-forces may occur if different weighting functions are used than for the interpolation of the current density [45, Chapter 8-5]. Furthermore the conservation of momentum may not be guaranteed.

The above described procedures to compute the fields anywhere inside the cells have the disadvantage that the resulting local fields don't fulfill Maxwell's equations. This means in particular that the magnetic field is not divergence-free. In [61] it is found that the subtle effect of trapping charged particles in the cusp region of earths magnetosphere is much better reproduced when using their improved procedure to calculate the magnetic field.

The method proposed in [61] calculates the vector potential from the magnetic field by means of the FFT:

$$\mathcal{F}(\tilde{\mathbf{B}})(\mathbf{k}) = -i\mathbf{k} \times \mathcal{F}(\tilde{\mathbf{A}})(\mathbf{k}), \quad (3.2)$$

where the FFT is denoted by \mathcal{F} . To that end the magnetic field is extended by a factor of two in every direction by mirroring the initial field before applying the FFT. This is done in order to avoid effects due to the non-periodicity of the magnetic field. (3.2) is then inverted by

$$\mathcal{F}(\tilde{\mathbf{A}})(\mathbf{k}) = i\frac{\mathbf{k}}{k^2} \times \mathcal{F}(\tilde{\mathbf{B}})(\mathbf{k}),$$

where the Coulomb gauge, $\nabla \cdot \tilde{\mathbf{A}} = 0$, is assumed. The vector potential is then obtained by means of an inverse FFT. The resulting vector potential is then interpolated at the position of the particles with cubic splines from which finally the local magnetic field is calculated.

The above described procedure is expensive when adapted to time dependent magnetic fields. A simpler method is described in [62]. Instead of an interpolation as in (3.1) these authors propose to interpolate the fields by

$$\begin{aligned} \tilde{\mathbf{B}}_x(x, y, z) = & \hat{x}(U_{i+1,j,k} + (\hat{y} - 1/2) U_{i+1,j,k}^y + (\hat{z} - 1/2) U_{i+1,j,k}^z) \\ & + (1 - \hat{x})(U_{i,j,k} + (\hat{y} - 1/2) U_{i,j,k}^y + (\hat{z} - 1/2) U_{i,j,k}^z) \\ & + \hat{x}(1 - \hat{x})(V_{i,j+1,k}^x - V_{i,j,k}^x + W_{i,j,k+1}^x - W_{i,j,k}^x) \end{aligned}$$

where $U_{i,j,k} = \tilde{\mathbf{B}}_{x; i,j+1/2,k+1/2}$, $V_{i,j,k} = \tilde{\mathbf{B}}_{y; i+1/2,j,k+1/2}$, $W_{i,j,k} = \tilde{\mathbf{B}}_{z; i+1/2,j+1/2,k}$ and the superscripts denote spatial derivatives along the corresponding directions. Furthermore $\hat{x} = \frac{x}{\Delta x} - i$ and similarly \hat{y} and \hat{z} while i, j, k are chosen such that $0 \leq \hat{x}, \hat{y}, \hat{z} < 1$. The other components of the magnetic field are found in an analogous manner. Contrary to the interpolation as proposed in [61] the resulting local magnetic field is not continuous at the cell boundaries nor are its derivatives but the divergence vanishes inside the cell.

3.2 Temporal Integration

The next step in the loop of a simulation is to update the momenta and positions of the particles. Criteria for the choice of an integration scheme are consistency, accuracy, stability and efficiency.

Consistency

Important physical properties of the system of N charged particle propagating in external electromagnetic fields should be reproduced by the integration scheme. First, finite-differences have to approximate the derivatives they represent as the step size approaches zero, e.g.

$$\lim_{\Delta s \rightarrow 0} \frac{x(s^n + \Delta s) - x(s^n)}{\Delta s} = \frac{dx}{ds}.$$

Then the resulting scheme has to be symmetric under time reversal as are the laws of motion, when neglecting any energy dissipation [63]. Finally the scheme should conserve the energy of the system as well as the phase space density, that is, it should be symplectic. Symplectic integrators model the update of the positions and momenta by

$$\begin{aligned}\frac{d\mathbf{r}}{dt} &= \nabla_{\mathbf{P}} H, \\ \frac{d\mathbf{P}}{dt} &= -\nabla_{\mathbf{r}} H,\end{aligned}$$

where H is the Hamiltonian of the particle, $H(\mathbf{r}, \mathbf{P}) = q\tilde{\phi} - \sqrt{m_0^2 c^4 + c^2(\mathbf{P} - q\tilde{\mathbf{A}})^2}$, and $\mathbf{P} = m\gamma\dot{\mathbf{r}} + q\tilde{\mathbf{A}}$ is the canonical momentum. The true Hamiltonian is then well approximated.

Accuracy

The result of a simulation should be a good approximation of the real system. The deviation of the simulation is a result of round-off errors and truncation errors. The round-off errors are caused by the way numbers are represented in computer memory notably the finite length of a word. This error is usually negligible compared to the truncation error. The latter describes the difference between a derivative and its finite-difference representation. This error may be reduced with a more elaborate representation of the derivative though at the cost of increased storage, reduced efficiency or reduced stability.

Stability

Non-physical solutions for the discretized equations must not grow to a large cumulated error. One could consider the application of implicit schemes. They allow for large time steps while keeping the cumulated errors low. A possible drawback of such a choice is the increased costs to calculate one time step particularly when the solution has to be calculated iteratively. For simulations with a large number of particles implicit schemes may become unfeasible.

Efficiency

A large number of particles are needed in order to reduce the noise caused by abrupt variations in the current density. Furthermore a lot of time steps are needed due to possible stability criteria of both the integration methods for the particles and for the fields as well as due to accuracy requirements. Thus efficiency of the integration methods is utterly important.

3.2.1 Störmer-Verlet Method

The Störmer-Verlet method for the propagation of particles [63], also called Boris-Buneman method, is a very simple method yet it is unconditionally stable due to its implicit character. It is given by

$$\frac{\mathbf{r}^{n+1/2} - \mathbf{r}^n}{\Delta t} = \frac{c \mathbf{p}^n}{2 \gamma^n} = \nabla_{\mathbf{P}} H(\mathbf{r}^n, \mathbf{P}^n), \quad (3.3)$$

$$c \frac{\mathbf{p}^{n+1} - \mathbf{p}^n}{\Delta t} = \frac{q}{m_0} \left(\mathbf{E}^{n+1/2} + c \frac{\mathbf{p}^{n+1} + \mathbf{p}^n}{2\gamma^{n+1/2}} \times \mathbf{B}^{n+1/2} \right) \\ \simeq -\frac{1}{2m_0} \left(\nabla_{\mathbf{r}} H(\mathbf{r}^{n+1/2}, \mathbf{P}^n) + \nabla_{\mathbf{r}} H(\mathbf{r}^{n+1/2}, \mathbf{P}^{n+1}) + q \frac{d\mathbf{A}^{n+1/2}}{dt} \right), \quad (3.4)$$

$$\frac{\mathbf{r}^{n+1} - \mathbf{r}^{n+1/2}}{\Delta t} = \frac{c \mathbf{p}^{n+1}}{2 \gamma^{n+1}} = \nabla_{\mathbf{P}} H(\mathbf{r}^n, \mathbf{P}^n), \quad (3.5)$$

where $\mathbf{p} = \beta \gamma$ and where both \mathbf{A}^n and \mathbf{A}^{n+1} (hidden in \mathbf{P}^n and $\mathbf{P}^{n+1/2}$ respectively) are approximated by $\mathbf{A}^{n+1/2}$. By means of a change of variable [64] this method is fast despite its implicit character. To that end (3.4) is split into three separate steps. The first and the third step update the velocity using the electric field only. The second step uses only the magnetic field for the update of the velocity. This second step is fully described by a pure rotation of the momentum. The three steps of the momentum update are given by

$$\frac{\mathbf{p}_- - \mathbf{p}^n}{\Delta t} = \frac{q}{2m_0 c} \mathbf{E}^{n+1/2}, \quad (3.6)$$

$$\frac{\mathbf{p}_+ - \mathbf{p}_-}{\Delta t} = \frac{\mathbf{p}_+ + \mathbf{p}_-}{2} \times \boldsymbol{\Omega}^{n+1/2}, \quad (3.7)$$

$$\frac{\mathbf{p}^{n+1} - \mathbf{p}_+}{\Delta t} = \frac{q}{2m_0 c} \mathbf{E}^{n+1/2}. \quad (3.8)$$

Here $\boldsymbol{\Omega}^{n+1/2} = \frac{q}{m_0 \gamma_-} \mathbf{B}^{n+1/2}$ is the gyrofrequency and, since (3.7) is a pure rotation of the momentum, $\gamma_- = \sqrt{1 + \mathbf{p}_-^2} = \sqrt{1 + \mathbf{p}_+^2} = \gamma_+ = \gamma^{n+1/2}$. The axis of the rotation is $\frac{\mathbf{p}^{n+1/2}}{\Omega^{n+1/2}}$ and the angle is $-2 \tan(\Theta^{n+1/2})$, where $\Theta^{n+1/2} = \frac{\Delta t}{2} \boldsymbol{\Omega}^{n+1/2}$. The rotation operator, \mathcal{R} , is then

$$(1 + |\boldsymbol{\Theta}|^2) \mathcal{R} = (1 - |\boldsymbol{\Theta}|^2) \mathcal{I} + 2 \boldsymbol{\Theta} \otimes \boldsymbol{\Theta} - 2 \boldsymbol{\Theta} \times \mathcal{I},$$

where \mathcal{I} is the unit tensor. In this form it is easy to invert (3.7):

$$\begin{aligned}\Theta &= \frac{\Delta t}{2} \Omega^{n+1/2}, \\ s &= \frac{2}{1 + |\mathbf{u}|^2} \mathbf{u}, \\ \mathbf{w} &= \mathbf{p}_- + \mathbf{p}_- \times \mathbf{u}, \\ \mathbf{p}_+ &= \mathbf{p}_- + \mathbf{w} \times \mathbf{s}.\end{aligned}$$

The resulting method is of second order in Δt but it is not strictly symplectic in contrast to a proper Störmer-Verlet method [65]. This is due to the approximation made to \mathbf{A}^n and \mathbf{A}^{n+1} . Nonetheless energy and phase space are very well conserved. Furthermore the method is time reversible and the computational cost per particle is also moderate since it needs a single evaluation of the fields per step and since it is easily inverted.

There is also a version of the Boris-Buneman method that adapts the time step size [66]. Furthermore there is a version in which a corrector step follows a predictor step to improve the estimate of the fields [67].

3.2.2 Symplectic Runge-Kutta Methods

Classical Runge-Kutta methods,

$$\begin{aligned}y^{n+1} &= y^n + \Delta t \sum_{i=1}^s b_i k_i, \\ k_i &= f \left(t^n + c_i \Delta t, y^n + \Delta t \sum_{j=1}^{i-1} a_{ij} k_j \right),\end{aligned}$$

where $c_i = \sum_{j=1}^{i-1} a_{ij}$, is a broadly used class of explicit methods. In particular the fourth order Runge-Kutta method is popular. Their disadvantage compared to the Boris-Buneman method is that more evaluations of the fields are needed and that they do not conserve energy and phase space density well. The symplectic variants [68] are of course good at conserving those quantities but they are implicit and can't be inverted analytically. Thus the solutions have to be computed iteratively which is slow [69]. The electromagnetic fields have to be updated with every iteration step as well. Symplectic Runge-Kutta methods don't seem to be viable options considering the large number of particles needed in the simulation of particle accelerators using PIC methods.

3.3 Calculation of Current

Numerical methods for the integration of Maxwell's equations rely on methods to compute the current density that conserve the electric charge in order to comply to Gauss's law. Basically charge conservation can be achieved in two different ways: (i) By computing the charge current with a method that does not fulfill charge conservation followed by a correction step, or (ii) directly with appropriate methods.

3.3.1 Enforcing Gauss's Law

The propagation of particles is computationally expensive, thus one is tempted to simplify the steps that are involved. One such step could be the calculation of the current density. An early method for this reads [45, p. 358 ff.]

$$\tilde{\mathbf{J}}_{i,j,k}^{n+1/2} = \sum_{\alpha} q_{\alpha} \mathbf{v}_{\alpha}^{n+1/2} \frac{S^1(\mathbf{P} - \mathbf{r}_{\alpha}^n) + S^1(\mathbf{P} - \mathbf{r}_{\alpha}^{n+1})}{2},$$

where $S^1(\mathbf{r}) = S_{\Delta x}^1(\mathbf{r}_x)S_{\Delta y}^1(\mathbf{r}_y)S_{\Delta z}^1(\mathbf{r}_z)$, \mathbf{P} is the location ($i \Delta x$, $j \Delta y$, $k \Delta z$) relative to the origin of the mesh and $\tilde{\mathbf{J}}_{i,j,k}$ is the charge current at \mathbf{P} . These values for the current density are then averaged with their neighbors to receive the current density at the same location as the electric field:

$$\tilde{\mathbf{J}}_{x; i+1/2, j, k}^{n+1/2} = \frac{\tilde{\mathbf{J}}_{x; i, j, k}^{n+1/2} + \tilde{\mathbf{J}}_{x; i+1, j, k}^{n+1/2}}{2}.$$

The resulting current density violates the charge conservation even for particles moving parallel to the mesh edges. The electric field that is derived with the defective current density will violate the divergence condition in (1.4). Several solutions exist to correct the electric field.

Boris Method

Denoting the uncorrected solution of the electric field by $\tilde{\mathbf{E}}^{* n+1}$ we can state that in general

$$\nabla_{\text{FD}} \cdot \tilde{\mathbf{E}}^{* n+1} \neq \frac{\tilde{\rho}^{n+1}}{\epsilon_0}.$$

A solution for the electric field that satisfies Gauss's law, $\tilde{\mathbf{E}}^{n+1}$, can be found by introducing a correcting potential $\tilde{\phi}^{n+1}$,

$$\tilde{\mathbf{E}}^{n+1} = \tilde{\mathbf{E}}^{* n+1} - \nabla_{\text{FD}} \tilde{\phi}^{n+1}.$$

The correcting potential has to solve the equation

$$-\Delta_{\text{FD}} \tilde{\phi}^{n+1} = \frac{\tilde{\rho}^{n+1}}{\epsilon_0} - \nabla_{\text{FD}} \cdot \tilde{\mathbf{E}}^{* n+1}, \quad (3.9)$$

with $\tilde{\phi}^{n+1} = 0$ on PEC boundaries. Thus to correct the electric field the above Poisson's equation has to be solved [64] which is computationally expensive.

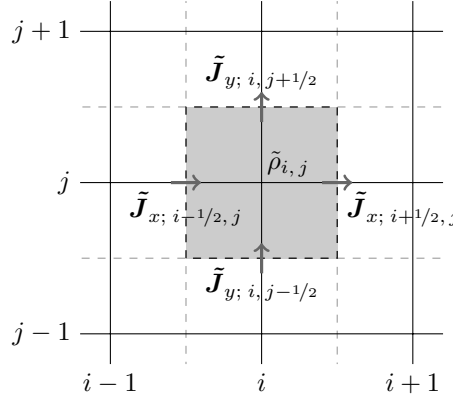


Figure 3.1: Situation when calculating the charge current. In solid line the primal grid and in dashed line the dual grid. The difference of charge inside a dual cell between two steps has to be equal the difference between charge flowing in through the boundaries and charge flowing out.

Langdon-Marder Method

A second method [70, 71] is to add a diffusive term to the electric field,

$$\tilde{\mathbf{E}}^{n+1} = \tilde{\mathbf{E}}^{* n+1} + D \Delta t \nabla_{\text{FD}} F^{n+1},$$

where $F^{n+1} = \nabla_{\text{FD}} \cdot \tilde{\mathbf{E}}^{* n+1} - \frac{\tilde{\rho}^{n+1}}{\varepsilon_0}$ and $D \leq \frac{1}{2\Delta t} \frac{\Delta x^2 \Delta y^2}{\Delta x^2 + \Delta y^2}$. This method is equivalent to a Jacobi iteration step for the approximation to the solution of Poisson's equation in Boris's method. Thus if repeated the solution for the electric field converges asymptotically towards the solution of (3.9).

3.3.2 Charge Conserving Current

In order that the charge conservation,

$$\frac{\tilde{\rho}^{n+1} - \tilde{\rho}^n}{\Delta t} + \nabla_{\text{FD}} \cdot \tilde{\mathbf{J}}^{n+1/2} = 0, \quad (3.10)$$

is satisfied one can integrate the charge that swipes over the edges of the dual cells, in the following called Villasenor-Buneman's method. This procedure holds for a single particle as well as for a collection of particles. For particle \$\alpha\$ one gets

$$\tilde{\mathbf{J}}_{x; i+1/2, j, k} = \frac{1}{\Delta t} \int_{t^n}^{t^{n+1}} \int_{Y_{j-1/2}}^{Y_{j+1/2}} \int_{Z_{k-1/2}}^{Z_{k+1/2}} (\mathbf{v}_\alpha(t))_x \tilde{\rho}_\alpha(X_{i+1/2}, y, z, t) dz dy dt,$$

and similarly one also gets the current densities of the other three edges, see Fig. 3.1. With this method (3.10) holds independently of the choice of form function with the restriction that the support of the form function should not interfere with the boundaries of the domain.

Most often it is assumed that particles propagate on linear paths between two time instances. The combination of point charges and linear motion [72] causes jumps in the current density and thus a lot of noise. This noise is reduced when zeroth order [73] or higher order [57] splines are used, though at the cost of increased computational costs. The computational costs can be somewhat lowered if the particles don't propagate on a single straight line. The straight line can be split into d lines [74] where d is the dimensionality of the domain. Each of these lines is parallel to the coordinates of the mesh. There exist $d!$ such paths which are all equivalent. Thus the average of the resulting current densities is taken.

One difficulty when calculating the current density is to correctly identify those sampling points which are affected by the motion of a particle. This difficulty arises when some of the sampling points are only affected during part of the time between two time steps.

When zeroth order splines are used then the simplest case is when a particle remains within one cell of the primal grid. Then only the four sampling points lying on the edges of this cell are affected. When the particle crosses the cell boundary then also sampling points of the neighboring cell are affected. The path of the particle is then split at the boundary, each part is treated the same way as the simple case. The size of the time step for explicit integration methods for Maxwell's equations is limited and so is the number of cell boundary crossings.

The support of higher order splines increases and thus more sampling points are affected by the motion of a particle. Furthermore the size of the support also changes the relevant boundary crossings. For splines of even order the crossing of cell boundaries of the primal grid are relevant while the cell boundaries of the dual grid are relevant for splines of odd order.

The Zigzag scheme [75] reduces the effort to compute cell boundary crossings by splitting every path exactly once while keeping the procedure of how to compute the current from Villasenor-Buneman's method. If the path of a particle does not cross the boundary of a cell (primal or secondary mesh depending on form function) then it is split at the mid-point. On the other hand if the path crosses the cell e.g. in the x-direction then the x-coordinate of the introduced location is changed to that of the boundary while the y- and z-coordinate remain at the mid-point: $\mathbf{r}_{\text{mid}} = (X_{cb}, (\mathbf{r}_y^n + \mathbf{r}_y^{n+1})/2, (\mathbf{r}_z^n + \mathbf{r}_z^{n+1})/2)$, where X_{cb} is the x-coordinate of the cell boundary. This scheme reduces the number of if-statements compared to Villasenor-Buneman's method as described above. Thus the time to calculate the current density is reduced while keeping the error low [75]. The generalization to higher order splines can be carried out in analogy to Villasenor-Buneman's method [76].

A different approach is taken for the Density Decomposition scheme [77]. The flow through the faces of a cell can be described by a unique linear combination of the functions

$$\begin{array}{ll} S_{i,j,k}(\mathbf{r}_x, \mathbf{r}_y, \mathbf{r}_z), & S_{i,j,k}(\mathbf{r}_x + \boldsymbol{\delta}_x, \mathbf{r}_y, \mathbf{r}_z), \\ S_{i,j,k}(\mathbf{r}_x, \mathbf{r}_y + \boldsymbol{\delta}_y, \mathbf{r}_z), & S_{i,j,k}(\mathbf{r}_x + \boldsymbol{\delta}_x, \mathbf{r}_y + \boldsymbol{\delta}_y, \mathbf{r}_z), \\ S_{i,j,k}(\mathbf{r}_x, \mathbf{r}_y, \mathbf{r}_z + \boldsymbol{\delta}_z), & S_{i,j,k}(\mathbf{r}_x + \boldsymbol{\delta}_x, \mathbf{r}_y, \mathbf{r}_z + \boldsymbol{\delta}_z), \\ S_{i,j,k}(\mathbf{r}_x, \mathbf{r}_y + \boldsymbol{\delta}_y, \mathbf{r}_z + \boldsymbol{\delta}_z), & S_{i,j,k}(\mathbf{r}_x + \boldsymbol{\delta}_x, \mathbf{r}_y + \boldsymbol{\delta}_y, \mathbf{r}_z + \boldsymbol{\delta}_z), \end{array}$$

such that the charge is conserved. In order to get a unique solution two more conditions are introduced:

1. if the velocity component in one direction vanishes then no charge may flow through the faces in this direction,
2. if the form function is symmetric under permutation of two variables and e.g. $\mathbf{r}_x^n = \mathbf{r}_y^n$ and $\mathbf{r}_x^{n+1} = \mathbf{r}_y^{n+1}$ then the outbound flow through the faces in x-direction should be the same as the one through the faces in y-direction.

The Density Decomposition calculates the same current for a particle as the Villasenor-Buneman method if zeroth order splines are used and if the particle does not cross the cell boundary. For higher order form functions or crossing paths this is in general not true anymore, the differences are small though. The advantages of the Density Decomposition are that arbitrary form functions can be chosen, that the form function can change from time step to time step and thus the handling of particles close to the domain boundary is simplified [78]. Furthermore it is slightly faster than the Villasenor-Buneman method but slower than the Zigzag method [75].

Chapter Four

Finite-Difference Time-Domain

The Finite-Difference Time-Domain method was introduced by Yee [56]. It provides a simple yet powerful tool for the simulation of Maxwell's equations in bounded as well as unbounded domains. However it also shows disadvantages compared to more modern schemes namely its stringent stability criterion and numerical dispersion. In the following a short introduction to the Yee scheme, the Alternating-Direction Implicit scheme as well as the TE/TM scheme is given. Finally an overview over the most common boundary conditions is given.

Criteria for the choice of a scheme are the preservation of divergence in the presence of electric current and the numerical dispersion. Divergence preserving schemes guarantee that the discrete version of Gauss's law,

$$\nabla_{\text{FD}} \cdot \tilde{\mathbf{E}}^n = \frac{\tilde{\rho}^n}{\varepsilon_0}, \quad \forall n > 0,$$

holds provided the initial solution of the electric field $\tilde{\mathbf{E}}^0$ satisfies Gauss's law and provided that the method for the computation of the current density complies with the charge conservation,

$$\frac{\tilde{\rho}^n - \tilde{\rho}^{n-1}}{\Delta t} = -\nabla_{\text{FD}} \cdot \tilde{\mathbf{J}}^{n-1/2}. \quad (4.1)$$

If for a scheme $\nabla_{\text{FD}} \cdot \nabla_{\text{FD}} \times \equiv 0$ is given then the scheme preserves the divergence. This can be shown by calculating the divergence to both sides of the equation for the update of

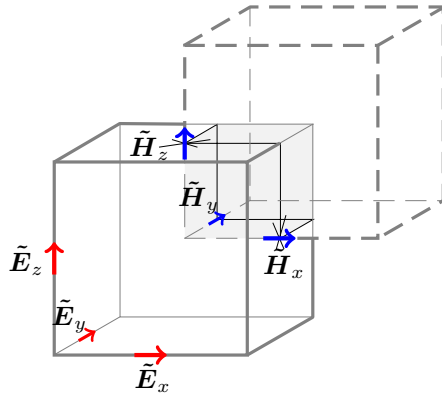


Figure 4.1: The staggered grid for FDTD formulations of Maxwell's equations.

the electric field,

$$\begin{aligned} \nabla_{\text{FD}} \cdot (\tilde{\mathbf{E}}^n - \tilde{\mathbf{E}}^{n-1}) &= \Delta t \left(c^2 \nabla_{\text{FD}} \cdot \nabla_{\text{FD}} \times \tilde{\mathbf{B}}^{n-1/2} - \frac{1}{\epsilon_0} \nabla_{\text{FD}} \cdot \tilde{\mathbf{J}}^{n-1/2} \right) \\ &= \frac{\tilde{\rho}^n - \tilde{\rho}^{n-1}}{\epsilon_0}. \end{aligned}$$

Thus if Gauss's law holds for $\tilde{\mathbf{E}}^{n-1}$ then it also holds $\tilde{\mathbf{E}}^n$.

If a scheme shows large numerical dispersion then it is not able to represent vacuum properly. Electromagnetic waves of different frequencies do not have the same group velocity in a dispersive medium while in vacuum they propagate with the speed of light. In many applications numerical dispersion may not be a big issue but simulations of particle accelerators are very sensitive to it.

4.1 Yee Scheme

The Yee scheme is a widely used and documented scheme for simulations of Maxwell's equations in time-domain. Here only a short overview is given over its advantages as well as disadvantages particularly with respect to the application in this thesis. For further details common textbooks such as [79] may be consulted.

This scheme uses finite-differences on a staggered grid, see Fig. 4.1. The electric components are located on the edges of a primal grid and the magnetic components are located on the edges of a secondary grid. The secondary grid is shifted by half a cell in each dimension

relative to the primal grid. The update of the two fields are also shifted by half a time step:

$$\begin{aligned}\mathbf{v}^{n+1/2} &= \mathbf{v}^{n-1/2} - \mathcal{P}^\top \mathbf{u}^n, \\ \mathbf{u}^{n+1} &= \mathbf{u}^n + \mathcal{P} \mathbf{v}^{n+1/2} - c\Delta t \mathbf{j}^{n+1/2},\end{aligned}\quad (4.2)$$

where

$$\begin{aligned}\mathbf{u}^n &= \begin{pmatrix} \mathbf{E}_x^n \\ \mathbf{E}_y^n \\ \mathbf{E}_z^n \end{pmatrix}, \quad \mathbf{v}^{n+1/2} = Z_0 \begin{pmatrix} \mathbf{H}_x^{n+1/2} \\ \mathbf{H}_y^{n+1/2} \\ \mathbf{H}_z^{n+1/2} \end{pmatrix}, \quad \mathbf{j}^{n+1/2} = Z_0 \begin{pmatrix} \mathbf{J}_x^{n+1/2} \\ \mathbf{J}_y^{n+1/2} \\ \mathbf{J}_z^{n+1/2} \end{pmatrix}, \\ \mathcal{P} &= \begin{pmatrix} \mathcal{D}_z^\top & -\mathcal{D}_y^\top \\ -\mathcal{D}_z^\top & \mathcal{D}_x^\top \\ \mathcal{D}_y^\top & -\mathcal{D}_x^\top \end{pmatrix},\end{aligned}$$

and where \mathcal{D}_ν , \mathcal{D}_ν^\top are the forward and backward difference operators in ν -direction, respectively and $\mu_0 \tilde{\mathbf{H}} = \tilde{\mathbf{B}}$ inside the vacuum tubes of particle accelerators. $\tilde{\mathbf{H}}$ is preferred throughout the chapter mainly due to simplifications in the notation.

The action of e.g. \mathcal{D}_x^\top on \mathbf{H}_z in vacuum is described by

$$\sum_J \mathcal{D}_{x; J, I} \mathbf{H}_{z; J} = -\eta_x \left(\tilde{\mathbf{H}}_{z; i+1/2, j+1/2, k} - \tilde{\mathbf{H}}_{z; i-1/2, j+1/2, k} \right),$$

where we used $\Phi(i, j, k) = I$ to map from the 3-dimensional scalar field $\tilde{\mathbf{H}}_z$ of dimension $N_x \times N_y \times N_z$ to the vector \mathbf{H}_z of length $N_x N_y N_z$ and where $\eta_\nu = c\Delta t / \Delta\nu$, Δt denotes the time step, $\Delta\nu$ the mesh size in ν -direction and c is the speed of light.

This yields an explicit update scheme which has a second order convergence rate with respect to the mesh size. The size of the time step is limited to a relatively small region of stability. Its upper bound in three dimensions is given by [80]

$$(\eta_x^2 + \eta_y^2 + \eta_z^2)^{1/2} \leq 1. \quad (4.3)$$

This is the well known Courant-Friedrichs-Lowy (CFL) condition for the Yee scheme.

The dispersion of a medium describes the dependence of the phase velocity of an electromagnetic wave on its frequency. In free space all components of a light pulse with a spectrum of finite width propagate with the same speed through vacuum. Thus the shape of the pulse is preserved and vacuum in free space has no dispersion. This property is not preserved by the Yee model of electromagnetic fields. The numerical dispersion of this scheme is given by

$$\sin^2(\omega\Delta t/2) = \Sigma_x + \Sigma_y + \Sigma_z \quad (4.4)$$

where $\Sigma_\nu = (\eta_\nu \sin(\frac{k_\nu \Delta\nu}{2}))^2$ and $\mathbf{k} = (k_x, k_y, k_z)^\top$ is the wave vector. If we assume that $\eta_x = \eta_y = \eta_z = 1/\sqrt{3}$ and $\mathbf{k} = (k, 0, 0)^\top$ then we find

$$\frac{1}{c} \frac{\omega}{k} = \frac{\omega\Delta t}{2\eta_x \arcsin(\eta_x^{-1} \sin(\omega\Delta t/2))} \quad (4.5)$$

Thus in forward direction the simulated speed of light is lower than the physical one and it approaches it as $\omega \rightarrow 0$, see Fig. 4.2.

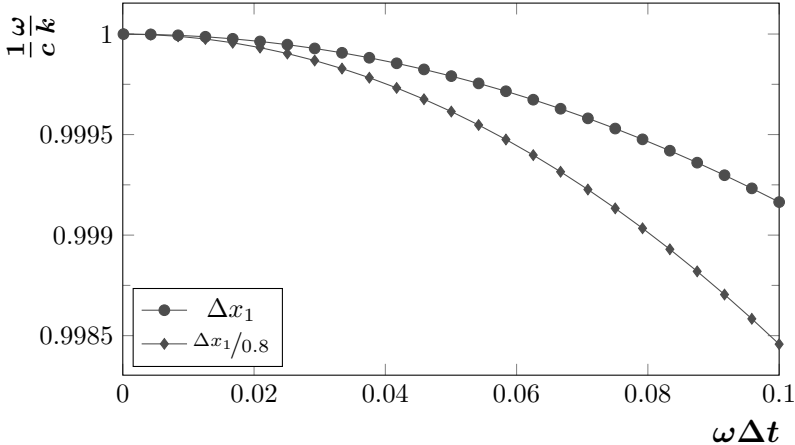


Figure 4.2: The numerical dispersion of the Yee scheme normalized to the speed of light for $\mathbf{k} = (k, 0, 0)^\top$ and for the two cases $c\Delta t/\Delta x_1 = \eta_x = 1/\sqrt{3}$ and $\Delta x = \Delta x_1/0.8$ while Δt remains constant.

The numerical phase velocity of a wave in FDTD does not only depend on the frequency of the wave but also on its direction. Inserting $\mathbf{k} = k(\sin(\Theta)\cos(\varphi), \sin(\Theta)\sin(\varphi), \cos(\Theta))^\top$ into (4.4) and applying a few transformations yields

$$\frac{1}{c} \frac{\omega}{k} = \frac{2}{\eta_x k \Delta x} \arcsin \left(\sqrt{\Sigma_x(\mathbf{k}, \varphi, \Theta) + \Sigma_y(\mathbf{k}, \varphi, \Theta) + \Sigma_z(\mathbf{k}, \varphi, \Theta)} \right). \quad (4.6)$$

The dispersion of the Yee scheme is plotted in Fig. 4.3 for the two distinct choices $\Theta = \pi/2$ and $\cos(\Theta) = 1/\sqrt{3}$. The first case describes waves propagating in the xy-plane of the mesh. The dispersion is minimized in the diagonal of the plane, $\varphi = \pi/4$. At the same angle the dispersion vanishes completely in the second case. This direction of propagation is parallel to the diagonal of the mesh cell.

Numerical dispersion occurs in all simulation schemes for Maxwell's equation in a more or less pronounced way. The dispersion of these schemes combined with PIC codes causes spurious Cerenkov radiation. True Cerenkov radiation occurs when relativistic particles propagate through a medium for which the phase velocity is lower than the speed of the particles. Typically this effect can be observed in nuclear power plants where the rods of radioactive material are submerged into water. The interaction of high energetic electrons resulting from an α decay with the surrounding water molecules is visible as blue light. Due to numerical dispersion a similar effect can be observed in simulation. Spurious high frequency fields are generated and degrade the results of simulations. One approach to reduce this effect is to eliminate these high frequencies through filters [81, 82].

The fact of vanishing dispersion in the Yee scheme in the direction parallel to the diagonal of the mesh cell can be exploited in simulations of systems with a distinguished direction such as linear particle accelerators [83]. The unit vectors of the cartesian coordinate system

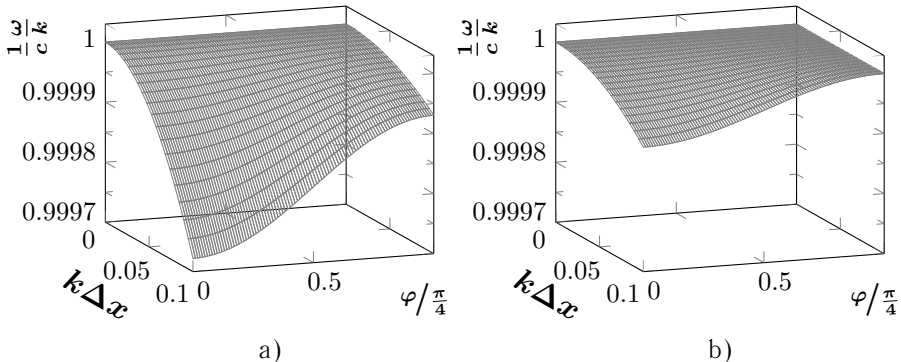


Figure 4.3: The numerical dispersion of the Yee scheme normalized to the speed of light for $\eta_x = \eta_y = \eta_z = 1/\sqrt{3}$, $\mathbf{k} = k(\sin(\Theta)\cos(\varphi), \sin(\Theta)\sin(\varphi), \cos(\Theta))^\top$ in dependence of the wave length and φ for a) $\Theta = \pi/2$ and b) $\Theta = \arccos(1/\sqrt{3})$.

of the domain are then no longer parallel to the edges of the mesh cells. This introduces an increased complexity caused by transformations from the coordinate system of the domain to the coordinate system of the mesh. In particular the discretization of the boundaries becomes more cumbersome.

Many more techniques to lower the dispersion have been investigated e.g. [84, 85].

4.2 Alternating-Direction Implicit Schemes

The Alternating-Direction Implicit (ADI) scheme for Maxwell's equations was introduced by Namiki [86] in two dimensions in order to overcome the CFL condition of the Yee scheme. The same formulation is also applicable in three dimensions [87]. The staggered grid was kept from the Yee scheme. But instead of a purely explicit finite-difference stencil a more complicated implicit update was chosen which is closely related to the Alternating-Direction Implicit method for parabolic and elliptic partial differential equations [88].

The update step is divided into two substeps and all the electric and magnetic components are twice updated simultaneously. In both substeps one part of the update for each component of the electric field is formulated implicitly. For the x-component of the electric field this yields

$$\mathbf{E}_x^{n+1/2} = \mathbf{E}_x^n + \frac{Z_0}{2} \mathcal{D}_z^\top \mathbf{H}_y^n - \frac{Z_0}{2} \mathcal{D}_y^\top \mathbf{H}_z^{n+1/2}, \quad (4.7)$$

The update for the other two electric components as well as the magnetic components follow likewise. The parts to be updated implicitly are chosen in such a way that for each substep every component of the electric field is implicitly coupled to only one component of the magnetic field and vice versa:

$$\mathbf{H}_z^{n+1/2} = \mathbf{H}_z^n + \frac{1}{2Z_0} \mathcal{D}_y \mathbf{E}_x^{n+1/2} - \frac{1}{2Z_0} \mathcal{D}_x \mathbf{E}_y^n. \quad (4.8)$$

This coupling is then alternated between the substeps:

$$\mathbf{E}_x^{n+1} = \mathbf{E}_x^{n+1/2} + \frac{Z_0}{2} \mathcal{D}_z^\top \mathbf{H}_y^{n+1} - \frac{Z_0}{2} \mathcal{D}_y^\top \mathbf{H}_z^{n+1/2}, \quad (4.9)$$

$$\mathbf{H}_y^{n+1} = \mathbf{H}_y^{n+1/2} + \frac{1}{2Z_0} \mathcal{D}_x \mathbf{E}_z^{n+1/2} - \frac{1}{2Z_0} \mathcal{D}_z \mathbf{E}_x^{n+1}. \quad (4.10)$$

By inserting (4.8) into the right hand side of (4.7) and (4.10) into the right hand side of (4.9) we get tridiagonal matrices on the left hand side. For the case of trivial boundaries where every mesh cell is either inside or outside the domain (staircase approximation) this matrix is symmetric, positive semi-definite and diagonal dominant. For (4.7) and (4.8) this matrix is $(\mathbb{1} + \frac{1}{4} \mathcal{D}_y^\top \mathcal{D}_y)$ and has the term $(1 + \frac{1}{2} \eta_y^2)$ on its diagonal and $-\frac{1}{4} \eta_y^2$ on the off-diagonals. Every component of the electric field is coupled implicitly to its neighboring siblings in one dimension only, e.g. $\tilde{\mathbf{E}}_{x; i+1/2, j, k}$ is coupled to $\tilde{\mathbf{E}}_{x; i+1/2, j, k'}$, where $k' \in \{0, N_z - 1\}$, in the first substep and to $\tilde{\mathbf{E}}_{x; i+1/2, j', k}$, where $j' \in \{0, N_y - 1\}$, in the second substep. Thus for the x-component there are $N_x N_y$ square matrices of size N_z in the first substep, and $N_x N_z$ square matrices of size N_y in the second substep. With a cyclic permutation of the indices the corresponding numbers for the y- and z-component can be found. Each of these systems can be solved independently using a Cholesky decomposition on a single core if the whole problem fits into memory. Thus for every tridiagonal matrix $\mathcal{T}_x^{(i,j)}$ one gets an upper triangular matrix $\mathcal{U}_x^{(i,j)}$ with $\mathcal{U}_x^{(i,j) \top} \mathcal{U}_x^{(i,j)} = \mathcal{T}_x^{(i,j)}$ and one off diagonal only. These decompositions are performed once at the beginning of the simulation and then stored instead of the matrices for the rest of the simulation. Thus the solution of the implicit scheme,

$$\mathcal{T}_x^{(i,j)} \mathbf{x} = \mathbf{r},$$

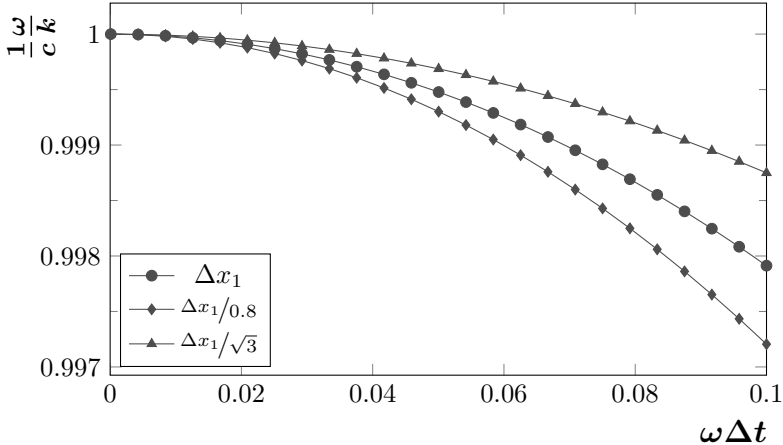


Figure 4.4: The numerical dispersion of the ADI scheme normalized to the speed of light for $\mathbf{k} = (k, 0, 0)^T$ and for the three cases $c\Delta t/\Delta x_1 = \eta_x = 1/\sqrt{3}$, $\Delta x = \Delta x_1/0.8$ and $\Delta x = 0.8 \Delta x_1$ while Δt remains constant.

reduces to

$$\begin{aligned}\mathcal{U}_x^{(i,j)} \mathbf{r} &= \mathbf{r}, \\ \mathcal{U}_x^{(i,j)} \mathbf{x} &= \mathbf{y}.\end{aligned}$$

In the latter form \mathbf{x} is found with little effort. \mathbf{y} is calculated by forward substitution

$$\mathbf{y}_k = \left(\mathcal{U}_{x; k, k}^{(i,j)} \right)^{-1} \left(\mathbf{r}_k - \mathcal{U}_{x; k-1, k}^{(i,j)} \mathbf{y}_{k-1} \right),$$

whereas \mathbf{x} is calculated from \mathbf{y} by backward substitution

$$\mathbf{x}_k = \left(\mathcal{U}_{x; k, k}^{(i,j)} \right)^{-1} \left(\mathbf{y}_k - \mathcal{U}_{x; k, k+1}^{(i,j)} \mathbf{x}_{k+1} \right).$$

For more complicated boundary conditions these tridiagonal matrices become non-symmetric, though the matrices remain diagonally dominant. In a simulation on a single core the Cholesky decomposition is replaced by the LU decomposition, while everything else remains unchanged.

In parallel these systems of equations can be solved by efficient methods such as [89, 90], derivations thereof [91], or newer developments for larger systems [92]. The consecutive solution of these systems of equations yields a non-optimal communication scheme due to the large number of small messages to be passed. Instead, the messages to be passed can be vectorized into larger chunks to better balance the ratio between transmission time and start-up time [93].

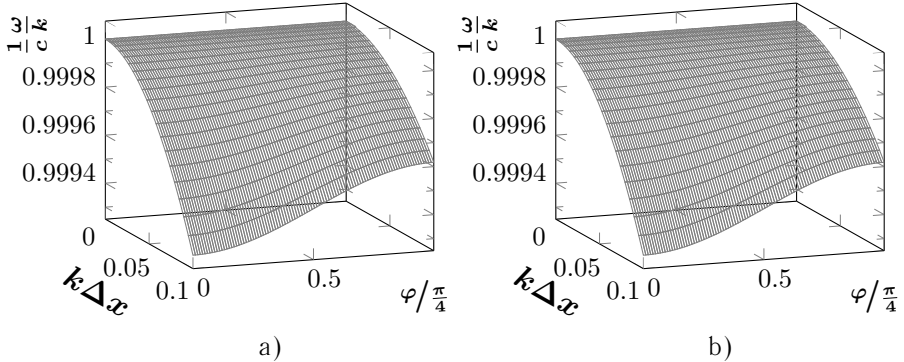


Figure 4.5: The numerical dispersion of the ADI scheme normalized to the speed of light for $\eta_x = \eta_y = \eta_z = 1/\sqrt{3}$, $\mathbf{k} = k (\sin(\Theta) \cos(\varphi), \sin(\Theta) \sin(\varphi), \cos(\Theta))^T$ in dependence of the wave length and φ for a) $\Theta = \pi/2$ and b) $\Theta = \arccos(1/\sqrt{3})$.

The ADI scheme is a compelling choice for the efficient solution of Maxwell's equations in parallel but for the numerical dispersion. Unfortunately in this respect this scheme is inferior to Yee's scheme. It is given by [94]

$$\sin(\omega \Delta t) = \frac{2\sqrt{(1 + \Sigma_x \Sigma_y \Sigma_z)(\Sigma_x + \Sigma_y + \Sigma_z + \Sigma_x \Sigma_y + \Sigma_y \Sigma_z + \Sigma_z \Sigma_x)}}{(1 + \Sigma_x)(1 + \Sigma_y)(1 + \Sigma_z)}, \quad (4.11)$$

where in vacuum $\Sigma_\nu = (\eta_\nu \sin(\frac{k_\nu \Delta \nu}{2}))^2$. For $\mathbf{k} = (k, 0, 0)^T$ we find

$$\frac{1}{c} \frac{\omega}{k} = \frac{\omega \Delta t}{2\eta_x \arcsin\left(\eta_x^{-1} \frac{1 - \cos(\omega \Delta t)}{\sin(\omega \Delta t)}\right)}.$$

Compared to the dispersion of the Yee scheme the dispersion of the ADI scheme is clearly stronger for the same size of time step and it gets worse with larger time steps, see Fig. 4.4.

Furthermore there is no propagation direction in which the dispersion vanishes such as for the Yee scheme, see Fig. 4.5. The dispersion is minimized in the direction parallel to the diagonal of the mesh cell but is far from vanishing. The situation can be alleviated by the introduction of artificial anisotropy [95] or higher order stencils [96]. Though poor dispersion properties are not the only weaknesses of the ADI scheme. It was observed that it exhibits also asymmetric effects [97] and fast growing truncation errors [98] that are absent in the Yee scheme.

4.2.1 Divergence Preserving Scheme

The standard ADI scheme is not only not suited for the combination with fast particles due to the dispersion but also because it does not preserve the divergence of the electromagnetic field. Thus the discrete representation of the divergence operator in the ADI scheme does

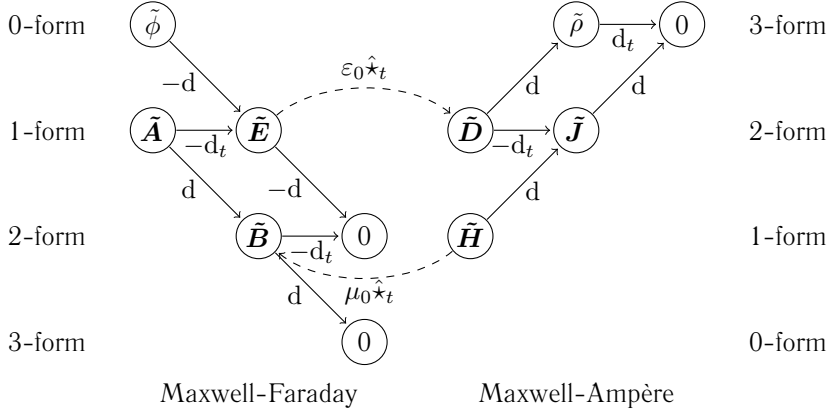


Figure 4.6: Maxwell's equations and their relations formulated with differential forms [100]. The Maxwell-Faraday part is discretized on the primal grid whereas the Maxwell-Ampère part on the dual grid. For regular meshes and vacuum the Hodge star operator, $\hat{\star}_t$ becomes 1.

not fulfill the conditions $\nabla_{\text{FD}} \cdot \tilde{\mathbf{E}} = \tilde{\rho}/\epsilon_0$ and $\nabla_{\text{FD}} \cdot \tilde{\mathbf{H}} = 0$ such as required in (1.4) [99]. It is shown in [99] how a divergence preserving ADI scheme can be obtained which is second order accurate with respect to the size of the time step as the original ADI scheme. The authors introduced the four operators $(\mathbb{1} + \frac{1}{2}\mathcal{P})$, $(\mathbb{1} - \frac{1}{2}\mathcal{P})$, $(\mathbb{1} + \frac{1}{2}\mathcal{M})$ and $(\mathbb{1} - \frac{1}{2}\mathcal{M})$, where

$$\mathcal{P} = \begin{pmatrix} 0 & 0 & 0 & 0 & 0 & -\mathcal{D}_y^\top \\ 0 & 0 & 0 & -\mathcal{D}_z^\top & 0 & 0 \\ 0 & 0 & 0 & 0 & -\mathcal{D}_x^\top & 0 \\ 0 & \mathcal{D}_z & 0 & 0 & 0 & 0 \\ 0 & 0 & \mathcal{D}_x & 0 & 0 & 0 \\ \mathcal{D}_y & 0 & 0 & 0 & 0 & 0 \end{pmatrix}, \quad \mathcal{M} = \begin{pmatrix} 0 & 0 & 0 & 0 & \mathcal{D}_z^\top & 0 \\ 0 & 0 & 0 & 0 & 0 & \mathcal{D}_x^\top \\ 0 & 0 & 0 & \mathcal{D}_y^\top & 0 & 0 \\ 0 & 0 & -\mathcal{D}_y & 0 & 0 & 0 \\ -\mathcal{D}_z & 0 & 0 & 0 & 0 & 0 \\ 0 & -\mathcal{D}_x & 0 & 0 & 0 & 0 \end{pmatrix}.$$

In this notation the discrete curl operator is given by $\nabla_{\text{FD}} \times \cong (c\Delta t)^{-1} (\mathcal{P} + \mathcal{M})$ and the discrete divergence operator by

$$\nabla_{\text{FD}} \cdot \cong (c\Delta t)^{-1} \begin{pmatrix} -\mathcal{D}_x^\top & -\mathcal{D}_y^\top & -\mathcal{D}_z^\top & 0 & 0 & 0 \\ 0 & 0 & 0 & \mathcal{D}_x & \mathcal{D}_y & \mathcal{D}_z \end{pmatrix}.$$

It is then easy to check that $\nabla_{\text{FD}} \cdot \nabla_{\text{FD}} \times \equiv 0$.

Note that the components of $\nabla_{\text{FD}} \cdot \tilde{\mathbf{E}}$ are face centered on the primal grid while those of $\nabla_{\text{FD}} \times \tilde{\mathbf{H}}$ are face centered on the dual grid. On an rectilinear grid the positions of the centers of the faces coincide with the center of the edges of its dual grid and vice versa. The location of field sampling points becomes clear when looking from the perspective of differential forms, see Fig. 4.6.

The original ADI scheme expressed with the operators $(\mathbb{1} \pm \frac{1}{2}\mathcal{P})$ and $(\mathbb{1} \pm \frac{1}{2}\mathcal{M})$ reads

$$\begin{aligned} \left(\mathbb{1} - \frac{1}{2}\mathcal{P}\right)\mathbf{u}^{n+1/2} &= \left(\mathbb{1} + \frac{1}{2}\mathcal{M}\right)\mathbf{u}^n \\ \left(\mathbb{1} - \frac{1}{2}\mathcal{M}\right)\mathbf{u}^{n+1} &= \left(\mathbb{1} + \frac{1}{2}\mathcal{P}\right)\left(\mathbf{u}^{n+1/2} + c\Delta t\mathbf{j}^{n+1/2}\right), \end{aligned}$$

where

$$\mathbf{u}^n = \begin{pmatrix} \mathbf{E}_x^n \\ \mathbf{E}_y^n \\ \mathbf{E}_z^n \\ Z_0 \mathbf{H}_x^n \\ Z_0 \mathbf{H}_y^n \\ Z_0 \mathbf{H}_z^n \end{pmatrix} \quad \text{and} \quad \mathbf{j}^n = - \begin{pmatrix} Z_0 \mathbf{J}_x^n \\ Z_0 \mathbf{J}_y^n \\ Z_0 \mathbf{J}_z^n \\ 0 \\ 0 \\ 0 \end{pmatrix}.$$

Out of $4!$ possible combinations including all four operators exactly once only eight schemes are second order in Δt : those four schemes which, for $a, b \in \{-1, 1\}$, are of the form $(\mathbb{1} + \frac{1}{2}a\mathcal{M})^a \cdot (\mathbb{1} + \frac{1}{2}b\mathcal{P})^b \cdot (\mathbb{1} - \frac{1}{2}b\mathcal{P})^{-b} \cdot (\mathbb{1} - \frac{1}{2}a\mathcal{M})^{-a}$ and those four one gets by interchanging \mathcal{P} and \mathcal{M} in the first four schemes. The second four are equivalent to the first four. Only one of the first four combinations and its equivalent preserve the divergence:

$$\begin{aligned} \left(\mathbb{1} - \frac{1}{2}\mathcal{M}\right)\mathbf{u}^{n+1/4} &= \mathbf{u}^n \\ \left(\mathbb{1} - \frac{1}{2}\mathcal{P}\right)\mathbf{u}^{n+3/4} &= \left(\mathbb{1} + \frac{1}{2}\mathcal{P}\right)\mathbf{u}^{n+1/4} + c\Delta t\mathbf{j}^{n+1/2} \\ \mathbf{u}^{n+1} &= \left(\mathbb{1} + \frac{1}{2}\mathcal{M}\right)\mathbf{u}^{n+3/4}. \end{aligned}$$

Using the identity,

$$\left(\mathbb{1} \pm \frac{1}{2}\mathcal{P}\right) \cdot \left(\mathbb{1} \mp \frac{1}{2}\mathcal{M}\right)^{-1} = \mathbb{1} \pm \frac{1}{2}(\mathcal{P} + \mathcal{M}) \cdot \left(\mathbb{1} \mp \frac{1}{2}\mathcal{M}\right)^{-1},$$

one finds

$$\boldsymbol{\nabla}_{\text{FD}} \cdot (\mathbf{u}^{n+1} - \mathbf{u}^n) = c\Delta t \boldsymbol{\nabla}_{\text{FD}} \cdot \mathbf{j}^{n+1/2} = \begin{pmatrix} (\tilde{\rho}^{n+1} - \tilde{\rho}^n)/\varepsilon_0 \\ 0 \end{pmatrix}.$$

The last equality does only hold if the numerical current preserves charge. As we will see, such methods for current deposition do indeed exist.

The dispersion relation is unfortunately the same as for the original ADI scheme, see (4.11) and Appendix A.1.

4.3 TE/TM Schemes

As we have seen, numerical schemes for Maxwell's equations that are coupled with the propagation of relativistic particles and which exhibit dispersion cause artificial Cerenkov radiation. To mitigate this effect one could apply low-pass filters to suppress the high frequency part of the electromagnetic field. Alternatively one could implement finite-difference time-domain methods devoid of dispersion. TE/TM schemes [55, 101] promise dispersion free propagation of electromagnetic waves along a single direction and moderate dispersion along the other directions.

The velocity of the particles in particle accelerators distinguish one direction in the 3-dimensional coordinate system. The electromagnetic field along this direction varies rapidly and high frequencies occur while transverse fields are of low frequency. Thus it is desirable to eliminate the numerical dispersion along the direction of propagation.

Instead of updating consecutively the electric and the magnetic field components as in the Yee scheme the TE/TM schemes update consecutively the transverse electric and the transverse magnetic field components. Thus the first step updates $\tilde{\mathbf{E}}_x$, $\tilde{\mathbf{H}}_y$ and $\tilde{\mathbf{H}}_z$ whereas the second step updates the remaining components. The transverse electric and the longitudinal magnetic field components of a cell that are updated simultaneously during the first step are located in a common plane, see Fig. 4.1. Also the remaining field components of a cell that are updated in the second step are located in a common plane. The stencil for the curl operator is the common finite-difference stencil which includes the co-planar field components. Thus the updates require future values of these components or approximations thereof. The first approach leads to the implicit scheme [101] whereas the second leads to the explicit scheme [55].

4.3.1 Implicit Scheme

For situations where the electric permittivity and the magnetic permeability reduce to the vacuum permittivity and permeability respectively the first implicit TE/TM scheme reads

$$\left(\mathbb{1} - \frac{1}{2} \mathcal{P}_1 \right) \mathbf{u}^{n+1/2} = \left(\mathbb{1} + \frac{1}{2} \mathcal{P}_1 \right) \mathbf{u}^{n-1/2} + \mathcal{M} \mathbf{v}^n - c\Delta t \mathbf{j}_u^n, \quad (4.12)$$

$$\left(\mathbb{1} - \frac{1}{2} \mathcal{P}_2 \right) \mathbf{v}^{n+1} = \left(\mathbb{1} + \frac{1}{2} \mathcal{P}_2 \right) \mathbf{v}^n - \mathcal{M}^\top \mathbf{u}^{n+1/2} - c\Delta t \mathbf{j}_v^{n+1/2}, \quad (4.13)$$

where

$$\begin{aligned} \mathbf{u}^n &= \begin{pmatrix} \mathbf{E}_x^n \\ Z_0 \mathbf{H}_y^n \\ Z_0 \mathbf{H}_z^n \end{pmatrix}, \quad \mathbf{v}^n = \begin{pmatrix} Z_0 \mathbf{H}_x^n \\ \mathbf{E}_y^n \\ \mathbf{E}_z^n \end{pmatrix}, \quad \mathbf{j}_u^n = \begin{pmatrix} Z_0 \mathbf{J}_x^n \\ 0 \\ 0 \end{pmatrix}, \quad \mathbf{j}_v^n = \begin{pmatrix} 0 \\ Z_0 \mathbf{J}_y^n \\ Z_0 \mathbf{J}_z^n \end{pmatrix}, \\ \mathcal{P}_1 &= \begin{pmatrix} 0 & \mathcal{D}_z^\top & -\mathcal{D}_y^\top \\ -\mathcal{D}_z & 0 & 0 \\ \mathcal{D}_y & 0 & 0 \end{pmatrix}, \quad \mathcal{P}_2 = \begin{pmatrix} 0 & \mathcal{D}_z & -\mathcal{D}_y \\ -\mathcal{D}_z^\top & 0 & 0 \\ \mathcal{D}_y^\top & 0 & 0 \end{pmatrix}, \quad \mathcal{M} = \begin{pmatrix} 0 & 0 & 0 \\ 0 & 0 & \mathcal{D}_x \\ 0 & -\mathcal{D}_x & 0 \end{pmatrix}. \end{aligned}$$

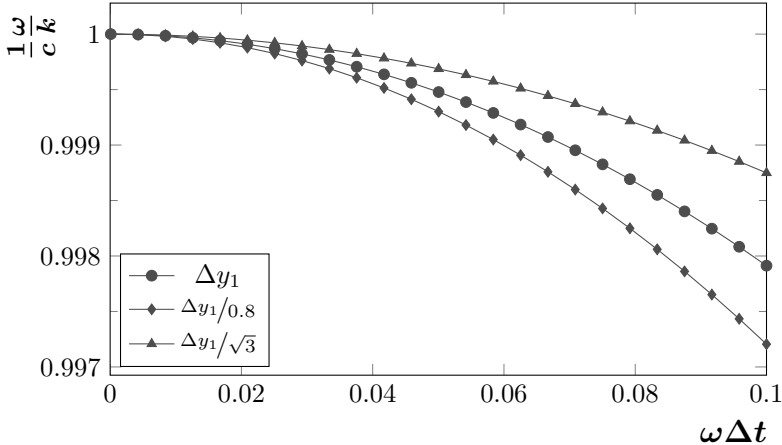


Figure 4.7: The numerical dispersion of the implicit TE/TM-ADI2 scheme normalized to the speed of light for $\eta_x = c\Delta t/\Delta x = 1$, $\mathbf{k} = (0, k, 0)^\top$ and for the three cases $c\Delta t/\Delta y_1 = 1/\sqrt{3}$, $\Delta y = \Delta y_1/0.8$ and $\Delta y = \Delta y_1/\sqrt{3}$ while Δt remains constant.

By inserting the second and third row into the first row of (4.12) and (4.13) respectively yields the matrices

$$\mathcal{W}^{E_x} = \left(\mathbb{1} + \frac{1}{4} \mathcal{D}_y^\top \mathcal{D}_y + \frac{1}{4} \mathcal{D}_z^\top \mathcal{D}_z \right), \quad (4.14)$$

$$\mathcal{W}^{H_x} = \left(\mathbb{1} + \frac{1}{4} \mathcal{D}_y \mathcal{D}_y^\top + \frac{1}{4} \mathcal{D}_z \mathcal{D}_z^\top \right) \quad (4.15)$$

on the left hand side for the solution of $\mathbf{E}_x^{n+1/2}$ and \mathbf{H}_x^{n+1} respectively. These matrices are symmetric and diagonally dominant though their inversion in parallel is far more demanding than the inversion of the corresponding matrices of the ADI scheme. They couple the values in two dimensions instead of a single dimension. Therefore the approximation

$$\mathcal{W}_{\text{ADI2}}^{E_x} = \left(\mathbb{1} + \frac{1}{8} \mathcal{D}_z^\top \mathcal{D}_z \right) \left(\mathbb{1} + \frac{1}{4} \mathcal{D}_y^\top \mathcal{D}_y \right) \left(\mathbb{1} + \frac{1}{8} \mathcal{D}_z^\top \mathcal{D}_z \right), \quad (4.16)$$

$$\mathcal{W}_{\text{ADI2}}^{H_x} = \left(\mathbb{1} + \frac{1}{8} \mathcal{D}_z \mathcal{D}_z^\top \right) \left(\mathbb{1} + \frac{1}{4} \mathcal{D}_y \mathcal{D}_y^\top \right) \left(\mathbb{1} + \frac{1}{8} \mathcal{D}_z \mathcal{D}_z^\top \right) \quad (4.17)$$

was proposed [101]. The error of this approximation is $O(\Delta t^4)$ but instead of a 2-dimensional problem only 1-dimensional problems have to be solved.

So far the material matrices that contain the electric permittivity and the magnetic permeability are assumed to be diagonal and reducing to their values in vacuum. In the notation above they are hidden in the matrices \mathcal{D}_ν . For boundary conditions different from the staircase approximation the material matrices may become non-diagonal. To retain the tridiagonal matrices in (4.16) and (4.17) only the diagonal part of the material matrices

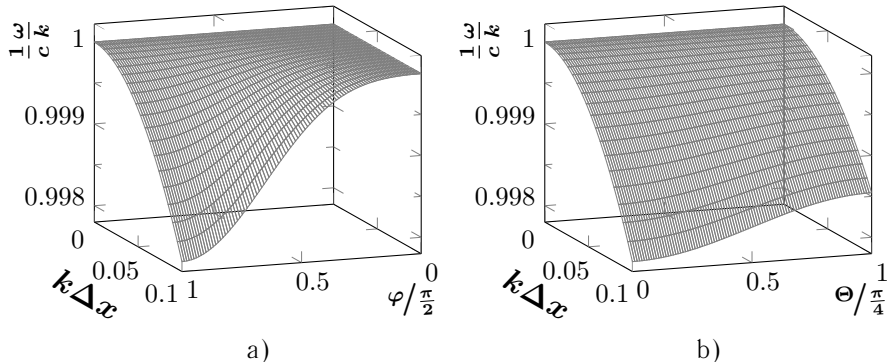


Figure 4.8: The numerical dispersion of the implicit TE/TM-ADI2 scheme normalized to the speed of light for $\mathbf{k} = k(\sin(\Theta)\cos(\varphi), \sin(\Theta)\sin(\varphi), \cos(\Theta))^\top$ and $\eta_x = 1, \eta_y = \eta_z = 1/\sqrt{3}$ a) in dependence of the wave length and φ for $\Theta = \pi/2$ and b) in dependence of the wave length and Θ for $\varphi = \pi/2$.

is used to solve the systems. To correct for the error introduced by the omission of the non-diagonal part a few iteration steps are applied.

The TE/TM-ADI2 scheme is stable for

$$c \Delta t \leq \min(2\Delta x, 2\Delta y, \Delta z).$$

Two more approximations for (4.14) and (4.15) are proposed in [101] but the TE/TM-ADI2 scheme combined with a few iterations, if needed, seems to perform best.

The dispersion of the implicit TE/TM is given by [101]

$$\sin^2(\omega\Delta t/2) = \cos^2(\omega\Delta t/2)(\Sigma_y + \Sigma_z) + \Sigma_x,$$

where $\Sigma_\nu = (\eta_\nu \sin(\frac{k_\nu \Delta_\nu}{2}))^2$. Thus the dispersion vanishes in forward direction for $\eta_x = 1$. For $\mathbf{k} = (0, k, 0)^\top$ it becomes

$$\frac{1}{c} \frac{\omega}{k} = \frac{\omega \Delta t}{2\eta_y \arcsin(\eta_y^{-1} \tan(\omega \Delta t / 2))}.$$

It is comparable to the dispersion of the Yee scheme along the axis of the grid, compare Fig. 4.2 and Fig. 4.7.

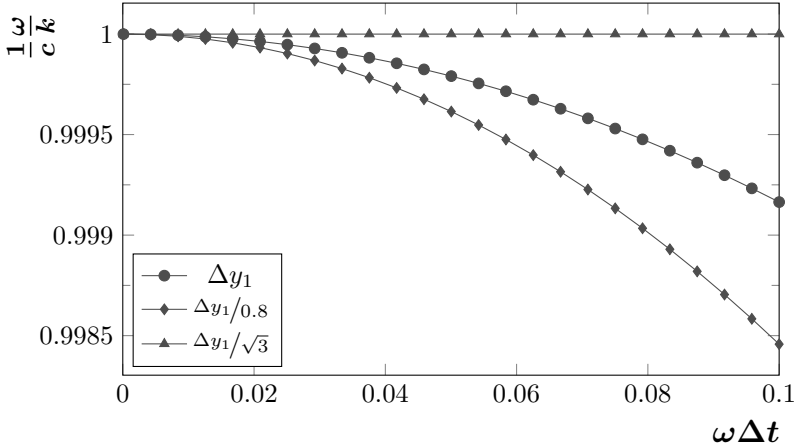


Figure 4.9: The numerical dispersion of the explicit TE/TM scheme normalized to the speed of light for $\eta_x = c\Delta t/\Delta x = 1$, $\mathbf{k} = (0, k, 0)^\top$ and for the three cases $c\Delta t/\Delta y_1 = 1/\sqrt{3}$, $\Delta y = \Delta y_1/0.8$ and $\Delta y = \Delta y_1/\sqrt{3}$ while Δt remains constant.

4.3.2 Explicit Scheme

$$\mathbf{u}^n = \left(\mathbb{1} + \frac{1}{2}\mathcal{P}_1 \right) \mathbf{u}^{n-1/2} + \frac{1}{2}\mathcal{M} \mathbf{v}^n, \quad (4.18)$$

$$\mathbf{u}^{n+1/2} = \left(\mathbb{1} + \frac{1}{2}\mathcal{P}_1 - \mathcal{P}_1^\top \right) \mathbf{u}^n + \frac{1}{2}\mathcal{M} \mathbf{v}^n - c\Delta t \mathbf{j}_u^n, \quad (4.19)$$

$$\mathbf{v}^{n+1/2} = \left(\mathbb{1} + \frac{1}{2}\mathcal{P}_2 \right) \mathbf{v}^n - \frac{1}{2}\mathcal{M}^\top \mathbf{u}^{n+1/2}, \quad (4.20)$$

$$\mathbf{v}^{n+1} = \left(\mathbb{1} + \frac{1}{2}\mathcal{P}_2 - \mathcal{P}_2^\top \right) \mathbf{v}^{n+1/2} - \frac{1}{2}\mathcal{M}^\top \mathbf{u}^{n+1/2} - c\Delta t \mathbf{j}_v^{n+1/2}, \quad (4.21)$$

where

$$\begin{aligned} \mathbf{u}^n &= \begin{pmatrix} \mathbf{E}_x^n \\ Z_0 \mathbf{H}_y^n \\ Z_0 \mathbf{H}_z^n \end{pmatrix}, \quad \mathbf{v}^n = \begin{pmatrix} Z_0 \mathbf{H}_x^n \\ \mathbf{E}_y^n \\ \mathbf{E}_z^n \end{pmatrix}, \quad \mathbf{j}_u^n = \begin{pmatrix} Z_0 \mathbf{J}_x^n \\ 0 \\ 0 \end{pmatrix}, \quad \mathbf{j}_v^n = \begin{pmatrix} 0 \\ Z_0 \mathbf{J}_y^n \\ Z_0 \mathbf{J}_z^n \end{pmatrix}, \\ \mathcal{P}_1 &= \begin{pmatrix} 0 & 0 & 0 \\ -\mathcal{D}_z & 0 & 0 \\ \mathcal{D}_y & 0 & 0 \end{pmatrix}, \quad \mathcal{P}_2 = \begin{pmatrix} 0 & 0 & 0 \\ -\mathcal{D}_z^\top & 0 & 0 \\ \mathcal{D}_y^\top & 0 & 0 \end{pmatrix}, \quad \mathcal{M} = \begin{pmatrix} 0 & 0 & 0 \\ 0 & 0 & \mathcal{D}_x \\ 0 & -\mathcal{D}_x & 0 \end{pmatrix}. \end{aligned}$$

The stability condition of the explicit TE/TM scheme demands that $\eta_x \leq 1$, while η_y and η_z do not influence the stability. Thus one can use larger grid sizes in transverse direction as with the implicit scheme.

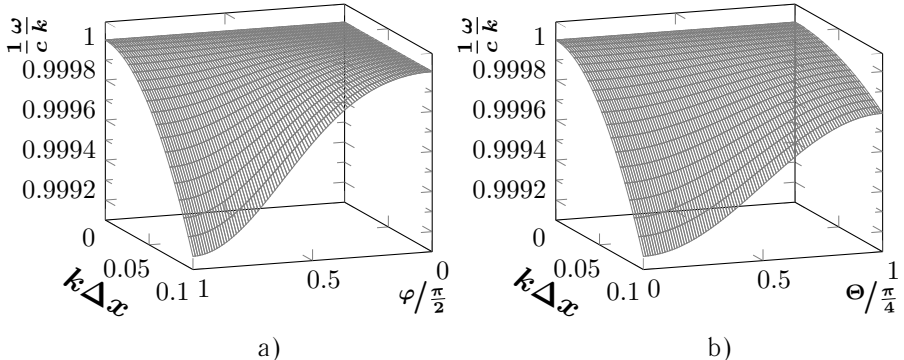


Figure 4.10: The numerical dispersion of the explicit TE/TM scheme normalized to the speed of light for $\mathbf{k} = k(\sin(\Theta)\cos(\varphi), \sin(\Theta)\sin(\varphi), \cos(\Theta))^\top$ and $\eta_x = 1$, $\eta_y = \eta_z = 1/\sqrt{3}$ a) in dependence of the wave length and φ for $\Theta = \pi/2$ and b) in dependence of the wave length and Θ for $\varphi = \pi/2$.

The dispersion of the scheme in forward direction vanishes for the upper limit of the stability region, $\eta_x = 1$:

$$\sin^2(\omega\Delta t/2) = (\Sigma_y + \Sigma_z)(1 - \Sigma_x) + \Sigma_x,$$

where $\Sigma_\nu = (\eta_\nu \sin(\frac{k_\nu \Delta \nu}{2}))^2$. The transverse dispersion also vanishes for $\mathbf{k} = (0, k, 0)^\top$ and $\eta_y = 1$ or $\mathbf{k} = (0, 0, k)^\top$ and $\eta_z = 1$. The transverse dispersion for $0 \leq \Theta \leq \pi/4$, $\varphi = \pi/2$ and $\eta_y = \eta_z = 1/5$ is plotted in Fig. 4.10 on the left hand side whereas for $\Theta = \pi/2$, $0 \leq \varphi \leq \pi/4$ it is plotted on the right hand side.

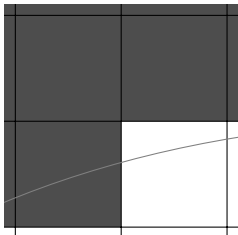
4.4 Boundary Conditions

4.4.1 Perfect Electric Conductor

As its name suggests, the Perfectly Electric Conducting (PEC) boundaries simulate materials with vanishing electric resistance. Thus any applied potential between two points on a surface is instantaneously compensated by surface charges. For any electric field with components tangential to the surface an electric field is induced which compensates the tangential components.

The PEC boundary condition is often a sufficiently accurate approximation for metallic surfaces.

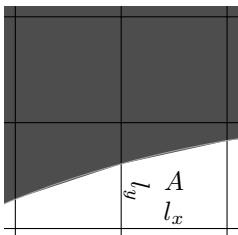
Staircase Approximation



The staircase approximation is the simplest implementation of a PEC boundary condition. Any cell of the primal grid is either inside or outside the domain. The electric components inside the material and on the surface as well as the magnetic components inside the material are initialized to zero and are not updated during the simulation.

Unfortunately the staircase approximation yields poor accuracy and introduces spurious modes [102, 103].

Dey-Mitra Boundary Condition



This cut-cell approximation is easy to implement [104] and is not afflicted with poor accuracy or spurious modes. The update of the electric components remains unaltered. Though in the calculation of the curl of the electric field only those parts of the edges and the area are considered which are inside the domain. (4.2) is changed to

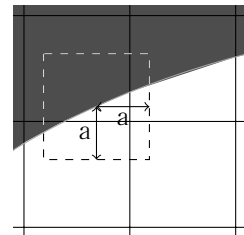
$$\mathcal{A} \mathbf{v}^{n+1} = \mathcal{A} \mathbf{v}^n - \mathcal{P}^\top \mathcal{L} \mathbf{u}^{n+1/2},$$

where \mathcal{A} and \mathcal{L} are the diagonal matrices containing the fractions of the areas and the fractions of lengths respectively of the cells of the primal mesh that are inside the domain.

The Dey-Mitra approach yields low errors and nice convergence rates of second order in edge lengths. But the time step size has to be reduced due to possibly reduced ratios between edge lengths and areas. In [104] two conditions are given: one for the area and one for the ratio between edge length and area. Then time steps between 50 % to 70 % are proposed. This reduction in time step size is unfavorable for update schemes which rely on fixed ratios between time step to mesh size in one direction for vanishing dispersion such as the implicit or the explicit TE/TM schemes.

Uniformly Stable Conformal Scheme

The Uniformly Stable Conformal (USC) scheme [105] for the treatment of boundary cells was invented to avoid the need to reduce the time step. For this a virtual cell is envisioned inside the primal grid which protrudes into those neighboring cells that are partially or fully inside the domain. The size of the virtual cell can be controlled within certain limits. Within these limits the cell is large enough to run the simulation without reduction of the time step. The electric voltages on the edges of this virtual cell are then calculated by an interpolation of the adjacent edges.



The exact weights for the interpolation are calculated at the beginning and are then kept for the rest of the simulation.

In the formulation of the Finite-Integration Technique (FIT) [106] the weights are incorporated into the material matrix. This matrix is the product of two matrices which in turn are calculated from the areas of the neighboring cells that are inside the domain and edge lengths to these neighboring cells. For a matrix free formulation such as the original Yee scheme the procedures for the calculation of the weights becomes complicated but is feasible.

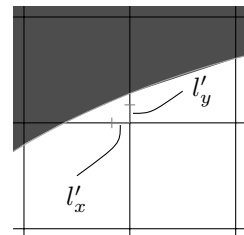
Simplified Conformal Scheme

In [107] it is analyzed why the Dey-Mittra cut-cell approximation fails if the time step is not reduced. The authors find that if for any face the ratio $\tilde{s}_{p;ijk}/\tilde{l}_{\bar{p};IJK} < 0.5$ between the normalized area

$$\tilde{s}_{p;ijk} = \frac{s_{p;ijk}}{S_{p;ijk}}$$

and one of its bounding normalized edges

$$\tilde{l}_{\bar{p};IJK} = \frac{l_{\bar{p};IJK}}{L_{\bar{p};IJK}}$$



then the cut-cell approximation becomes unstable. Here $S_{p;ijk}$ and $L_{\bar{p};ijk}$ denote area of face p and length of edge \bar{p} of cell ijk . The lower case equivalents denote the area and edge length of the cut-cells.

To ensure that the ratio remains greater or equal to the limit of $1/2$ two schemes are proposed: the first scheme increases the areas of the faces of the cut-cells. The authors call this the s-method. The second scheme lowers the lengths of the edges. The authors then show for the case of a circular domain that the second method has a second order convergence rate whereas the first method only has one of first order. The convergence rate of the second method is also comparable to the convergence rate of the Dey-Mittra cut-cell method but in contrary the time step does not have to be reduced. This new method shows also good results for other domains. For all examples the uniformly stable conformal scheme shows better convergence but the implementation of this new method is far simpler while still showing good results.

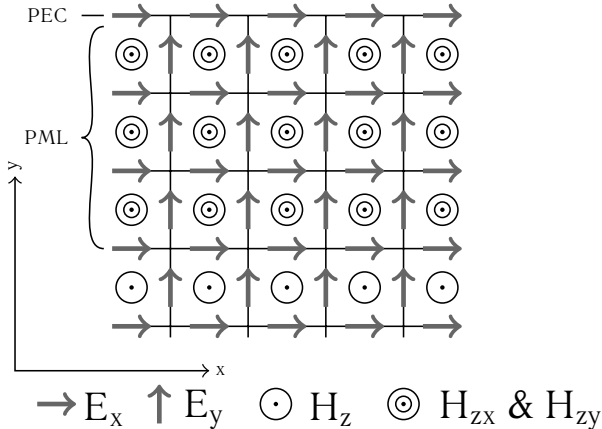


Figure 4.11: A domain terminated by perfectly matched layers.

4.4.2 Absorbing Boundary Conditions

Absorbing boundaries are introduced to reduce the domain size if only vacuum is beyond this boundary. Good absorbing boundaries have a low reflectivity for a broad frequency spectrum and a broad range of incidence angle. Without absorbing boundaries the size of the domain has to be chosen large enough such that during the simulation reflecting waves do not have an impact on the region of interest.

Perfectly Matched Layers

Perfectly Matched Layers [108] fulfill the requirements of absorbing a broad spectrum of waves from any angle. This is achieved by adding a band filled with perfectly matched media, see Fig. 4.11. Each component of the magnetic field is split into two sub-components inside a perfectly matched medium. Then terms for electric and magnetic conductivities are added. Maxwell's equations in 2D and for the transverse electric case then become

$$\begin{aligned} \frac{\partial \tilde{\mathbf{E}}_x}{\partial t} + \sigma_y \tilde{\mathbf{E}}_x &= -\frac{\partial (\tilde{\mathbf{H}}_{zx} + \tilde{\mathbf{H}}_{zy})}{\partial y}, \\ \frac{\partial \tilde{\mathbf{E}}_y}{\partial t} + \sigma_x \tilde{\mathbf{E}}_y &= -\frac{\partial (\tilde{\mathbf{H}}_{zx} + \tilde{\mathbf{H}}_{zy})}{\partial x}, \\ \frac{\partial \tilde{\mathbf{H}}_{zx}}{\partial t} + \sigma_x^* \tilde{\mathbf{H}}_{zx} &= -\frac{\partial \tilde{\mathbf{E}}_y}{\partial x}, \\ \frac{\partial \tilde{\mathbf{H}}_{zy}}{\partial t} + \sigma_y^* \tilde{\mathbf{H}}_{zy} &= \frac{\partial \tilde{\mathbf{E}}_x}{\partial y}. \end{aligned}$$

The procedure for 3-dimensional domains is similar, see [109]. The reflection of a wave that propagates in y-direction in Fig. 4.11 is controlled by σ_x and σ_x^* only. The conductivities have to fulfill the requirement

$$\frac{\sigma_x}{\varepsilon_0} = \frac{\sigma_x^*}{\mu_0} \quad \text{and} \quad \frac{\sigma_y}{\varepsilon_0} = \frac{\sigma_y^*}{\mu_0}$$

in order that the impedance of the medium is the same as that of vacuum. This guarantees in theory that no waves are reflected at the interface between vacuum and PML. Furthermore the conductivities should not change rapidly to keep numerical reflections low. In order to have a low reflectivity the band of PML is several layers thick and the conductivities increase towards the outer boundary. Thus the theoretical and numerical reflectivity is controlled by the total conductivity integrated over the width of the band of PM media and the differences in conductivities between the layers.

Perfectly matched layers can be adapted to the original [110, 111] and the divergence preserving [112] ADI scheme. However no literature could be found that showed results for the combination PML and TE/TM schemes but it seems straight forward to adapt the PML to these schemes too.

Chapter Five

Implementation

The FDTD code started as an adaptation of the simple application ToyFDTD [113] using the library *Independent Parallel Particle Layer* (IPPL) [54]. IPPL provides classes and methods for particles and for vector and scalar fields. Among others it provides methods to scatter and gather field values for node and cell centered fields. However corresponding methods for edge centered fields such as the electric field are missing and had to be implemented. From a user perspective it is very convenient that IPPL exchanges field values on guard cells and particles transparently among computing cores.

Furthermore the following libraries were used:

- Trilinos [114, 115] for the Poisson solver that is based on a multilevel preconditioned solver,
- Boost [116] for its C++ bindings to the Message Passing Interface (MPI),
- TCLAP [117] to parse the command line arguments,
- H5hut [118] to save all necessary information for restarts of simulations and analysis,
- GSL [119] for its pseudo and quasi random number generators and
- OpenSSL for md5 hashtags of MPI messages.

5.1 Parallelization

For a good load balancing in a Particle-in-Cell application it is necessary that both the load due to the particles as well as the load due to the fields are well balanced among the compute cores. In a particle accelerator particles are found in a small region of the machine only. This leads to an uneven distribution of the particles among the cores. A good balancing is non-trivial since the two problems are coupled at two locations in a simulation loop (see Fig. 1.8). On the one hand the electromagnetic field at the location of a particle is needed for the update of position and momentum of the particle. On the other hand the current that is induced by the particles is needed to update the electric field at the positions of the particles. For both steps it is advantageous if the particle and the surrounding electromagnetic field are updated on the same compute core. If this is not the case then this information has to be communicated between the cores that contain them.

IPPL provides two different parallelization schemes for the particles whereas the fields are by default evenly distributed among the compute cores using recursive binary subdivision. The *ParticleSpatialLayout* is easy to use since it distributes the particles according to their location within the mesh. Gathering the electromagnetic field from the mesh and scattering the current density to the mesh is then trivial. IPPL handles the exchange of particles when they leave the local part of the mesh.

In the worst case this leads to a partitioning where a single core has to handle all particles. All other cores would have to wait to exchange the guard cells for the electric field.

IPPL also provides the *ParticleUniformLayout* which distributes the particles equally among the cores irrespective of their locations. Indeed this guarantees that the load due to the particles is equal on all cores. But every core has to receive a copy of the electromagnetic field of the region that contains the particles in order to update the positions and momenta of the particles. Thereafter the cores have to send the current density that their particles induced to the cores that update the electromagnetic field in the region of the particles. The time needed for this exchange of electromagnetic field and current density increases rapidly with the number of cores.

Possibly one could also improve the parallel performance using the new non-blocking methods for collective communications introduced to the MPI standard. This could help to hide the latency due to the communication. But they were not used for this project because the first stable version of Open MPI that implements them has been released recently.

Additionally to an implementation using the *ParticleUniformLayout* a more complicated approach was implemented. An auxiliary mesh that is only a little bigger than the bounding box that contains the particles is introduced, see Fig. 5.1. This mesh uses the same cell size as the global mesh. For every cell of the auxiliary mesh there is a cell of the global mesh at the exact same position. The auxiliary mesh is moving with the particle bunch. Its position is changed after every time step such that all particles are contained within it at any time.

The auxiliary mesh is distributed evenly among the cores. For the partitioning of the particles the *ParticleSpatialLayout* based on the partitioning of the auxiliary mesh is used. In this application the size of the bounding box that contains the particles changes only marginally since the energy of the particles is large compared to the rest mass of the particles. For the same reason the relative movements of the particles within the bunch are small. This allows one to disregard a reassignment of the particles to the cores.

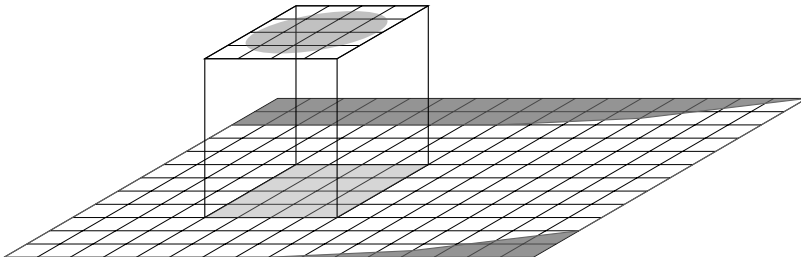


Figure 5.1: Sketch of the auxiliary mesh that propagates through the domain synchronously to the particle bunch.

The electromagnetic field on the auxiliary mesh is initialized by copying the electromagnetic field of the global mesh after the successful initialization of the electromagnetic field on the global mesh. Thereafter the electromagnetic field on the auxiliary mesh is updated including the current density that is induced by the particles. On the global mesh however the current density is neglected when updating the electromagnetic field. On the one hand this leads to an electromagnetic field on the global mesh that is not correct in the region where the auxiliary mesh and the global mesh overlap. On the other hand also on the auxiliary mesh information is missing to maintain a correct solution of the electromagnetic field. Therefore after every update of the electromagnetic field the data at the boundary of the auxiliary mesh has to be copied to the global mesh. Conversely corresponding data from the global mesh has to be copied to the auxiliary mesh.

On the one hand the particles are more evenly distributed when using this auxiliary mesh compared to when the ParticleSpatialLayout is used directly on the global mesh. On the other hand the amount of data that has to be communicated is reduced when using the auxiliary mesh compared when using the ParticleUniformLayout on the global mesh.

Algorithm 1 Assigns each core in the pool of secondary cores to a primary core while trying to reduce the maximal load caused by the particles.

```

1: struct PrimaryListItem{int id, int sIds[], float quorum}
2: struct SecondaryPoolItem{int id, int nParts}
3: function BUILDPRIMARYLIST(PrimaryList, SecondaryPool)
4:   Sort(SecondaryPool, SecondaryPool[].nParts, desc)
5:   while Size(SecondaryPool) > 0 do
6:     Sort(PrimaryList, PrimaryList[].quorum, desc)
7:     pItem  $\leftarrow$  First(PrimaryList)
8:     sItem  $\leftarrow$  Last(SecondaryPool)
9:     AssignSecondaryCore(pItem, sItem)
10:    PopBack(SecondaryPool)
11:   end while
12:   return PrimaryCoreList
13: end function
```

Disadvantages of the approach with this auxiliary mesh are an increased complexity in particular the exchange of boundary values, an increased memory usage and unfavorable ratios between local fields and guard cells on the auxiliary mesh for increasing numbers of cores. Furthermore the load due to the particles is still not distributed very evenly. For a Gaussian particle distribution e.g. the cores that update the fields at the center of the auxiliary mesh have a considerably bigger load due to the particles than cores that update the fields at the boundary of the auxiliary mesh. To overcome the latter a primary-secondary scheme was introduced.

At the beginning of the simulation two lists are created. The lists contain the ranks of the cores and the number of particles that are located in their partition of the auxiliary mesh. All cores that have more local particles than the average are potential primary cores, all cores with less local particles are secondary cores. The primary core list contains all potential primary cores and a list of secondary cores which are assigned to them and which is empty at the beginning. The secondary core pool contains all secondary cores. The secondary cores are then assigned to the primary cores. A simple algorithm is used to optimize the distribution of particles, see Algorithms 1 and 2.

The secondary core pool is first sorted such that the core with the least particles comes first. The primary core list is sorted such that the core with the most particles is in the first entry. Then the first core of the pool of secondary cores is assigned to the first primary core of the list and removed from the pool. Then the primary core list is sorted such that the primary-secondary group with the most particles per core is in the first entry. This process is then repeated until there are no secondary cores left in the pool.

Algorithm 2 Adds a core to the list of cores a primary core controls and updates the average number of particles each core of this primary-secondary group has to handle.

```

1: function ASSIGNSECONDARYCORE(pItem, sItem)
2:   s  $\leftarrow$  Size(Item.sIds)
3:   q  $\leftarrow$  pItem.quorum
4:   Insert(pItem.sIds[], sItem.id)
5:   q  $\leftarrow$  q * s
6:   q  $\leftarrow$  q + sItem.nParts
7:   s  $\leftarrow$  Size(pItem.sIds)
8:   pItem.quorum  $\leftarrow$  q/s
9: end function
```

After updating the electromagnetic field on the auxiliary mesh a primary core sends its local fields to all its secondary cores. Each primary-secondary group has its own MPI communicator such that efficient methods for collective communication can be used. The secondary cores then update the positions and momenta of the particles, compute the current density and send back the current density. The amount of data that has to be sent around is much smaller compared to a direct application of the *ParticleUniformLayout*. Furthermore the load of collecting and sending data is distributed among more cores. But also for this scheme an improvement from non-blocking collectives could be expected.

This primary-secondary scheme is very similar to [120] and [121]. It is relatively simple to implement but it cannot guarantee that in the number of particles per core is the same in

every primary-secondary group. This is easily seen in a simple example: if we assume that there 4 cores with 2, 5, 8 and 9 particles respectively. Then we get two primary-secondary groups with the above algorithms with 13 and 11 particles respectively. This is not optimal but there is no combination which yields 12 particles per group. The authors of [121] therefore propose to treat all cores as potential secondary cores. Some cores can then be primary cores of one primary-secondary group and at the same time secondary core of another group. This allows one to the balance number of particles optimally among all cores at the cost of an increased amount of data that has to be communicated.

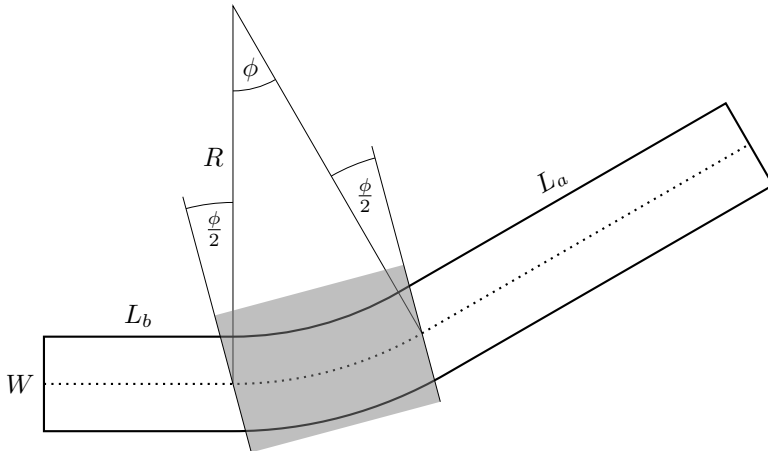


Figure 5.2: Sketch of a bend with the necessary parameters marked. These are the lengths of the drifts before and after the bend, L_b and L_a respectively, the width W , the bend angle ϕ and the bend radius R . The gray shaded rectangle indicates the dipole magnet.

5.2 Geometry and Boundary Conditions

To run simulations with complicated geometries using finite-differences one often has to read in CAD files and then identify the points of intersection with the rectangular mesh. For this thesis this was not necessary. A few parameters are sufficient to fully describe a simple bend in two dimensions. A rectangular bend with hard edges was chosen due to the simplicity to implement. Before and after the bend the particles should drift for some distance. Such a geometry is determined by the following parameters (see Fig. 5.2):

- L_b the length of drift before the dipole magnet,
- L_a the length of drift after the dipole magnet,
- W the distance between the two boundaries,
- ϕ the angle of deflection,
- B_z the strength of the uniform magnetic field,
- E_{kin} the kinetic energy of the particles.

The radius R of the bend is determined by the kinetic energy, the magnetic field and the rest mass, m , and charge, q , of the particles. The key for the derivation is the Lorentz force,

$$\mathbf{F} = m\gamma \frac{d^2\mathbf{r}}{dt^2} = q \frac{d\mathbf{r}}{dt} \times \tilde{\mathbf{B}}.$$

For the simple magnetic field, $\tilde{\mathbf{B}}(\mathbf{r}) = (0, 0, B_z)^\top$ for \mathbf{r} inside the bend and $\tilde{\mathbf{B}}(\mathbf{r}) = 0$ outside, such as it is assumed in this thesis, one can derive the radius of the bend. For this

we assume the following path, velocity and acceleration of a particle,

$$\mathbf{r} = R \begin{pmatrix} \sin\left(\frac{\beta c}{R}t\right) \\ (1 - \cos\left(\frac{\beta c}{R}t\right)) \\ 0 \end{pmatrix}, \quad \frac{d\mathbf{r}}{dt} = \beta c \begin{pmatrix} \cos\left(\frac{\beta c}{R}t\right) \\ \sin\left(\frac{\beta c}{R}t\right) \\ 0 \end{pmatrix}, \quad \frac{d^2\mathbf{r}}{dt^2} = \frac{\beta^2 c^2}{R} \begin{pmatrix} -\sin\left(\frac{\beta c}{R}t\right) \\ \cos\left(\frac{\beta c}{R}t\right) \\ 0 \end{pmatrix},$$

where we assume that $qB_z < 0$. The path describes a perfect circle with radius R . Inserting velocity and acceleration into the Lorentz force yields then

$$R = -\frac{mc^2\beta\gamma}{c qB_z} = -\frac{\sqrt{E_{\text{kin}}^2 + 2E_{\text{kin}}mc^2}}{c qB_z}$$

The first step that the geometry class has to perform is to determine for all mesh nodes whether they are inside or outside the domain or on the boundary. A cell is inside the domain if all of its nodes are inside, it is outside if all of its nodes are outside and it is on the boundary if some of its nodes are inside while others are outside. Using this information the geometry class provides a list of all boundary cells and a mask that can be used to efficiently update the field inside the domain. With IPPL one then can use this mask to update only those field values that lie fully inside. The boundary cells have then to be treated separately.

The geometry also determines for every boundary cell the fraction of length of their edges and the fraction of their areas that are inside the domain. This information is needed by the cut-cell boundary conditions. The s-method as described in [107] and in Section 4.4.1 is implemented for the treatment of boundary cells. It loops over all local boundary cells and updates the electromagnetic field in each cell.

Finally the geometry class also provides a method which takes a position and returns the external magnetic field at this position. For this it checks whether the position is inside the gray shaded rectangle in Fig. 5.2. If this is the case then the geometry class returns the magnetic field that the user provided as parameter. If the position is outside the rectangle then the geometry class returns an external magnetic field of 0 T.

5.3 Poisson Solver

The computation of the initial conditions of the electromagnetic field is a delicate step in a simulation. If the solution for the initial field does not fit to the updating steps of Maxwell's equations then two artifacts can be observed. First a halo field remains stationary at the location where particles were initially. And second the correct field develops eventually but for large particle energies this is a very slow process. The transverse electric field for highly relativistic charged particles is orders of magnitude stronger than the longitudinal electric field due to relativistic length contraction. Thus a small error in the initial solution is immediately visible in the longitudinal electric field.

An initial solution at $t = 0$ has not to be calculated once but twice. Once for the longitudinal electric field which is edge centered in the primal grid and once for the transverse magnetic field which is face centered in the primal grid or edge centered in the dual grid depending on whether one calculates $\tilde{\mathbf{B}}$ or $\tilde{\mathbf{H}}$. This then has to be repeated for $t = \Delta t/2$ for the transverse electric and the longitudinal magnetic field. Thus for a three dimensional simulation one would have to solve a Poisson problem four times. In two dimensions no longitudinal component of the magnetic field has to be updated in the second substep. Thus one has to solve the problem three times.

The longitudinal dimension has to be stretched by the factor $\gamma = E_{\text{kin}}/m + 1$ for the transformation from a system at rest to the co-moving frame in which the particles are at rest. Here E_{kin} is the kinetic energy of the particles and m is their rest mass. For highly relativistic particles this leads to a large aspect ratio of the cells which causes a Poisson solver that is based on a conjugate-gradient method to converge slowly and many iteration steps are needed. Fortunately one has good initial solutions for the Poisson solver after it has converged once.

Furthermore the stretch in longitudinal direction gives rise to a quick decay of the fields. This is important since the boundary Γ_1 , see Fig. 2.2, is treated as a PEC boundary instead of as an open boundary. This quick decay however allows one to place the particle bunch close to the boundary and to keep small the length of the drift L_b in front of the bend, see Fig. 5.2. Furthermore one can neglect the geometry beyond the entry edge of the bend provided the distance is large enough. Thus one can reduce the geometry for the Poisson solver to a simple straight section.

5.4 Particle Bunch

Quasi-static PIC codes and self-consistent PIC codes can share most of the common routines except for the space charge solver. The particle class for this thesis originates from OPAL [44]. It had to be adapted for the problem at hand. Most of the code was stripped.

So far only a Gauss distribution is implemented. The space part of this distribution is fully described by the mean and standard deviation of the positions of the particles. The momentum part is controlled by the mean kinetic energy and a standard deviation. So far no correlation between components of the momenta and components of the positions and vice versa can be modeled.

Besides positions and momenta of the particles both the total charge and the number of macroparticles are of importance for a simulation. A low particle density causes noise in the current density. On the other hand the propagation of particles and in particular the calculation of the current is expensive. The positions and momenta of the particles have to be updated twice per time step when using the TE/TM scheme. In each substep components of the electric field are updated. Thus the corresponding components of the current density are needed. To reduce this load several measures have been taken. In both substeps only those components of the current density that are needed are computed. This reduces the load by a factor two.

A term that is often computed for the update of the particles is $1/\gamma$ to get β from $\beta\gamma$. By replacing $1/\sqrt{1+\beta^2\gamma^2}$ with the fast inverse square root algorithm [122, 123] one can lower the load of the particle update considerably. This algorithm uses Newton's method to iteratively improve an initial guess. It was found that for $E_{\text{kin}} = 150 \text{ MeV}$ a single iteration step as is usually used [124] was not sufficient. Instead at least a second iteration step is needed.

Finally the particles are ordered according to their position in the bunch to increase the efficiency of the computation. For this all particles located inside a mesh cell are stored consecutively in memory. Unlike in [125] this is done only once at the beginning of the simulation. This should not lower the efficiency much since again the energy is high enough to prevent the particles from moving excessively around inside the bunch. However no large effect on the performance could be observed.

5.5 Output

A visual inspection of simulation results can help immensely to understand results or to correct errors. The fields can for this be written to disk in a Visualize ToolKit (VTK) [126] format or as H5Block [118]. For the latter the *H5hut* library is linked and only a thin layer of software is added. For the VTK file formats on the other hand two classes have been written to avoid to link to the library. The VTK library provides much more than is needed for this thesis. Instead only two dimensional scalar and vector fields on a rectilinear grid are needed. The interval of output of data for visualization can be chosen on command-line.

Two classes have been written for XML-based parallel VTK output, one for ASCII output and one for raw binary output. The output can be compressed according to the specifications. This can help to reduce the size of data that is written to disk and most likely also reduce the time to write to disk. On the one hand time is needed to compress the data while on the other hand less time is needed to write data to disk. The latter will probably outweigh the former. But this depends on the compression factor that is achieved. So far timings for the VTK output did not give cause to implement compression. It's rather the size of data that may justify this effort.

The size of data can not only be reduced by compression but also by sampling. So far one value is written for every cell and every vector component of a field. For visualization only this is overly detailed.

Finally a file has to be entirely written in ASCII to be a valid XML document. To comply with this specification one often encodes the data using the Base64 encoding scheme. But visualization applications that are built on the VTK library, such as *VisIt* [127] or *ParaView* [128], can also handle raw data as it is defined in the VTK specification. For this reason no urge has been felt to implement Base64 encoding.

Although visual results can be very helpful they often only yield an overview. Some detailed information can be extracted with help of the visualization applications such as plots of data along a line but not all information is accessible like this. Therefore more data than VTK or H5hut files have to be written.

Statistics on the particles are written in a Self Describing Data Sets (SDDS) [129] compliant file format. The corresponding class from OPAL with minor changes could be used. This provides mean position, mean energy, rms beam size, rms momentum, energy spread, normalized emittance and a few more measures such as the energy of the field. The field energy, $\frac{1}{2} (\epsilon_0 |\tilde{\mathbf{E}}|^2 + \mu_0 |\tilde{\mathbf{H}}|^2)$, is numerically integrated using zeroth order quadrature (rectangle rule). The interval for the calculation of statistics can also be chosen on command-line.

Furthermore the electromagnetic field along the central line of the bunch can be written to disk. The central line is parallel to the mean momentum and touches the mean position of the bunch. The coordinate system for these data is such that the x -axis is always parallel to the mean momentum of the bunch. The interval of this procedure can be controlled from the command-line.

A measure that is closely related to the latter is the energy gain along the bunch. It is the temporal integral of the electric field along the central line instead of a temporal snapshot. The interval between two sampling points in the integration can be chosen on command-line.

Finally detailed timings of the simulation is provided. The cpu time usage for important steps within the simulation are accumulated. This yields important information on bottlenecks, imbalances among the cores and overall performance.

Chapter Six

Results

6.1 Validation

To validate the solution of a FDTD simulation of a bend as depicted in Fig. 6.1 we used Liénard–Wiechert potentials (1.10). Both the charge distribution and the electric field are discretized on regular grids to keep the computational costs low. Contrary to the FDTD code the charge distribution is not considered as individual 2-dimensional particles at random positions and with momenta. Instead it is modeled as a Gaussian distribution with given total charge and standard deviation. It does not change its shape during the simulation. Its centroid drifts for an infinitely long time with a constant kinetic energy until it reaches the dipole field at $t = 0$. The path of the charge distribution is then bent by a magnetic dipole field. After leaving this field the charge distribution drifts again for an infinitely long time.

Inside the dipole field the distribution moves on a segment of a circle. The radius of the circle is given by the kinetic energy and the rest mass of an electron and by the strength of the magnetic field. The direction of deflection is given by the direction of the field and the velocity of the centroid.

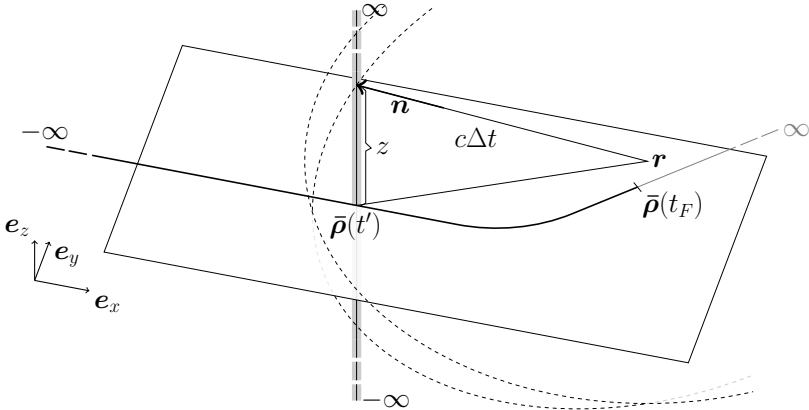


Figure 6.1: Sketch of situation for the calculation of Liénard-Wiechert potentials of a charged line at any point, \mathbf{r} , in the plane.

The path of the centroid of the charge density as depicted in Fig. 6.1 can be described by

$$\bar{\rho}(t) = \begin{cases} \beta ct \mathbf{e}_x & t \leq 0, \\ R \sin\left(\frac{\beta c}{R} t\right) \mathbf{e}_x + R(1 - \cos\left(\frac{\beta c}{R} t\right)) \mathbf{e}_y & 0 < t \leq \frac{R\varphi}{\beta c}, \\ (R \sin(\varphi) + \beta ct \cos(\varphi)) \mathbf{e}_x + (R(1 - \cos(\varphi)) + \beta ct \sin(\varphi)) \mathbf{e}_y & \frac{R\varphi}{\beta c} < t, \end{cases}$$

where R is the radius, φ the angle of deviation, β the relative speed of the centroid and c is the speed of light. This path is located in the plane $z = 0$. The magnetic dipole is of the form $\tilde{\mathbf{B}} = B \mathbf{e}_z$. For simplicity we assume that the magnet has hard edges, that is, there is no transition from outside to the constant magnetic field in the interior. In Fig. 6.1 as well as in the mathematical description above it is assumed that $B > 0$ since the charge density is bent towards $y > 0$. The direction of deflection is given by the Lorentz force $qc\beta \times \tilde{\mathbf{B}}$, where the charge of the electrons, q , is negative. The radius of the bend is given by $R = \beta \gamma m c^2 / |qB|c$, where mc^2 is the rest energy of an electron.

To calculate the electric field at any time $t_F \geq 0$ and at any point \mathbf{r} in the plane $z = 0$ one has to traverse the entire history of the path. For any moment $t' < t_F$ and for any location $\rho(t') + \delta\rho$ for which the charge density is not negligible one has to determine whether the equality,

$$c \cdot (t_F - t') \stackrel{?}{=} |\mathbf{r} - (\rho(t') + \delta\rho)|, \quad (6.1)$$

holds. For a given time t' and location \mathbf{r} in the plane all locations for which this equation holds are located on the surface of a sphere. The calculation of the field for all points that fulfill the equation is already quite costly but it won't suffice yet: so far we neglected the boundary conditions that are implemented in the FDTD simulation.

The PEC boundary condition has to be approximated with a series of image charges. Since the electric field in two dimensions decays as $1/r$ there are considerably more image

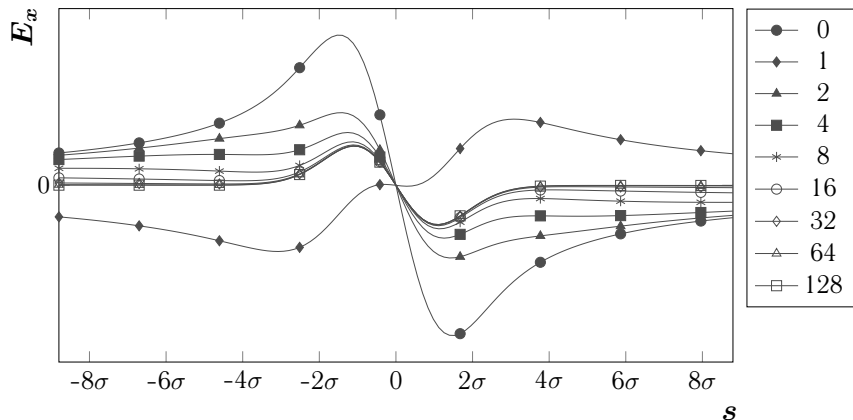


Figure 6.2: The influence of a variable number of image charges on the electric field. Plotted is the x-component of the electric field along a line for various number of image charges. The line is parallel to the momentum and goes through the centroid of the bunch. The bunch has a Gaussian charge distribution and is drifting for an infinitely long time.

charges needed than one copy on either side of the boundaries. Let's for now only consider the drift in front of the bend. We then have a PEC boundary at $y = -w/2$ and one at $y = w/2$. For any charge q at $y = \psi$ we will have an image with charge $-q$ at $y = -w - \psi$ and at $y = w - \psi$. These images in turn will cause images with charge $+q$ at $y = -2w + \psi$ and at $y = 2w + \psi$. This repeats infinitely many times with charge $(-1)^n q$ at $y = \pm w + (-1)^n \psi$ for $n = 3, 4, 5, \dots$. However the influence of a charge decreases with increasing distance. Thus the number of image charges can be limited. The influence of image charges on the electric field in the vicinity of the bunch is depicted in Fig. 6.2. As can be seen the difference between 64 and 128 is negligible. Thus 64 image charges on either side are sufficient here.

For a simulation the following parameters have to be provided

- Q the total charge,
- σ the standard deviation of the Gaussian charge distribution,
- E_{kin} the kinetic energy of the simulated electrons,
- L the distance of the bunch from the end of the bend at t_F , see Fig. 6.3,
- B the strength of the magnetic field,
- φ the angle of deviation, see Fig. 6.3,
- N_t the number of straight sections inside the bend,
- w the width of the vacuum chamber,
- N_i the number of image charges,
- N_x the number of grid cells in x-direction of the source grid,
- N_y the corresponding number in y-direction,

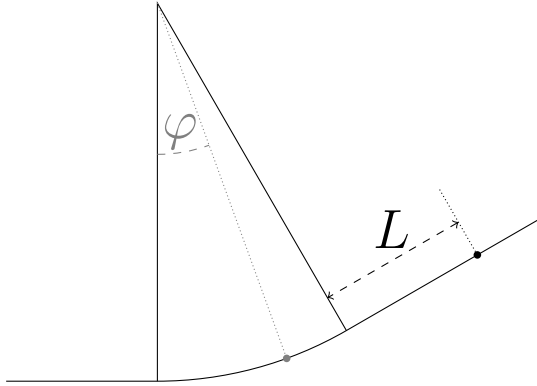


Figure 6.3: Path and parameters.

Δx the size of a grid cell in x-direction,

Δy the size of a grid cell in y-direction.

All the other quantities can be deduced from these parameters.

For the discretization of the Liénard-Wiechert potentials we split the history into three sections:

- o the drift in front of the bend where the bunch is not accelerated and therefore only the first term in (1.10) occurs,
- o the bend where also the acceleration field contributes,
- o the drift after the bend where the bunch is again not accelerated.

We split the segment of the circular path into N_t straight sections to simplify the evaluation of the Liénard-Wiechert potentials. To each section we assign an initial position, a constant velocity and a constant acceleration. N_t can be chosen freely but a too small N_t will deteriorate the result while the time to solution increases approximatley linearly with increasing N_t . A good initial guess is $N_t = {}^R\varphi/\beta\Delta x$ where Δx is the length of a cell of the grid. For this choice we assume that the same grid cell size is chosen as for the FDTD simulation. This specific choice N_t is equal to the number of steps that are needed by a particle in an FDTD/TETM simulation to traverse a bend with the same parameters.

For each section of the circular path the velocity and the acceleration is given by,

$$\boldsymbol{\beta}_k = \beta \begin{pmatrix} \cos(\frac{\varphi}{N_t} k) \\ \sin(\frac{\varphi}{N_t} k) \\ 0 \end{pmatrix},$$

$$\dot{\boldsymbol{\beta}}_k = \frac{\beta^2 c}{R} \begin{pmatrix} -\sin(\frac{\varphi}{N_t} k) \\ \cos(\frac{\varphi}{N_t} k) \\ 0 \end{pmatrix},$$

where $0 \leq k \leq N_t$. The path of a charged particle drifts between two time steps. The path for $t_k = k ({}^{R\varphi} / N_t \beta c) \leq t' < t_{k+1}$ can be written as

$$\begin{aligned}\boldsymbol{\rho}(t', z) &= \boldsymbol{\rho}_k + z \mathbf{e}_z + \boldsymbol{\beta}_k c(t' - t_k) \\ &= \boldsymbol{\rho}_k + z \mathbf{e}_z + \boldsymbol{\beta}_k c(t_F - t_k) - \boldsymbol{\beta}_k c(t_F - t') \\ &= \boldsymbol{\rho}_k + z \mathbf{e}_z + \boldsymbol{\beta}_k l - \boldsymbol{\beta} c \Delta t.\end{aligned}$$

For any point \mathbf{r} in the plane $z = 0$ one finds for the normal vector,

$$\mathbf{n} = \frac{\mathbf{r} - \boldsymbol{\rho}_k - \boldsymbol{\beta}_k l - z \mathbf{e}_z + \boldsymbol{\beta}_k c \Delta t}{c \Delta t} = \frac{\tilde{\mathbf{r}} - z \mathbf{e}_z + \boldsymbol{\beta}_k c \Delta t}{c \Delta t}.$$

By means of the equality (6.1) one finds

$$\frac{(c \Delta t)^2}{\gamma^2} - 2(\tilde{\mathbf{r}} \cdot \boldsymbol{\beta}) c \Delta t - \tilde{\mathbf{r}}^2 = z^2. \quad (6.2)$$

The part in (1.10) that is due to the velocity then becomes,

$$\begin{aligned}\frac{4\pi\epsilon_0\gamma^2}{q} \mathbf{E} &= \frac{\mathbf{n} - \boldsymbol{\beta}}{(1 - \mathbf{n} \cdot \boldsymbol{\beta})^3 (c \Delta t)^2} \\ &= \frac{\tilde{\mathbf{r}} - z \mathbf{e}_z}{(c \Delta t - \tilde{\mathbf{r}} \cdot \boldsymbol{\beta} - \boldsymbol{\beta}^2 c \Delta t)^3} \\ &= \gamma^6 \frac{\tilde{\mathbf{r}} - z \mathbf{e}_z}{(c \Delta t - \gamma^2 \tilde{\mathbf{r}} \cdot \boldsymbol{\beta})^3} \\ &= \gamma^3 \frac{\tilde{\mathbf{r}} - z \mathbf{e}_z}{(\gamma^2 (\tilde{\mathbf{r}} \cdot \boldsymbol{\beta})^2 + \tilde{\mathbf{r}}^2 + z^2)^{\frac{3}{2}}}.\end{aligned} \quad (6.3)$$

In the last step we solved (6.2) for $c \Delta t$ and inserted the result. The term $z \mathbf{e}_z$ in the final expression will not contribute since for any z that fulfills (6.1) also $-z$ will fulfill it. On the other hand the remaining term yields the same result for z and $-z$.

Similarly for the acceleration field:

$$\begin{aligned}\frac{4\pi\epsilon_0 c}{q} \mathbf{E} &= \frac{\mathbf{n} \times ((\mathbf{n} - \boldsymbol{\beta}) \times \dot{\boldsymbol{\beta}})}{(1 - \mathbf{n} \cdot \boldsymbol{\beta})^3 c \Delta t} \\ &= \gamma^6 \frac{(\tilde{\mathbf{r}} - z \mathbf{e}_z + \boldsymbol{\beta} c \Delta t) \times ((\tilde{\mathbf{r}} - z \mathbf{e}_z) \times \dot{\boldsymbol{\beta}})}{(c \Delta t - \gamma^2 \tilde{\mathbf{r}} \cdot \boldsymbol{\beta})^3} \\ &= \gamma^6 \frac{\tilde{\mathbf{r}} \times (\tilde{\mathbf{r}} \times \dot{\boldsymbol{\beta}}) + \boldsymbol{\beta} \times (\tilde{\mathbf{r}} \times \dot{\boldsymbol{\beta}}) c \Delta t - z^2 \dot{\boldsymbol{\beta}} - z ((\tilde{\mathbf{r}} + \boldsymbol{\beta} c \Delta t) \times (\mathbf{e}_z \times \dot{\boldsymbol{\beta}}))}{(c \Delta t - \gamma^2 \tilde{\mathbf{r}} \cdot \boldsymbol{\beta})^3} \\ &= \frac{\gamma^3}{(\gamma^2 (\tilde{\mathbf{r}} \cdot \boldsymbol{\beta})^2 + \tilde{\mathbf{r}}^2 + z^2)^{\frac{3}{2}}} \left(-\dot{\boldsymbol{\beta}} z^2 \right. \\ &\quad \left. + \gamma \boldsymbol{\beta} \times (\tilde{\mathbf{r}} \times \dot{\boldsymbol{\beta}}) (\gamma^2 (\tilde{\mathbf{r}} \cdot \boldsymbol{\beta}) + \tilde{\mathbf{r}}^2 + z^2)^{\frac{1}{2}} \right. \\ &\quad \left. + (\tilde{\mathbf{r}} + \gamma^2 (\tilde{\mathbf{r}} \cdot \boldsymbol{\beta}) \boldsymbol{\beta}) \times (\tilde{\mathbf{r}} \times \dot{\boldsymbol{\beta}}) \right),\end{aligned} \quad (6.4)$$

where again we replaced $c\Delta t$ by the solution of (6.2).

Both the velocity field, (6.3), and the acceleration field, (6.4), can then be integrated along z from $-\infty$ to ∞ . For every step k we have to determine z_k and z_{k+1} from $c\Delta t_k$ and $c\Delta t_{k+1}$ respectively. The velocity field then becomes

$$\begin{aligned} \frac{4\pi\varepsilon_0}{\gamma q} \mathbf{E} &= 2\tilde{\mathbf{r}} \int_{z_{k+1}}^{z_k} \frac{1}{(\gamma^2(\tilde{\mathbf{r}} \cdot \boldsymbol{\beta})^2 + \tilde{\mathbf{r}}^2 + z^2)^{\frac{3}{2}}} dz \\ &= \frac{2\tilde{\mathbf{r}}}{\gamma^2(\tilde{\mathbf{r}} \cdot \boldsymbol{\beta})^2 + \tilde{\mathbf{r}}^2} \left(\frac{z_k}{\sqrt{\gamma^2(\tilde{\mathbf{r}} \cdot \boldsymbol{\beta})^2 + \tilde{\mathbf{r}}^2 + z_k^2}} - \frac{z_{k+1}}{\sqrt{\gamma^2(\tilde{\mathbf{r}} \cdot \boldsymbol{\beta})^2 + \tilde{\mathbf{r}}^2 + z_{k+1}^2}} \right). \end{aligned} \quad (6.5)$$

Likewise integrating (6.4) from z_{k+1} to z_k yields

$$\begin{aligned} \frac{4\pi\varepsilon_0 c^2}{\gamma^3 q} \mathbf{E} &= -\dot{\boldsymbol{\beta}} \int_{z_{k+1}}^{z_k} \frac{z^2}{(\gamma^2(\tilde{\mathbf{r}} \cdot \boldsymbol{\beta})^2 + \tilde{\mathbf{r}}^2 + z^2)^{\frac{3}{2}}} dz \\ &\quad + \gamma \boldsymbol{\beta} \times (\tilde{\mathbf{r}} \times \dot{\boldsymbol{\beta}}) \int_{z_{k+1}}^{z_k} \frac{1}{(\gamma^2(\tilde{\mathbf{r}} \cdot \boldsymbol{\beta})^2 + \tilde{\mathbf{r}}^2 + z^2)^{\frac{3}{2}}} dz \\ &\quad + (\tilde{\mathbf{r}} + \gamma^2(\tilde{\mathbf{r}} \cdot \boldsymbol{\beta})\boldsymbol{\beta}) \times (\tilde{\mathbf{r}} \times \dot{\boldsymbol{\beta}}) \int_{z_{k+1}}^{z_k} \frac{1}{(\gamma^2(\tilde{\mathbf{r}} \cdot \boldsymbol{\beta})^2 + \tilde{\mathbf{r}}^2 + z^2)^{\frac{3}{2}}} dz \\ &= -\dot{\boldsymbol{\beta}} A \\ &\quad + \gamma \boldsymbol{\beta} \times (\tilde{\mathbf{r}} \times \dot{\boldsymbol{\beta}}) B \\ &\quad + (\tilde{\mathbf{r}} + \gamma^2(\tilde{\mathbf{r}} \cdot \boldsymbol{\beta})\boldsymbol{\beta}) \times (\tilde{\mathbf{r}} \times \dot{\boldsymbol{\beta}}) C, \end{aligned} \quad (6.6)$$

where

$$\begin{aligned} A &= -\frac{z_k}{\sqrt{\gamma^2(\tilde{\mathbf{r}} \cdot \boldsymbol{\beta})^2 + \tilde{\mathbf{r}}^2 + z_k^2}} + \operatorname{arcsinh} \left(\frac{z_k}{\sqrt{\gamma^2(\tilde{\mathbf{r}} \cdot \boldsymbol{\beta})^2 + \tilde{\mathbf{r}}^2}} \right) \\ &\quad + \frac{z_{k+1}}{\sqrt{\gamma^2(\tilde{\mathbf{r}} \cdot \boldsymbol{\beta})^2 + \tilde{\mathbf{r}}^2 + z_{k+1}^2}} - \operatorname{arcsinh} \left(\frac{z_{k+1}}{\sqrt{\gamma^2(\tilde{\mathbf{r}} \cdot \boldsymbol{\beta})^2 + \tilde{\mathbf{r}}^2}} \right) \\ B &= \frac{1}{\sqrt{\gamma^2(\tilde{\mathbf{r}} \cdot \boldsymbol{\beta})^2 + \tilde{\mathbf{r}}^2}} \left(\arctan \left(\frac{z_k}{\sqrt{\gamma^2(\tilde{\mathbf{r}} \cdot \boldsymbol{\beta})^2 + \tilde{\mathbf{r}}^2}} \right) - \arctan \left(\frac{z_{k+1}}{\sqrt{\gamma^2(\tilde{\mathbf{r}} \cdot \boldsymbol{\beta})^2 + \tilde{\mathbf{r}}^2}} \right) \right) \\ C &= \frac{1}{\gamma^2(\tilde{\mathbf{r}} \cdot \boldsymbol{\beta})^2 + \tilde{\mathbf{r}}^2} \left(\frac{z_k}{\sqrt{\gamma^2(\tilde{\mathbf{r}} \cdot \boldsymbol{\beta})^2 + \tilde{\mathbf{r}}^2 + z_k^2}} - \frac{z_{k+1}}{\sqrt{\gamma^2(\tilde{\mathbf{r}} \cdot \boldsymbol{\beta})^2 + \tilde{\mathbf{r}}^2 + z_{k+1}^2}} \right) \end{aligned}$$

The charge distribution is discretized on a regular grid of size 8σ in both space dimensions. The number of grid cells is given by N_x and N_y respectively. For the discretization of the charge distribution on the grid we assigned charge densities to the grid nodes as

$$\frac{d q_{i,j}}{dz} = \int_{-\Delta x/2}^{\Delta x/2} \int_{-\Delta y/2}^{\Delta y/2} \exp \left(-\frac{(i\Delta x + x)^2 + (j\Delta y + y)^2}{2\sigma^2} \right) dy dx.$$

Every 2-dimensional particle reaches from $z \rightarrow -\infty$ to $z \rightarrow \infty$ and it has a constant line density.

The electric field is evaluated on a grid that is centered around the location of the centroid at t_F , $\bar{\rho}(t_F)$. The size of this grid is preset to 16σ in both dimensions. The number of grid cells is $2N_x \times 2N_y$, i.e. twice as big in each dimension as the source grid. The components of the electric field are discretized in the middle of the edges such as it is the case for finite-differences.

To achieve an effect similar to a grid effect [45, Chapter 8] we have to average the fields over the area of a grid cell centered around the sampling point.

$$\begin{aligned}\mathbf{E}_x{}_{i+1/2,j} &= \frac{1}{\Delta x \Delta y} \int_{x_i}^{x_{i+1}} \int_{y_{j-1/2}}^{y_{j+1/2}} \mathbf{E}_x(x, y) \, dx \, dy, \\ \mathbf{E}_y{}_{i,j+1/2} &= \frac{1}{\Delta x \Delta y} \int_{x_{i-1/2}}^{x_{i+1/2}} \int_{y_j}^{y_{j+1}} \mathbf{E}_y(x, y) \, dx \, dy.\end{aligned}$$

In this form we can evaluate the Liénard-Wiechert potentials.

The limits of the temporal integration in (6.5) and (6.6) are not always correct. All integrals will vanish in the case where the left hand side of (6.2) is negative for $c\Delta t_k$. One has to adjust the upper limit in the case where the left hand side of (6.2) is positive for $c\Delta t_k$ but negative for $c\Delta t_{k+1}$. The lower limit then becomes $z_{k+1} = 0$.

For the drifts before and after the bend one only has to evaluate the velocity field. They can be evaluated in one piece with appropriate limits. For the drift in front of the bend one chooses

$$\begin{aligned}z_k &= \infty, \\ z_{k+1} &= \sqrt{\max \left(0, \frac{(c\tau)^2}{\gamma^2} - 2\tilde{\mathbf{r}} \cdot \beta(c\tau) - \tilde{\mathbf{r}}^2 \right)},\end{aligned}$$

where $\tau = (R\varphi + L)/\beta c$ is the time difference between the moment the bunch enters the bend to the moment when the bunch reaches a distance L to the exit of the bend.

In the case of the drift after the bend we chose

$$\begin{aligned}z_k &= \sqrt{\max \left(0, \frac{(c\tau)^2}{\gamma^2} - 2\tilde{\mathbf{r}} \cdot \beta(c\tau) - \tilde{\mathbf{r}}^2 \right)} \\ z_{k+1} &= 0,\end{aligned}$$

where $\tau = \frac{L}{\beta c}$ is the time difference between the moment the bunch leaves the bend to the simulated present.

One then has to loop over all straight segments ($N_t + 2$) and evaluate the fields for every cell of the receiver field ($2N_x \times 2N_y$), for every cell of the source field ($N_x \times N_y$), for every image ($1 + 2N_i$) and for both components separately. Thus there are

$$8N_x^2 N_y^2 (1 + 2N_i)(N_t + 2)$$

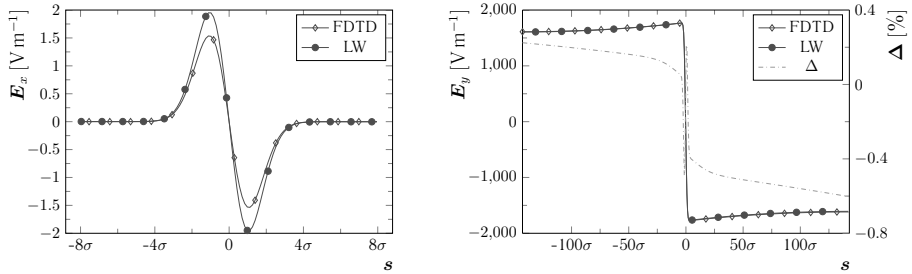


Figure 6.4: Comparison between the solution of an FDTD simulation and the Liénard-Wiechert potentials. On the left hand side the x-component of the electric field along $y = 0$ is plotted. On the right hand side is the y-component along $x = 0$. The bunch is Gaussian, has a standard deviation of 0.7 mm and a kinetic energy of 150 MeV. The velocity is parallel to the x -axis.

evaluations needed. Even for very moderately large N_x , N_y and N_z this becomes very time consuming. To compare the fields with the FDTD solution one often does not need the solutions for the full receiver field. Instead one is interested in the field along a single line. For this one evaluates the components on all four edges of every cell that contains part of that line. In the end one calculates the field on the line by interpolation such as it is done in the FDTD case. The field is rotated into the coordinate system for which the x-component is parallel to the line.

Fortunately one can speed up the evaluation. If one just for now assumes that the charge density on the source field is constant and equal to one then the field on the receiver field only depends on the distance and the direction relative to the velocity of the centroid. The combination (source field) $_{m,n} \rightarrow$ (receiver field) $_{i,j}$ yields the same result as (source field) $_{m+u,n+v} \rightarrow$ (receiver field) $_{i+u,j+v}$. In a first step an auxiliary vector field of size $3N_x \times 3N_y$ is allocated. Then one loops over all straight segments, every image and every cell of this auxiliary field and both components and determines the field caused by a single cell of the source field. In a second step one then loops over every cell of the actual receiver field and over every cell of the source field and accumulates the corresponding values from the auxiliary field. Like this one can reduce the expensive part by a factor $4N_x N_y / 9$.

For the parallelization this improvement causes a small complication. Before the improvement one splits the receiver field into equally large pieces. The charge density is cheap enough to calculate on the fly such that it's not needed to be stored. With the improvement one will also split the auxiliary field into equally large pieces and evaluate the fields. Now before one can accumulate the fields in the actual field one has to communicate those source/receiver combinations that are not local on the auxiliary field. Fortunately this has to be done only once such that the overhead remains small.

The y-component of the field for the drift in front of the bend matches very well with the solution of an FDTD simulation as can be seen on the right hand side in Fig. 6.4. For the x-component it does not yield so good results. Though if the x-component is not averaged over a cell then the result matches very well in x-direction as can be seen on the left hand

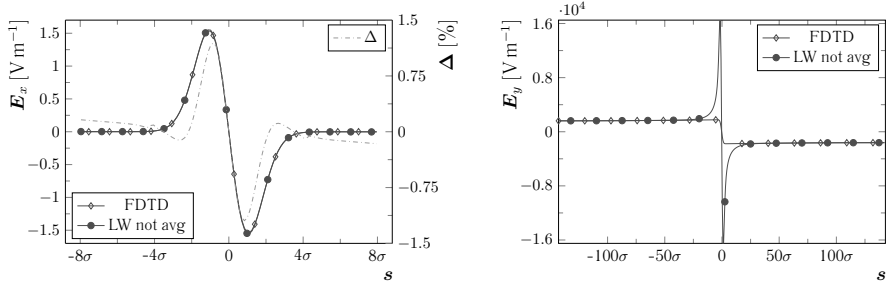


Figure 6.5: The same plots as in Fig. 6.4 with the difference that the Liénard-Wiechert solutions are not averaged over a grid cell.

side in Fig. 6.5. But then the result for the y-component does not fit at all in the vicinity of the bunch.

The drift in front of the bend also contributes to the solution when the bunch is inside or after the bend. The information that the bunch has been deflected from its straight path spreads with the speed of light. The limit between the region where this information is known and where it can not have reached yet is the horizon, see Fig. 1.1 and equation (6.1). The field beyond this horizon will still look like the bunch had not been bent. The field lines point to the location where the bunch would be if it had not been bent. The averaged Liénard-Wiechert potentials for the velocity field yield far better results also in the the region beyond the horizon than the not averaged version. This is due to the fact that the solution of the averaged version does not depend on where the projected location of the centroid is located inside a cell. Thus the divergence due to very small distances can be avoided.

The parameters for the simulation inside and after the bend can be found in Table 6.1. For both the FDTD simulation as well as the Liénard-Wiechert simulation the same parameters are chosen. The grid size is chosen such that in x-direction there are approximately 7 grid cells per σ of the charge distribution. This should be sufficiently small to reproduce wave length of similar length as the bunch while the results are obtained in reasonable time.

Table 6.1: Parameters for the comparison between FDTD and Liénard-Wiechert potentials.

kinetic energy	150 MeV
total charge	55.44 pC
standard deviation of distribution, σ	700 μm
magnetic field	0.502 T
final angle of deflection	5°
length of drift after bend	1 m
width of vacuum chamber	0.2 m
cell size in x-direction, Δx	97.7517 μm
cell size in y-direction, Δy	393.701 μm
number of particles in FDTD simulation	$1 \cdot 10^7$

For the Liénard-Wiechert solution we assume that the path of the centroid after the initial drift follows a parametrized curve as depicted in Fig. 6.3. The time difference between a chosen present and the moment when the bunch enters the bend is determined by the two parameters φ and L . If $L = 0$ and $\varphi > 0$ then the bunch is inside the bend, if $L > 0$ and $\varphi = \varphi_{\text{final}}$ then the bunch is in the drift that follows the bend. Also the location of the centroid, the velocity of the bunch and the acceleration of it are determined from φ and L . The mesh is then centered around the location of the centroid. The field components are then sampled at the middle of the according edges.

The visual comparison between the two codes shows a good agreement for both the x-component in Fig. 6.7 as well as the y-component in Fig. 6.8. One can observe that the center of the FDTD solution moves slightly from time step to another since the mesh is not centered around the centroid of the bunch.

For a more rigorous comparison we plot the fields along the line that contains the centroid of the bunch and that is parallel to the velocity. The fields are interpolated at several locations along that line. The resulting field is then transformed to the Cartesian coordinate system for which the x -axis is parallel to the line. The result for the x-component is found in Fig. 6.9. As already seen the solution for the situation in which the bunch is in front of the bend does not match well. Similarly the solution does not match well after the bunch enters the bend, see Fig. 6.9a. After the bend and for up to ~ 0.25 m the solutions match well, Fig. 6.9b. Thereafter a reflection from the boundary that is not included in the Liénard-Wiechert model disturbs the good agreement, Fig. 6.9c-h. This reflection is shown in an overview in Fig. 6.10 and more detailed in Fig. 6.11.

The disturbance is caused by the drift field that reflects on the upper boundary of the geometry. In Fig. 6.10a and Fig. 6.11a the reflection is still outside the region for which we calculate the Liénard-Wiechert solution. In Fig. 6.10b and Fig. 6.11b it is already visible in the clipping but it does not influences the field on the line that is tilted by 5° and that ends at the border of the clipping. The reflection then disturbs the solution on the line in Fig. 6.10c-f and in Fig. 6.11c-f. It also disturbs the solution for all remaining time steps and beyond the end of the simulation at $L = 1$ m.

To assess the agreement between the two methods we tried to match the solution as produced with FDTD. For this we produce a solution by superposing the velocity and the acceleration field with weights:

$$\tilde{\mathbf{E}}_x = w_v \tilde{\mathbf{E}}_{\text{vel},x} + w_a \tilde{\mathbf{E}}_{\text{acc},x} \quad (6.7)$$

We then search the maximum and the minimum of the FDTD solution and the respective positions. Then we solve the equations

$$\begin{aligned} w_v \tilde{\mathbf{E}}_{\text{vel},x}(\mathbf{r}_{\min}) + w_a \tilde{\mathbf{E}}_{\text{acc},x}(\mathbf{r}_{\min}) &= \tilde{\mathbf{E}}_{\text{FDTD},x}(\mathbf{r}_{\min}) \\ w_v \tilde{\mathbf{E}}_{\text{vel},x}(\mathbf{r}_{\max}) + w_a \tilde{\mathbf{E}}_{\text{acc},x}(\mathbf{r}_{\max}) &= \tilde{\mathbf{E}}_{\text{FDTD},x}(\mathbf{r}_{\max}). \end{aligned}$$

With these weights we then search for the positions at which the combination (6.7) has its maximum, \mathbf{r}'_{\max} , and minimum, \mathbf{r}'_{\min} , respectively. Then we correct the weights by solving

$$\begin{aligned} w_v \tilde{\mathbf{E}}_{\text{vel},x}(\mathbf{r}'_{\min}) + w_a \tilde{\mathbf{E}}_{\text{acc},x}(\mathbf{r}'_{\min}) &= \tilde{\mathbf{E}}_{\text{FDTD},x}(\mathbf{r}_{\min}) \\ w_v \tilde{\mathbf{E}}_{\text{vel},x}(\mathbf{r}'_{\max}) + w_a \tilde{\mathbf{E}}_{\text{acc},x}(\mathbf{r}'_{\max}) &= \tilde{\mathbf{E}}_{\text{FDTD},x}(\mathbf{r}_{\max}). \end{aligned}$$

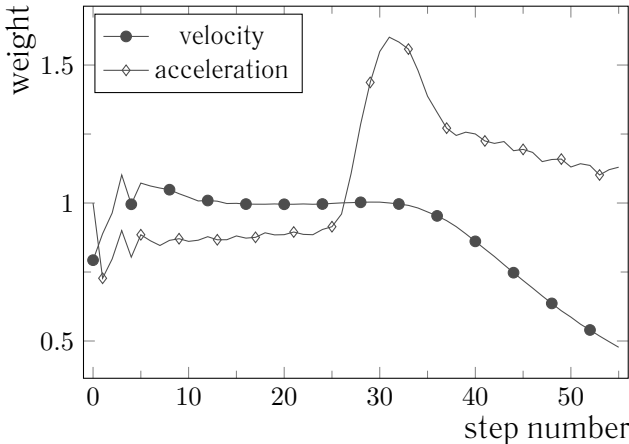


Figure 6.6: Weights for the velocity and the acceleration field to match the maximum and the minimum of the FDTD solution.

The reason for this second step is that the two solutions can have a shift in space which we assume that it is small. With the second step we make sure that the maximum and the minimum of the superposition is equal to the maximum and minimum of the FDTD solution.

The resulting superpositions match well with the FDTD solution as long as the reflection does not change neither maximum nor minimum as can be seen in Fig. 6.12. The above procedure does not produce good matches when the reflection does change one of the two. This can be seen from Fig. 6.6 where the weights are plotted. After step 25 the weight for the acceleration field increases abruptly. The contribution of the acceleration field to the maximum in this region is far stronger than the one from the velocity field which can also be observed in Fig. 6.9 and Fig. 6.12. The weight for the velocity plunges after step 32 when the reflection lifts the minimum of the FDTD solution.

In Fig. 6.6 one can also observe that the velocity field is very well approximated by the Liénard-Wiechert solution right after the bend. The weight for the acceleration field on the other hand hovers around 0.9 until the action of the reflection influences the weights.

Another source for possible differences between the two results is the oversimplified charge distribution. While the distribution may and will change during an FDTD simulation it is modeled as a rigid Gaussian in the Liénard-Wiechert approach. This rigidity is not fulfilled in particular at the entry and the exit of the bend. There is a smooth transition between the drifts and the bend. This transition phase starts when the particles at the head of the bunch enter the bend respectively leave it. And it ends when the particles at the tail enter the bend respectively leave it. Furthermore the distribution will be slightly distorted inside the bend compared to a perfect Gaussian due to the curved path. These differences are small but the fields change also rapidly in the vicinity of the centroid.

Not only the path of the particles is over simplified but also the velocity and the accel-

eration. Again there are smooth transitions at the entry and the exit of the bend. We underestimate them when some particles entered the bend while the centroid is still outside and we overestimate them when the centroid is inside but not all particles behind. Similarly at the exit where we first overestimate and then underestimate them. Again these differences are small but particularly the change of velocity is large at the chosen kinetic energy.

Although the TE/TM does not exhibit dispersion in the longitudinal direction it shows dispersion in the transverse direction. The chosen angle is small that the dispersion does not cause numerical Cerenkov radiation. No other obvious evidence of dispersion are observed in the result but it certainly does cause a small error in the FDTD solution.

For the Liénard-Wiechert solution we tried to add a grid effect by smoothing the result but the FDTD approach introduces further errors beyond the smoothing. These local approximation errors are of second order with respect to the mesh size. Thus these errors and the smoothing are reduced by finer meshes. The Liénard-Wiechert approach does not exhibit these errors since it is based on analytic solutions. On the other hand we rely on numerical integration for the smoothing but this error does not propagate to later time steps since we have to compute every time step separately.

The Liénard-Wiechert approach does exhibit another benefit beyond the validation of the FDTD solution. It also exposes the contributions of the velocity field and the acceleration field separately.

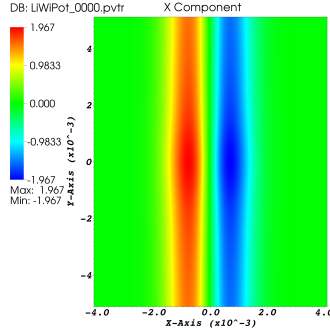
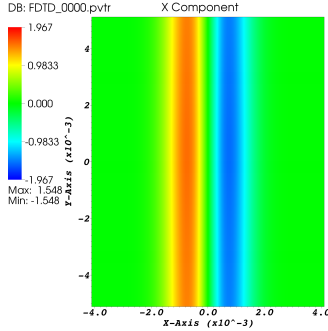
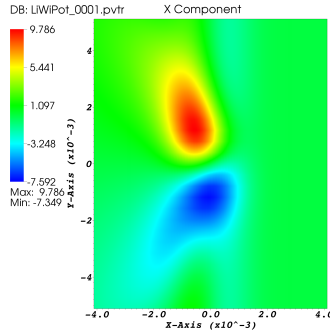
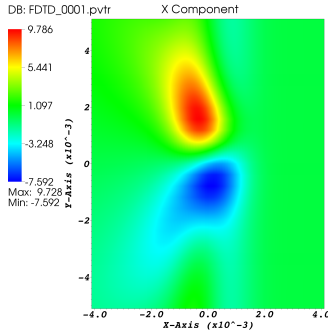
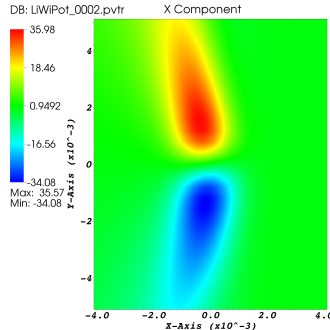
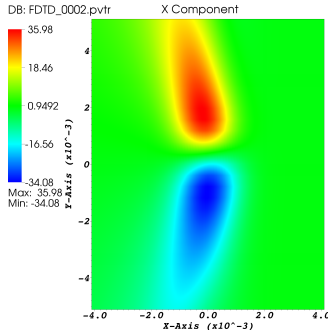
(a) The position here is $\varphi = 0^\circ$ and $L = 0$ m.(b) The position here is $\varphi = 0.496^\circ$ and $L = 0$ m.(c) The position here is $\varphi = 1.616^\circ$ and $L = 0$ m.

Figure 6.7: Comparison between the x-components of the electric field of the solutions of an FDTD/TETM simulation on the left and the corresponding solution derived with Liénard-Wiechert potentials on the right. The chosen parameters can be found in Table 6.1.

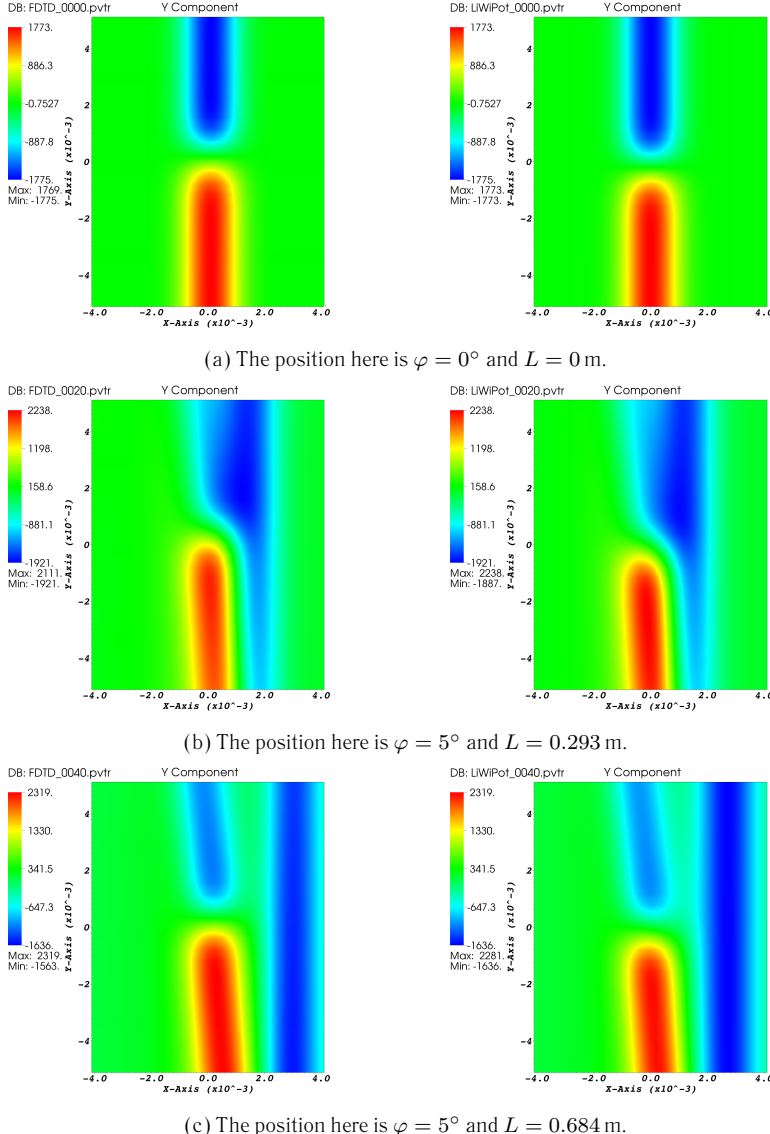


Figure 6.8: Comparison between the y-components of the electric field of the solutions of an FDTD/TETM simulation on the left and the corresponding solution derived with Liénard-Wiechert potentials on the right. The chosen parameters can be found in Table 6.1.

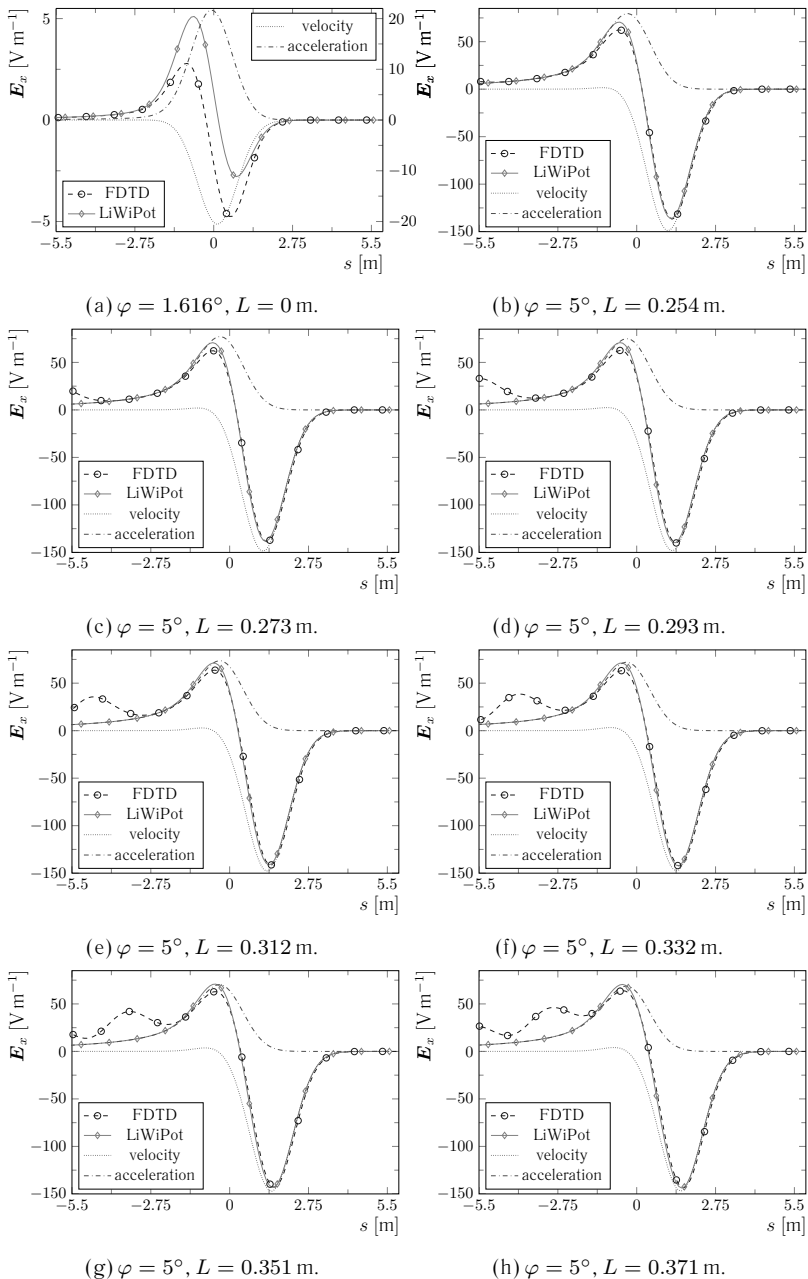


Figure 6.9: X-component of the electric field along the line that contains the centroid of the bunch and that is parallel to the velocity at different positions along the path.

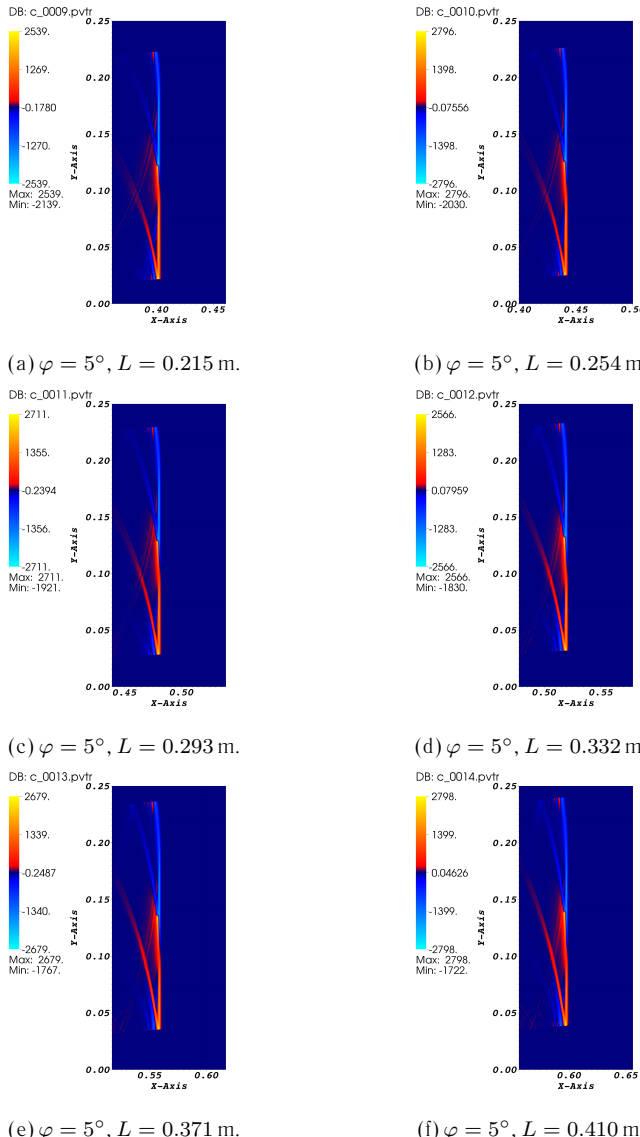


Figure 6.10: Visualization of the x-component of the electric field of the FDTD when the reflection on the upper boundary disturbs the solution the line that contains the centroid and that is parallel to the velocity.

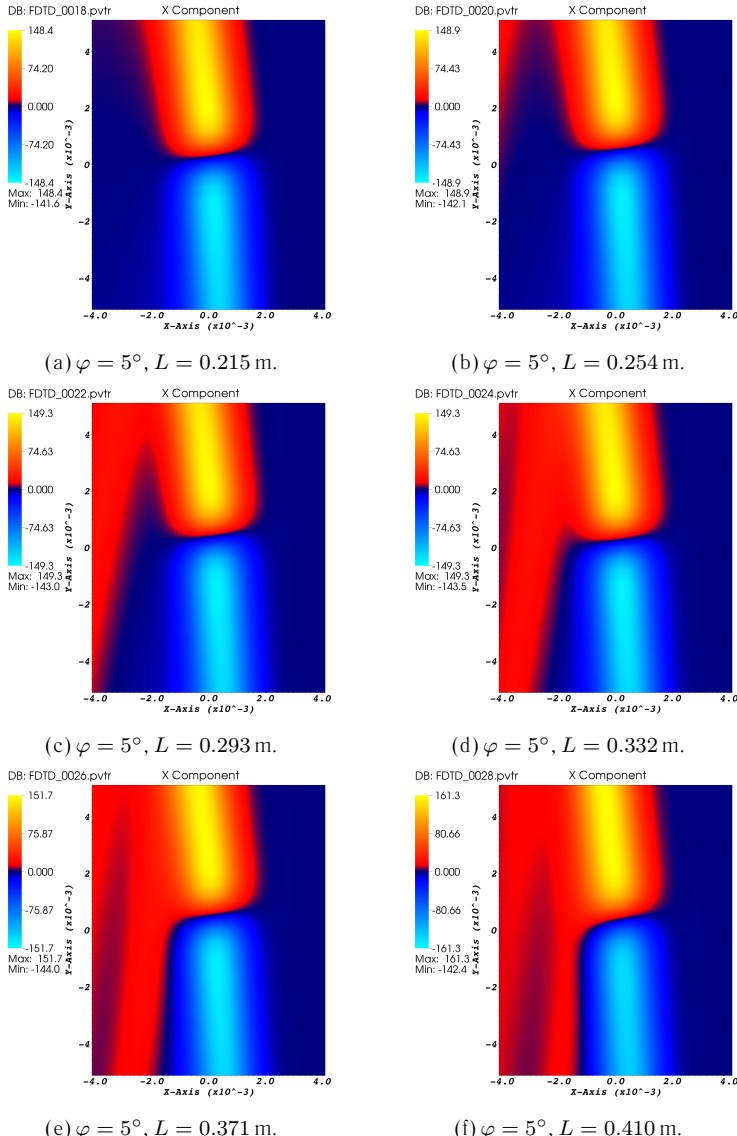


Figure 6.11: Visualization of the x-component of the electric field of the FDTD around the centroid of the bunch when the reflection on the upper boundary disturbs the solution on the line that contains the centroid and that is parallel to the velocity.

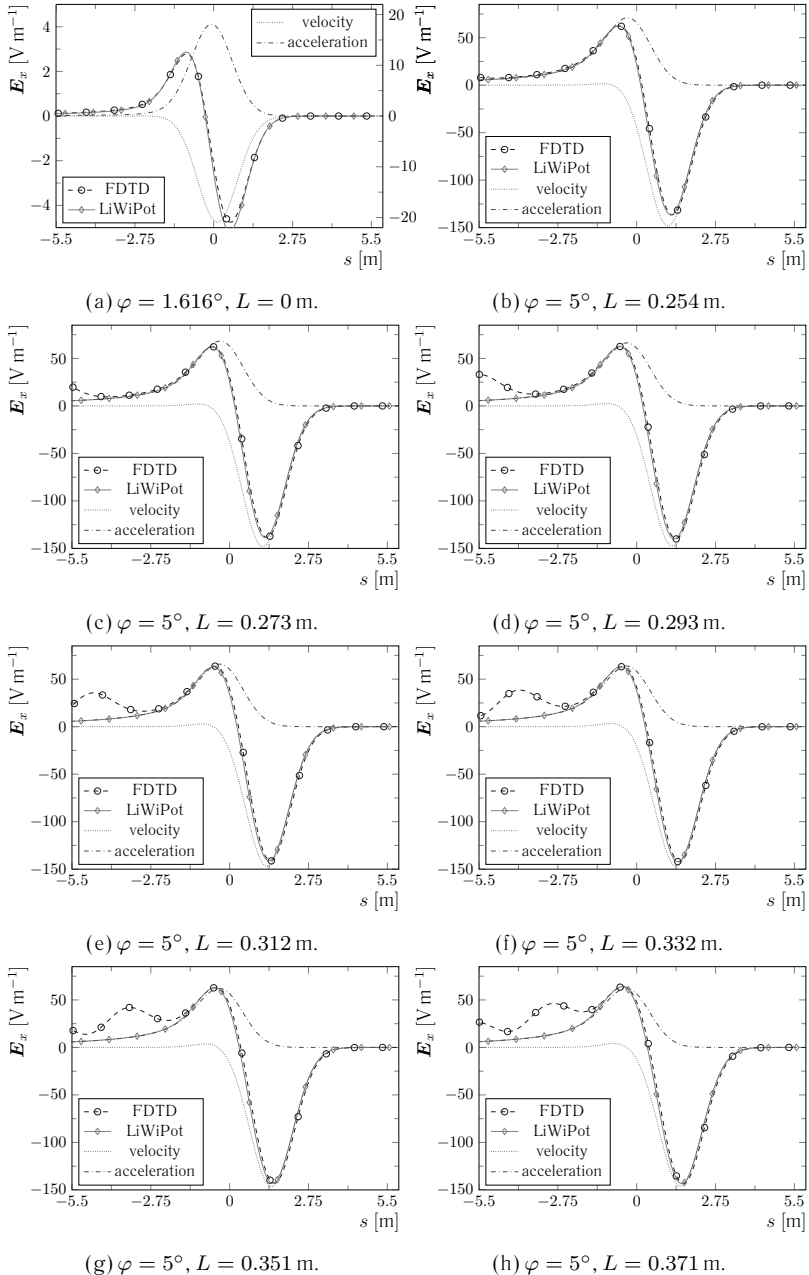


Figure 6.12: The x-component of the electric field along the line that contains the centroid of the bunch adjusted with weights to match the FDTD solution.

6.2 Scalability

In Section 5.1 we already discussed why here the most simple approach to parallelization doesn't work. The simplest approach is to let the node that updates the field in the vicinity of a particle also update the position and velocity of the particle. The problem with this approach is that the particles are localized in a small region of the domain. This could lead to a perfect balance of the fields and the worst possible balance of particles.

We then delved into the possibilities to improve the parallelization. One approach is to distribute the particles evenly between the cores. Then the cores that update the fields in the vicinity of the particles have to send the electromagnetic field of this vicinity to all other cores. All the other cores then have to send the current density field that is caused by those particles that they possess back after updating the positions and momenta of the particles. This approach is realized in revision 13734 of the code.

The amount of data that has to be moved depends on the spread of the particles and on the size of the mesh cells. If we assume that the Gaussian particle distribution has a maximal extent of 10σ in both x-direction and y-direction and that we use 10 cells per σ in the x-direction and 3 cells in the y-direction then the field that has to be communicated among the cores has a size of 100×30 cells. For every cell we have two components of electric field and a single component of the magnetic field for the scattering process and two components of current density for the gathering process. Thus the total amount of data is small for these parameters. The chosen parameters are realistic since we expect coherent radiation with wave length in the order of the bunch size. In the transverse dimension we are free to choose a bigger cell size since the CFL condition of the explicit TE/TM scheme only depends on the longitudinal cell size.

A more sophisticated approach was chosen for the current revision of the code. Here an auxiliary mesh was used. The auxiliary mesh is a few cells larger in each dimension than the size of the region of the particles. The mesh is split as evenly among the cores as possible. In a first step every core receives those particles that are located within its patch of the mesh. Then every core that has more particles than the average becomes master of zero or more other cores. The remaining cores are then assigned to the masters in such a way that the load due to the particles is as even among the cores as possible without sharing slaves.

The load due to the auxiliary mesh is not shared perfectly among the cores since the small number of cells in each dimension is not necessarily divisible evenly. This imbalance though does not harm since the local fields are so small. Furthermore the number of particles is not perfectly uniform among the cores but the difference is small and so should not harm either. The amount of data that has to be scattered and gathered for the update of the particles is about half as big since approximately every second core is master. Only the masters have to scatter their local field and then gather the current density from their slaves.

The drawbacks of this approach are first that the auxiliary mesh is very small and the ratio of number of guard cells to the total number of cells is unfavorable. Second, that the effort to synchronize the main mesh with the auxiliary mesh is enormous as we will see shortly.

The scaling tests were performed on a machine with 15 blades with two 2.6 GHz 8 core Intel Xeon CPUs (E5-2670) each. On every blade there are 64 GB of RAM. The blades are interconnected with Infiniband.

In Fig. 6.13a we find the strong scaling of the current version. For the test of strong

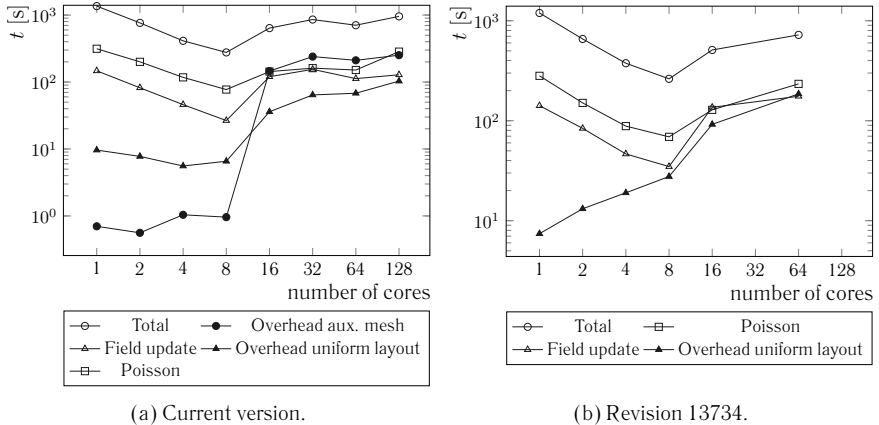


Figure 6.13: Strong scaling test.

scaling we chose a field with 4096×1024 cells, $2.5 \cdot 10^6$ particles and a straight domain with a length and width of 0.2 m. The mean kinetic energy of the particles is 150 MeV with no energy spread. The Gaussian particle distribution has a total charge of 55.4 pC and a σ of 700 μm . The cell size for the chosen parameters is approximately $48.9 \mu\text{m} \times 195.7 \mu\text{m}$. Finally the auxiliary mesh has a size of 157×47 cells. We let the code to first calculate the Poisson solution and then update the positions and velocities of the particles and the electromagnetic fields for 500 steps.

The current code scales nicely up to 8 cores. This is the case for the two largest contributors that are included in the graph namely the calculation of the initial field as well as the update of it. The update of the particles and the calculation of the current density are also big contributors but are not included here since they scale nicely up to 128 cores and their inclusion would reduce the readability of the graph. The overhead due to the uniform particle layout as well as the overhead due to the auxiliary mesh don't scale well. However their contribution remains small up to 8 cores.

The overhead due to the auxiliary mesh increases two orders of magnitude for 16 cores and rises only slightly for more cores. Also the overhead due to the uniform particle layout increases vigorously for 16 cores and more but not as drastically as for the auxiliary mesh. Finally also the Poisson solver as well as the update of the fields of the main mesh increase with 16 cores and more.

The revision 13 734 of the code could not be scaled to 128 cores due to a segmentation fault. For the same reason it would also not run with 32 cores. Nonetheless it seems to yield reasonable timings for the other scaling steps, see Fig. 6.13b.

Revision 13 734 does not feature the auxiliary mesh but uses a uniform particle layout. Only the communication overhead due to the uniform layout rises up to 8 cores. Between 8 and 16 cores then all timings increase and rise more gently for more cores. Overall it behaves very similarly to the newest version with the exception of the lack of overhead due to the auxiliary mesh.

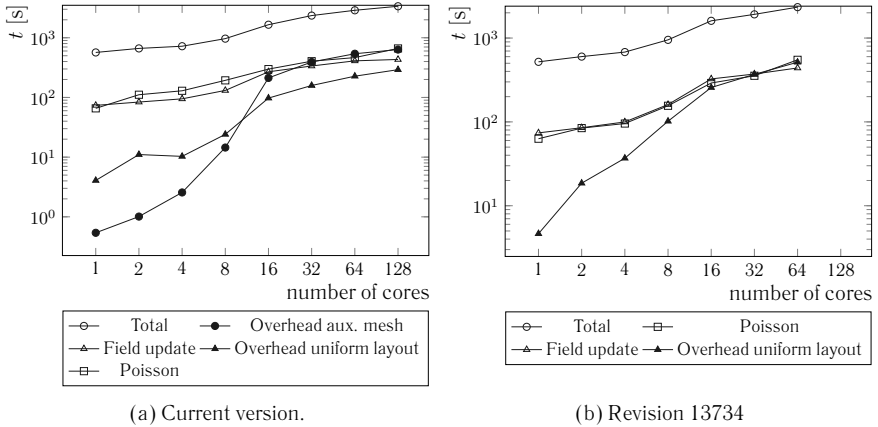


Figure 6.14: Weak scaling test.

The sharp rise of consumed time for communication in connection with the auxiliary mesh between 8 and 16 cores is also present in the test for weak scaling see Fig. 6.14a. The parameters used here can be found in Table 6.2.

Table 6.2: Parameters for weak scalability test.

# cores	1	2	4	8	16	32	64
Length				0.2 m			
Width				0.2 m			
Charge				55.4 pC			
σ				700 μ m			
# cells	2^{20}	2^{21}	2^{22}	2^{23}	2^{24}	2^{25}	2^{26}
# particles	$1 \cdot 10^6$	$2 \cdot 10^6$	$4 \cdot 10^6$	$8 \cdot 10^6$	$16 \cdot 10^6$	$32 \cdot 10^6$	$64 \cdot 10^6$
# cells aux. mesh	76 \times	110 \times	157 \times	217 \times	310 \times	444 \times	644 \times
# steps	28	36	47	63	88	123	178
				1000			

Instead of increasing the length and the width of the domain we chose to only increase the number of cells. This leads to finer meshes with increasing number of cores. This in turn makes sure that the number of cells in the auxiliary mesh increase. We would have ended up with a mixed scaling with partly weak and partly strong scaling if we had chosen to keep the cell size constant while increasing the number of cells. In real applications one is most often interested in increasing the domain while keeping the cell size constant at a size that can resolve the shortest wave lengths expected. However the behavior of the auxiliary mesh under strong scaling has already been shown. Here the weak scaling test would be dominated by the strong scaling of the auxiliary mesh. This we wanted to avoid.

The behavior of both code versions under weak scaling is not further noticeable except

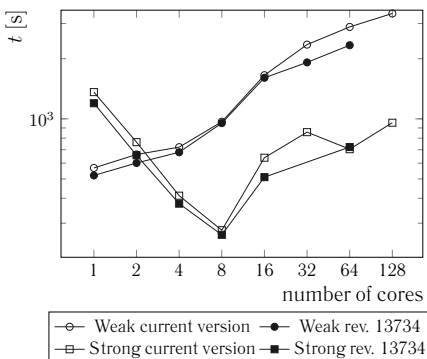


Figure 6.15: Comparisons between the current version and revision 13734 of the code.

for the sharp rise of the timing due the auxiliary mesh in the current version. The timings don't remain constant as would be ideal but instead rise. This is no surprise with all communication that is needed to synchronize fields and particles.

Finally in Fig. 6.15 we compare the overall timings for both revisions and for weak and strong scaling. Revision 13734 seems to be better for both tests except for the fact that we could not scale it up to 128 cores. It seems to be very questionable whether the approach with an auxiliary mesh should be pursued further. We expect that it could be optimized further since it has been added recently. In conjunction with a sub-gridding scheme such as in [130, 131] further optimization on the approach could be worthwhile.

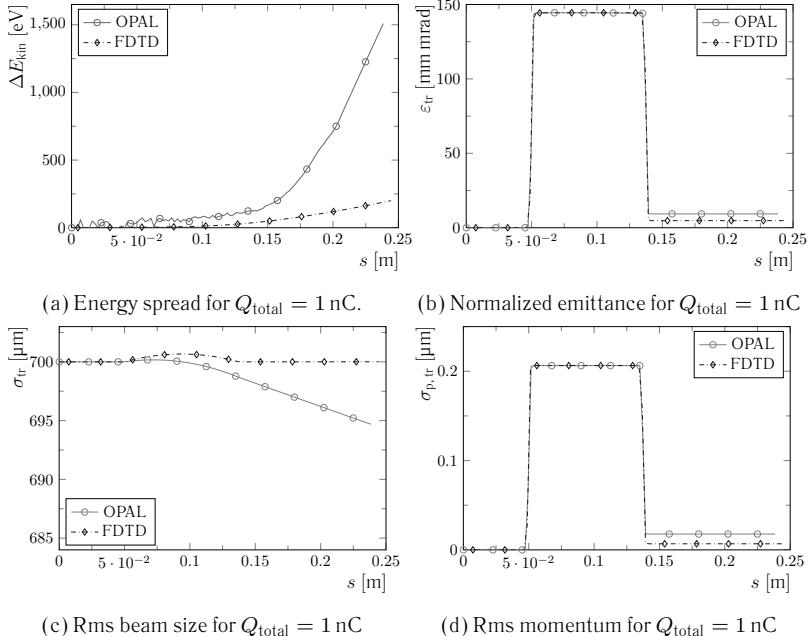


Figure 6.16: Comparison between OPAL and the FDTD code at $E_{\text{kin}} = 150 \text{ MeV}$

6.3 Application to Simple Bend

Although our FDTD code is 2-dimensional and therefore shows inherently different physics than a 3-dimensional code we compare results to results generated with *OPAL* [44]. For a first comparison we used the same parameters as in Table 6.1 with the exception of the total charge which we set to $Q_{\text{tot}} = 1 \text{ nC}$ to get a stronger effect of synchrotron radiation. We let both codes run for 2500 steps which results in a drift of approximately 0.1 m after the bend. The bend has a rectangular shape with parallel entry and exit edges. The orientation of the bend is such that the normal for both the entry and the exit edges form an angle of half of the total deflection with the path of the incoming respectively the outgoing particles. The magnetic field at the edges is set to have an abrupt transition, the change from outside to the inside of the bend is not smooth.

The root mean square of the kinetic energies, the normalized transverse emittance, the root mean square of the transverse particle positions and the root mean square of the transverse momenta are shown in Fig. 6.16a-d. The coordinate system of rms particle positions, rms momenta and normalized emittance are in the beam coordinate system which OPAL uses. This coordinate system has its z -axis parallel to the direction of the mean momentum and the y -axis is here parallel to the normal of the plane in which the mean position propagates. With transverse we mean the x -axis in this beam coordinate system and σ_{tr} means the rms of the transverse positions.

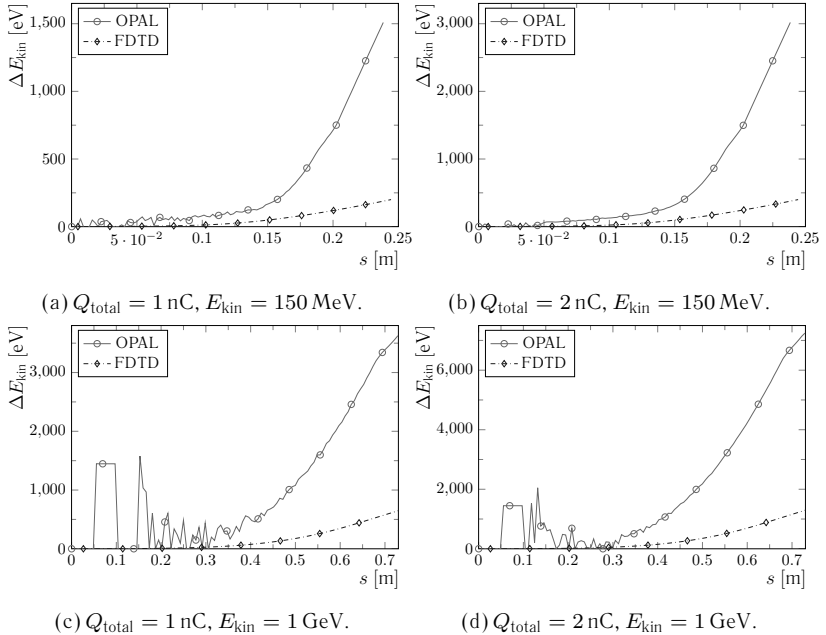


Figure 6.17: Comparison of the energy spread between OPAL and the FDTD code at different kinetic energies and for different total charges.

The obvious differences are in the energy spread Fig. 6.16a and in the beam size Fig. 6.16c. However the results for the normalized emittance Fig. 6.16b and for the rms of the momenta Fig. 6.16d match fairly well.

The beam in OPAL focuses weakly after the bend. With hard edge rectangular bends we expect that the beam is not focused. We attribute this difference to the far simpler implementation for the bend in the FDTD code where the possibility to have a smoothly changing magnetic field is not yet implemented.

The difference in the rms of the kinetic energy is possibly caused by the reduction from 3-dimensional to a 2-dimensional space. The 2-dimensional FDTD code clearly underestimates the action of the synchrotron radiation. We have seen in Section 6.1 that the results for the two 2-dimensional codes are consistent.

We get a similar result if we increase the total current while keeping all the other parameters. In Fig. 6.17a we show again the case with total charge 1 nC while in Fig. 6.17b the total charge is 2 nC. By doubling the total charge also the energy spread doubles approximately. This is valid for OPAL as well as for the FDTD code.

For Fig. 6.17c and d we increased the kinetic energy to 1 GeV. We kept the magnetic field strength and also the bend angle the same. This leads to a longer radius and a longer bend. In Fig. 6.17c the total charge is at 1 nC while in Fig. 6.17d it is doubled again. The two codes show a similar behavior at higher energies as at the lower energies.

Chapter Seven

Conclusions

In this thesis we worked towards a 3-dimensional self-consistent code for the simulation of magnetic chicanes in particle accelerators. The code should not restrict the number of particles that can be included nor the shape of the particle distribution. Although this goal was far-fetched we laid a good basis for further research towards this goal. For this we developed a self-consistent 2-dimensional finite-difference code.

We have chosen the finite-difference method with regular meshes for their simplicity, their wide usage and the large knowledge base. We first delved into an Alternating Direction Implicit scheme for Maxwell's equations with the property of divergence preservation [99]. Divergence preservation is important if one combines simulations of charged particles with simulations of electromagnetic fields. We developed a fully parallel code and we adapted the Perfectly Matched Layer method for the update scheme [112]. The performance of this adapted method has been compared to the results with the Yee scheme for time steps that are shorter than the Courant-Friedrichs-Lowy limit. We could show that the reflections were as low as for the Yee scheme.

Since the ADI method is not bound by the CFL condition but only by the accuracy requirement of the application one can also choose larger time steps. It has then been shown that the presented PML method also shows good results for large time steps compared to the PML implementation for an ADI method that does not preserve the divergence.

Although this new ADI method does preserve the divergence it also has a major drawback for our purpose. It shows dispersion in all space directions. This is no constraint for particles

that move slower than the waves with the highest frequency that are expected in a simulation. For our goal this poses an obstacle that is too severe. Electrons at a kinetic energy of 150 MeV have a speed that is only approximately 0.006 % and at 1 GeV the speed is only approximately 0.0001 % below the speed of light. We then changed the update scheme to a TE/TM scheme [55] which does both preserve the divergence and that has one direction for which the dispersion vanishes.

We then implemented a code that is based on Liénard-Wiechert potentials to validate results produced by the FDTD code. The charge in the Liénard-Wiechert code is not based on particles but on meshes to reduce the computational cost. Furthermore this Liénard-Wiechert approach is not self-consistent. Instead the path of the centroid of charge distribution is preassigned. Nevertheless we could show good agreement with the results of the FDTD code and hereby affirm the correctness.

Apart from validating the results of the FDTD code the Liénard-Wiechert method also has the benefit to distinguish the velocity field from the acceleration field. An adaption to three dimensions should not pose large problems. The computational cost for one time step will of course increase with the number of grid cells in the vertical dimension. Though it should be easy to scale to more cores since the model is not self-consistent and therefore has only few points in the algorithm where the cores have to be synchronized.

We also investigated different parallelization schemes for both the fields and the particles. Here the difficulty is that the particles in an accelerator are very localized while the surrounding structure is large. The update of the positions and momenta of the particles as well as the calculation of the currents are among the most compute intensive parts. Big imbalances occur if the particles are distributed only among a few cores. Thus the particles should be distributed as evenly as possible among the cores. The particles have to be updated with the fields at their positions since we intend to develop a self-consistent code. Likewise the fields have to be updated with the current density at the positions of the particles.

We then compared the performance of two different implementations for the parallelization. On one hand we showed the performance of a scheme where the particles are distributed evenly. Also the fields are distributed evenly. Thus the fields at position of the particles are at any time only updated by a few cores. The fields in the region of the particles are then sent by those few cores to all other cores in order for them to update the particles. All cores then send back the current density of their particles.

The second parallelization scheme uses an auxiliary mesh with the same cell dimensions as the main mesh. This auxiliary mesh is large enough and is moved such that it always contains all particles and that they are approximately centered in it. The mesh is shifted in steps of whole cells in order to have co-located sampling points with the main mesh.

We showed that the overhead caused by the auxiliary mesh outweighs the possible advantage of this approach. The overhead is composed by the need to synchronize the auxiliary mesh with the main mesh and by the disadvantageous ratio between the size of the patch of field that every core owns to the circumference of this patch. We concluded that this approach could still be of interest if one intends to implement a multigrid method with a coarser main mesh. Then one has to filter waves that fit into the fine auxiliary mesh but that can not be resolved sufficiently on the main mesh [130, 131].

Finally we compared results of the FDTD code with results from OPAL which uses an implementation of the 1-dimensional wake function for the coherent synchrotron radiation.

This wake function is based on analytic results for two particles propagating on the same bent path. In OPAL this wake function is applied both for situation when the particle bunch is inside the bend as well when it drifts on the adjacent straight section. It came to no surprise that the results for the root mean square of the kinetic energy differ considerably. In the 2-dimensional approach where we simulate line charges that stretch to infinity both above and below the plane. The electric field that this line charges generate falls off as $1/r$ with distance r to the line. For 3-dimensional point-like sources in contrast the field falls off as $1/r^2$.

Outlook

In the following we give some topics into which one could investigate further in order to achieve finally the goal of a 3-dimensional self-consistent code for the simulation of magnetic chicanes in particle accelerators.

Parallelization The current state offers a good basis for further optimization of the parallelization. This involves possibly also further work on the library IPPL to increase the flexibility.

Mesh refinement For the simulation of the magnetic chicane one is only interested in the interaction of the charged particles with the electromagnetic field they induce themselves. Though the interaction only happens at the location of the particles. On the other hand the surrounding mesh which is the larger part of a domain is needed for the feedback of the boundaries. One should therefore invest research into mesh refinement techniques that absorb high frequency portions of the radiation.

Moving main mesh To further reduce the number of mesh cells one could have at any time only parts of the whole domain loaded in memory. Distances in the longitudinal direction are strongly stretched from the perspective of the particles due to their high kinetic energy and relativistic length contraction. Thus simulating only small parts in front and behind the particles instead of the whole domain yields the same results. New parts of the domain should be loaded in front of the particles as they move and old parts should be dropped. The challenge here is that no reflection occurs.

Body fitted mesh Another method to reduce the number of mesh cells is to use a body fitted mesh. For this one should first research how update schemes for Maxwell's equation with low numerical dispersion have to be adapted. In particular one has to research how numerical dispersion behave in this adaption.

Liénard-Wiechert potentials in 3D The presented Liénard-Wiechert potential method is easily extendable to three dimensions. It can be a valuable tool for the validation of results and visualization. The necessary work and validation with the 1-dimensional approach could be subject of a semester thesis.

Appendices

A.1 Dispersion Relation of Divergence Preserving ADI

Following the approach in [87, 94] we apply the four operators of [99] to the plane wave \mathbf{F} and find

$$\begin{aligned} \left(\mathbb{1} + \frac{1}{2}\mathcal{P}\right)\mathbf{F} &= \mathcal{Z} \begin{pmatrix} \mathbb{1} & \mathcal{A} \\ \mathcal{A}^\intercal & \mathbb{1} \end{pmatrix} \mathcal{Z}^{-1} \mathbf{F} = \Lambda_{(\mathbb{1} + \frac{1}{2}\mathcal{P})} \mathbf{F}, \\ \left(\mathbb{1} - \frac{1}{2}\mathcal{P}\right)^{-1} \mathbf{F} &= \mathcal{Z} \begin{pmatrix} \mathcal{A} & \mathbb{1} \\ \mathbb{1} & \mathcal{A}^\intercal \end{pmatrix} \mathcal{K}\mathcal{R}\mathcal{Z}^{-1} \mathbf{F} = \Lambda_{(\mathbb{1} - \frac{1}{2}\mathcal{P})^{-1}} \mathbf{F}, \\ \left(\mathbb{1} + \frac{1}{2}\mathcal{M}\right) \mathbf{F} &= \mathcal{Z} \begin{pmatrix} \mathbb{1} & \mathcal{A}^\intercal \\ \mathcal{A} & \mathbb{1} \end{pmatrix} \mathcal{Z}^{-1} \mathbf{F} = \Lambda_{(\mathbb{1} + \frac{1}{2}\mathcal{M})} \mathbf{F}, \\ \left(\mathbb{1} - \frac{1}{2}\mathcal{M}\right)^{-1} \mathbf{F} &= \mathcal{Z} \begin{pmatrix} \mathcal{A}^\intercal & \mathbb{1} \\ \mathbb{1} & \mathcal{A} \end{pmatrix} \mathcal{R}\mathcal{K}\mathcal{Z}^{-1} \mathbf{F} = \Lambda_{(\mathbb{1} - \frac{1}{2}\mathcal{M})^{-1}} \mathbf{F} \end{aligned}$$

where

$$\begin{aligned}\mathcal{A} &= \begin{pmatrix} 0 & 0 & \mathbb{i}\Sigma_y^{1/2} \\ \mathbb{i}\Sigma_z^{1/2} & 0 & 0 \\ 0 & \mathbb{i}\Sigma_x^{1/2} & 0 \end{pmatrix}, & \mathcal{Z} &= \begin{pmatrix} Z_0^{1/2} \mathbb{1}_{3 \times 3} & 0 \\ 0 & Z_0^{-1/2} \mathbb{1}_{3 \times 3} \end{pmatrix}, \\ \mathcal{K} &= \begin{pmatrix} \mathcal{G} & \\ & \mathcal{E} \end{pmatrix}, & \mathcal{R} &= \begin{pmatrix} 0 & \mathbb{1}_{3 \times 3} \\ \mathbb{1}_{3 \times 3} & 0 \end{pmatrix}, \\ \mathcal{E} &= (\mathbb{1}_{3 \times 3} - \mathcal{A}\mathcal{A}^\top)^{-1}, & \mathcal{G} &= (\mathbb{1}_{3 \times 3} - \mathcal{A}^\top\mathcal{A})^{-1}, \\ \Sigma_\nu &= \left(\eta_\nu \sin \left(\frac{k_\nu \Delta \nu}{2} \right) \right)^2. \end{aligned}$$

Both \mathcal{E} and \mathcal{G} are diagonal matrices.

The dispersion relation of the original ADI scheme [87] is then given by

$$\det \left(e^{i\omega \Delta t} - \Lambda_{(\mathbb{1} + \frac{1}{2}\mathcal{M})} \Lambda_{(\mathbb{1} - \frac{1}{2}\mathcal{P})}^{-1} \Lambda_{(\mathbb{1} + \frac{1}{2}\mathcal{P})} \Lambda_{(\mathbb{1} - \frac{1}{2}\mathcal{M})}^{-1} \right),$$

whereas for the divergence preserving ADI scheme [99] it is given by

$$\det \left(e^{i\omega \Delta t} - \Lambda_{(\mathbb{1} - \frac{1}{2}\mathcal{M})}^{-1} \Lambda_{(\mathbb{1} + \frac{1}{2}\mathcal{P})} \Lambda_{(\mathbb{1} - \frac{1}{2}\mathcal{P})}^{-1} \Lambda_{(\mathbb{1} + \frac{1}{2}\mathcal{M})} \right).$$

Since

$$\mathcal{E}^{-1}\mathcal{A} = \mathcal{A}\mathcal{G}^{-1},$$

and

$$\begin{aligned}\Lambda_{(\mathbb{1} + \frac{1}{2}\mathcal{P})} &= \mathcal{Z}\mathcal{R}\mathcal{K}^{-1}\mathcal{R}\mathcal{Z}^{-1} & \Lambda_{(\mathbb{1} - \frac{1}{2}\mathcal{P})}^{-1} &= \Lambda_{(\mathbb{1} - \frac{1}{2}\mathcal{P})}^{-1} & \mathcal{Z}\mathcal{R}\mathcal{K}^{-1}\mathcal{R}\mathcal{Z}^{-1}, \\ \Lambda_{(\mathbb{1} - \frac{1}{2}\mathcal{P})}^{-1} &= \mathcal{Z}\mathcal{R}\mathcal{K}\mathcal{R}\mathcal{Z}^{-1} & \Lambda_{(\mathbb{1} + \frac{1}{2}\mathcal{P})} &= \Lambda_{(\mathbb{1} + \frac{1}{2}\mathcal{P})} & \mathcal{Z}\mathcal{R}\mathcal{K}\mathcal{R}\mathcal{Z}^{-1}, \\ \Lambda_{(\mathbb{1} + \frac{1}{2}\mathcal{M})} &= \mathcal{Z}\mathcal{K}^{-1}\mathcal{Z}^{-1} & \Lambda_{(\mathbb{1} - \frac{1}{2}\mathcal{M})}^{-1} &= \Lambda_{(\mathbb{1} - \frac{1}{2}\mathcal{M})}^{-1} & \mathcal{Z}\mathcal{K}^{-1}\mathcal{Z}^{-1}, \\ \Lambda_{(\mathbb{1} - \frac{1}{2}\mathcal{M})}^{-1} &= \mathcal{Z}\mathcal{K}\mathcal{Z}^{-1} & \Lambda_{(\mathbb{1} + \frac{1}{2}\mathcal{M})} &= \Lambda_{(\mathbb{1} + \frac{1}{2}\mathcal{M})} & \mathcal{Z}\mathcal{K}\mathcal{Z}^{-1}, \end{aligned}$$

we find

$$\begin{aligned}&\det \left(e^{i\omega \Delta t} - \Lambda_{(\mathbb{1} + \frac{1}{2}\mathcal{M})} \Lambda_{(\mathbb{1} - \frac{1}{2}\mathcal{P})}^{-1} \Lambda_{(\mathbb{1} + \frac{1}{2}\mathcal{P})} \Lambda_{(\mathbb{1} - \frac{1}{2}\mathcal{M})}^{-1} \right) \\ &= \det \left(\mathcal{Z}\mathcal{K}^{-1}\mathcal{Z}^{-1} \left(e^{i\omega \Delta t} - \Lambda_{(\mathbb{1} - \frac{1}{2}\mathcal{M})}^{-1} \Lambda_{(\mathbb{1} + \frac{1}{2}\mathcal{P})} \Lambda_{(\mathbb{1} - \frac{1}{2}\mathcal{P})}^{-1} \Lambda_{(\mathbb{1} + \frac{1}{2}\mathcal{M})} \right) \mathcal{Z}\mathcal{K}\mathcal{Z}^{-1} \right) \\ &= \det \left(e^{i\omega \Delta t} - \Lambda_{(\mathbb{1} - \frac{1}{2}\mathcal{M})}^{-1} \Lambda_{(\mathbb{1} + \frac{1}{2}\mathcal{P})} \Lambda_{(\mathbb{1} - \frac{1}{2}\mathcal{P})}^{-1} \Lambda_{(\mathbb{1} + \frac{1}{2}\mathcal{M})} \right). \end{aligned}$$

□

Thus the divergence preserving ADI scheme exhibits the same dispersion relation as the original ADI scheme, see (4.11) on page 54.

A.2 Installation

First check the FDTD code out:

```
git clone https://github.com/kreischtauf/CSRST.git
```

For the installation of the FDTD code you have to install the following libraries:

Name	Version	Notes
Boost	1.48.0	MPI, Regex, Serialization, System, Timer needed
GSL	≥ 1.16	
ScaLAPACK		
LAPACK		
SuperLU_DIST	3.0	here
METIS	5.0.2	here
PARMETIS	4.0.2	here
Trilinos	1.8.3	Amesos, AztecOO, Aztecoo-Teuchos, Belos, Epetra, EpetraExt, Ifpack, Isorropia, Isorropia- Epetraext, ML, Teuchos, Teuchos-Extended needed
HDF5	1.8.9	
SZip		
TCLAP	1.2.1	
H5Hut	1.99.7	here
IPPL	rev. 13577	here

For the libraries Trilinos, TCLAP, H5Hut and IPPL a detailed instruction is given below since you have to apply patches. You find these patches in the directory *CSRST/tools/*.

Trilinos

```
wget http://trilinos.org/oldsite/download/files/trilinos-10.8.3-Source.tar.gz
tar zxf trilinos-10.8.3-Source.tar.gz
patch -p1 < tools/trilinos-10.8.3.patch
```

A template for the build of Trilinos can be found in the directory *CSRST/tools/*.

TCLAP

```
wget -O tclap-1.2.1.tar.gz http://goo.gl/9PX3Hw
tar zxf tclap-1.2.1.tar.gz
patch -p1 < tools/tclap-1.2.1.patch
```

H5hut

```
svn co svn+ssh://savannah01.psi.ch/repos/H5hut/src/tags/1.99.7 H5hut-1.99.7
patch -p1 < tools/H5hut-1.99.7.patch
```

IPPL

```
svn co -r 13577 svn+ssh://savannah01.psi.ch/repos/ipll/src/trunk ippl-edge  
patch -p1 < tools/ipll-r13577.patch
```

After building all the libraries you can build the FDTD code. A cmake template for this can be found in the directory *CSRST/tools/*.

For the installation of the Liénard–Wiechert application check out the code

```
git clone https://github.com/kreischtauf/LiWiPot.git
```

A cmake template for the build can be found in the directory *LiWiPot/tools/*.

A.3 Run Examples

The call,

```
mkdir Data  
mpirun -np 4 csrst --commlib mpi --debug 5 --info 5 --length 1.0 --width 0.2 --phi  
5.0 --Ekin 150.0 --Bz 0.502 --mean_Rx 0.05 --mean_Ry 0.1 --sigma_x 0.0007  
--sigma_p 0 --Qtotal 1.0 --Np 10000000 -N 2500 -x 12200 -y 740 --plotmodulus  
500 --reballance 100000 --linemodulus 200 --statmodulus 1,
```

will cause the FDTD code to run a simulation of a particle bunch with 10 million particles for 2500 steps. The domain has a straight section of 0.1 m before (default) and of 1 m after the bend. The vacuum pipe has a width of 0.2 m. The particles have a kinetic energy of 150 MeV and have initially a mean position $x = 0.05$ m, $y = 0.1$ m. They have a Gaussian distribution with a standard deviation of 0.7 mm. Their total charge is 1 nC. The particles are deflected by 5° by a magnetic field of 0.502 T. The mesh has 12 200 cells in the longitudinal direction and 740 cells in the transverse direction. Binary VTK files are written every 500 steps, the electric field along a line is written every 200 steps and the particle statistics is computed and written to disc every step.

The call

```
mpirun -np 4 lw -commlib mpi --debug 5 --info 5 -w 0.2 -n 2 -N 128 -Q 1 --sigma_x  
0.0007 --Ekin 150.0 --Bz 0.50205 -p 5.000 -t 0.097 -t 893 -v -x 0.0001 -y 0.0004
```

will cause the Liénard-Wiechert application to compute the electric field of a Gaussian charge distribution with a total charge of 1 nC and a standard deviation, σ , of 0.7 mm. The field will be computed on a mesh with mesh cell of length 0.1 mm and a width of 0.4 mm. The total mesh length and width is 8σ . The mean position of the charge distribution is at 5° and 0.097 m after the bend, see Fig. 6.3. For the contribution due to the infinitely long drift in front of the bend 128 image charges are considered on either side of the domain, while for the remainig path only two image charges are considered. This low number of image charges in the latter case is justified by the fact that contributions due to image charges further away can't reach the vicinity of the bunch yet. The bend is split into 893 straight sections and the walls of the vacuum pipe are 0.2 m apart. The computed field is stored in a binary VTK file ‘*result_phi=5.00_L=0.10.pvt*’ and the electric field along a line is stored in a simple ASCII file ‘*FieldOnLine_phi=5.00_L=0.10.dat*’.

A Python script for the visualization of the VTK files using Visit can be checked out from the git repository:

```
git clone https://github.com/kreischtauf/CSRST.git
```

The script is used with Visit in command-line mode:

```
visit -cli -s tools/visualizeSim.py 'c_* .pvt'
```


Bibliography

- [1] A. Einstein, “Zur Elektrodynamik bewegter Körper”, Annalen der Physik **322**, 891–921 (1905).
[doi:10.1002/andp.19053221004](https://doi.org/10.1002/andp.19053221004).
- [2] D. H. Frisch and J. H. Smith, “Measurement of the Relativistic Time Dilation Using μ -Mesons”, Am. J. Phys. **31**, 342–355 (1963).
[doi:10.1119/1.1969508](https://doi.org/10.1119/1.1969508).
- [3] J. D. Jackson, “Classical Electrodynamics”, 3rd ed. (John Wiley & Sons Inc, Hoboken, NJ, 1999), ISBN: 0-471-30932-X.
- [4] S. G. Arutyunyan, “Electromagnetic field lines of a point charge moving arbitrarily in vacuum”, Soviet Physics Uspekhi **29**, 1053–1057 (1986).
[doi:10.1070/PU1986v029n11ABEH003539](https://doi.org/10.1070/PU1986v029n11ABEH003539).
- [5] T. Shintake, “Real-time animation of synchrotron radiation”, Nucl. Instrum. Methods Phys. Res. Sect. A **507**, 89–92 (2003).
[doi:10.1016/S0168-9002\(03\)00844-1](https://doi.org/10.1016/S0168-9002(03)00844-1).
- [6] H. Wiedemann, “Particle Accelerator Physics”, 3rd ed. (Springer, Berlin Heidelberg New York, 2007), ISBN: 978-3-540-49043-2.

- [7] M. Abraham, "Prinzipien der Dynamik des Elektrons", Annalen der Physik **315**, 105–179 (1902).
[doi:10.1002/andp.19023150105](https://doi.org/10.1002/andp.19023150105).
- [8] P. A. M. Dirac, "Classical Theory of Radiating Electrons", Royal Society of London Proceedings Series A **167**, 148–169 (1938).
[doi:10.1098/rspa.1938.0124](https://doi.org/10.1098/rspa.1938.0124).
- [9] D. Ivanenko and A. Sokolov, "The theory of the 'luminescent' electron", Doklady Akademii Nauk S.S.S.R. **59**, 1551 (1948).
- [10] J. Schwinger, "On the Classical Radiation of Accelerated Electrons", Phys. Rev. **75**, 1912–1925 (1949).
[doi:10.1103/PhysRev.75.1912](https://doi.org/10.1103/PhysRev.75.1912).
- [11] J. Schwinger, "On Radiation by Electrons in a Betatron", LBNL-39088, transcribed by M. A. Furman (1945).
- [12] W. A. Barletta et al., "Free electron lasers: Present status and future challenges", Nucl. Instrum. Methods Phys. Res. Sect. A **618**, 69–96 (2010).
[doi:10.1016/j.nima.2010.02.274](https://doi.org/10.1016/j.nima.2010.02.274).
- [13] A. M. Kondratenko and E. L. Saldin, "Generation of Coherent Radiation by a Relativistic Electron Beam in an Ondulator", Part. Accel. **10**, 207–216 (1980).
- [14] D. M. Mills et al., "Report of the Working Group on Synchrotron Radiation Nomenclature -- brightness, spectral brightness or brilliance?", J. Synchrotron Rad. **12**, 385 (2005).
[doi:10.1107/S090904950500796X](https://doi.org/10.1107/S090904950500796X).
- [15] H. H. Braun et al., "Emittance growth and energy loss due to coherent synchrotron radiation in a bunch compressor", Phys. Rev. ST Accel. Beams **3**, 124402 (2000).
[doi:10.1103/PhysRevSTAB.3.124402](https://doi.org/10.1103/PhysRevSTAB.3.124402).
- [16] G. Stupakov and S. Heifets, "Beam instability and microbunching due to coherent synchrotron radiation", tech. rep. SLAC-PUB-8761 (2001).
- [17] P. Emma and R. Brinkmann, "Emittance Dilution Through Coherent Energy Spread Generation in Bending Systems", tech. rep. SLAC-PUB-7554 (1997).
- [18] M. Borland, "Design and performance simulations of the bunch compressor for the Advanced Photon Source Low-Energy Undulator Test Line free-electron laser", Phys. Rev. ST Accel. Beams **4**, 074201 (2001).
[doi:10.1103/PhysRevSTAB.4.074201](https://doi.org/10.1103/PhysRevSTAB.4.074201).
- [19] F. Stulle, "A Bunch Compressor for small Emittances and high Peak Currents at the VUV Free-Electron Laser", PhD thesis (University of Hamburg, 2004).
- [20] E. L. Saldin, E. A. Schniedmiller and M. V. Yurkov, "Longitudinal space charge-driven microbunching instability in the TESLA Test Facility linac", Nucl. Instrum. Methods Phys. Res. Sect. A **528**, 355–359 (2004).
[doi:10.1016/j.nima.2004.04.067](https://doi.org/10.1016/j.nima.2004.04.067).

- [21] S. Seletskiy et al., “Initial source of microbunching instability studies in a free electron laser injector”, *Phys. Rev. ST Accel. Beams* **14**, 110701 (2011).
[doi:10.1103/PhysRevSTAB.14.110701](https://doi.org/10.1103/PhysRevSTAB.14.110701).
- [22] S. Wesch and B. Schmidt, “Summary of COTR Effects”, in Proceedings of DIPAC, WEOA01, 539–543 (2011).
<http://accelconf.web.cern.ch/AccelConf/DIPAC2011/papers/weoa01.pdf>.
- [23] Z. Huang et al., “Suppression of microbunching instability in the linac coherent light source”, *Phys. Rev. ST Accel. Beams* **7**, 074401 (2004).
[doi:10.1103/PhysRevSTAB.7.074401](https://doi.org/10.1103/PhysRevSTAB.7.074401).
- [24] T. Shaftan and Z. Huang, “Experimental characterization of a space charge induced modulation in high-brightness electron beam”, *Phys. Rev. ST Accel. Beams* **7**, 080702 (2004).
[doi:10.1103/PhysRevSTAB.7.080702](https://doi.org/10.1103/PhysRevSTAB.7.080702).
- [25] R. Ganter et al., “SwissFEL Conceptual Design Report”, tech. rep. PSI Bericht Nr. 10-04 (2010).
- [26] K. L. Brown, “A First- and Second-Order Matrix Theory for the Design of Beam Transport Systems and Charged Particle Spectrometers”, tech. rep. SLAC-R-75 (1968).
- [27] R. W. Hockney and J. W. Eastwood, “Computer Simulation Using Particles”, special student ed. (Adam Hilger, Bristol, 1988), ISBN: 0-85274-392-0.
- [28] J. Qiang and R. D. Ryne, “Parallel 3D Poisson solver for a charged beam in a conducting pipe”, *Comput. Phys. Commun.* **138**, 18–28 (2001).
[doi:10.1016/S0010-4655\(01\)00185-0](https://doi.org/10.1016/S0010-4655(01)00185-0).
- [29] G. Pöplau and U. van Rienen, “A Self-Adaptive Multigrid Technique for 3-D Space Charge Calculations”, *IEEE Trans. Magn.* **44**, 1242–1245 (2008).
[doi:10.1109/TMAG.2007.914831](https://doi.org/10.1109/TMAG.2007.914831).
- [30] A. Adelmann, P. Arbenz and Y. Ineichen, “A fast parallel Poisson solver on irregular domains applied to beam dynamics simulations”, *J. Comput. Phys.* **229**, 4554–4566 (2010).
[doi:10.1016/j.jcp.2010.02.022](https://doi.org/10.1016/j.jcp.2010.02.022).
- [31] G. A. Schott, “Electromagnetic Radiation” (Cambridge University Press, 1912).
- [32] J. B. Murphy, S. Krinsky and R. L. Gluckstern, “Longitudinal Wakefield for an Electron Moving on a Circular Orbit”, *Particle Accelerators* **57**, 9–64 (1997).
- [33] J. S. Nodwick and D. S. Saxon, “Suppression of Coherent Radiation by Electrons in a Synchrotron”, *Phys. Rev.* **96**, 180–184 (1954).
[doi:10.1103/PhysRev.96.180](https://doi.org/10.1103/PhysRev.96.180).
- [34] E. L. Saldin, E. A. Schneidmiller and M. V. Yurkov, “On the Coherent Radiation of an Electron Bunch Moving in an Arc of a Circle”, *Nucl. Instrum. Methods Phys. Res. Sect. A* **398**, 373–394 (1997).
[doi:10.1016/S0168-9002\(97\)00822-X](https://doi.org/10.1016/S0168-9002(97)00822-X).

- [35] C. Mayes and G. Hoffstaetter, “Exact 1D model for coherent synchrotron radiation with shielding and bunch compression”, Phys. Rev. ST Accel. Beams **12**, 024401 (2009).
[doi:10.1103/PhysRevSTAB.12.024401](https://doi.org/10.1103/PhysRevSTAB.12.024401).
- [36] D. Sagan et al., “Extended one-dimensional method for coherent synchrotron radiation including shielding”, Phys. Rev. ST Accel. Beams **12**, 040703 (2009).
[doi:10.1103/PhysRevSTAB.12.040703](https://doi.org/10.1103/PhysRevSTAB.12.040703).
- [37] R. D. Ryne et al., “A Model for One-Dimensional Coherent Synchrotron Radiation including Short-Range Effects”, ArXiv, 1202.2409 (2012).
<http://arxiv.org/abs/1202.2409>.
- [38] G. Bassi et al., “Overview of CSR codes”, Nucl. Instrum. Methods Phys. Res. Sect. A **557**, 189–204 (2006).
[doi:10.1016/j.nima.2005.10.067](https://doi.org/10.1016/j.nima.2005.10.067).
- [39] M. Borland, “Elegant: a flexible SDDS-compliant code for accelerator simulation”, tech. rep. LS-287 (2000).
- [40] M. Borland, “Simple method for particle tracking with coherent synchrotron radiation”, Phys. Rev. ST Accel. Beams **4**, 070701 (2001).
[doi:10.1103/PhysRevSTAB.4.070701](https://doi.org/10.1103/PhysRevSTAB.4.070701).
- [41] B. E. C. Koltenbah et al., “PARMELA_B: a new version of PARMELA with coherent synchrotron radiation effects and a finite difference space charge routine”, Nucl. Instrum. Methods Phys. Res. Sect. A **487**, 249–267 (2002).
[doi:10.1016/S0168-9002\(01\)02174-X](https://doi.org/10.1016/S0168-9002(01)02174-X).
- [42] K. Flöttmann, “ASTRA, A Space Charge Tracking Algorithm”, version 3.0, DESY (2011).
<http://www.desy.de/~mpyflo/>.
- [43] J. Qiang et al., “Three-dimensional quasistatic model for high brightness beam dynamics simulation”, Phys. Rev. ST Accel. Beams **9**, 044204 (2006).
[doi:10.1103/PhysRevSTAB.9.044204](https://doi.org/10.1103/PhysRevSTAB.9.044204).
- [44] A. Adelmann et al., “The Object Oriented Parallel Accelerator Library (OPAL), Design, Implementation and Application”, in Proceedings of ICAP, we3iopk01 (2009).
<http://accelconf.web.cern.ch/AccelConf/ICAP2009/papers/we3iopk01.pdf>.
- [45] C. K. Birdsall and A. B. Langdon, “Plasma physics via computer simulation” (McGraw-Hill, New York, 1985), ISBN: 0-07-005371-5.
- [46] D. Sagan, “Bmad: A relativistic charged particle simulation library”, Nucl. Instrum. Methods Phys. Res. Sect. A **558**, 356–359 (2006).
[doi:10.1016/j.nima.2005.11.001](https://doi.org/10.1016/j.nima.2005.11.001).
- [47] M. Dohlus, A. Kabel and T. Limberg, “Efficient field calculation of 3D bunches on general trajectories”, Nucl. Instrum. Methods Phys. Res. Sect. A **445**, 338–342 (2000).
[doi:10.1016/S0168-9002\(00\)00139-X](https://doi.org/10.1016/S0168-9002(00)00139-X).

- [48] R. Li, “Self-consistent simulation of the CSR effect on beam emittance”, Nucl. Instrum. Methods Phys. Res. Sect. A **429**, 310–314 (1999).
[doi:10.1016/S0168-9002\(99\)00135-7](https://doi.org/10.1016/S0168-9002(99)00135-7).
- [49] B. Terzić and R. Li, “New Particle-In-Cell Code for Numerical Simulation of Coherent Synchrotron Radiation”, in Proceedings of IPAC, tupec084 (2010).
<http://accelconf.web.cern.ch/AccelConf/IPAC10/papers/tupec084.pdf>.
- [50] T. Agoh and K. Yokoya, “Calculation of coherent synchrotron radiation using mesh”, Phys. Rev. ST Accel. Beams **7**, 054403 (2004).
[doi:10.1103/PhysRevSTAB.7.054403](https://doi.org/10.1103/PhysRevSTAB.7.054403).
- [51] R. Warnock, G. Bassi and J. A. Ellison, “Vlasov treatment of coherent synchrotron radiation from arbitrary planar orbits”, Nucl. Instrum. Methods Phys. Res. Sect. A **558**, 85–89 (2006).
[doi:10.1016/j.nima.2005.11.070](https://doi.org/10.1016/j.nima.2005.11.070).
- [52] J. J. Dongarra et al., “LINPACK Users’ Guide” (SIAM, 1980), ISBN: 0-89871-172-X.
- [53] H. Meuer et al., *TOP500 Supercomputing Sites*, (Feb. 17, 2014)
<http://www.top500.org>.
- [54] A. Adelmann and Y. Ineichen, “The IP²L Framework”, tech. rep. PSI-PR-09-05 (2009).
http://amas.web.psi.ch/docs/ipp1-doc/ipp1_user_guide.pdf.
- [55] M. Dohlus and I. Zagorodnov, “Explicit TE/TM scheme for particle beam simulations”, J. Comput. Phys. **228**, 2822–2833 (2009).
[doi:10.1016/j.jcp.2008.12.023](https://doi.org/10.1016/j.jcp.2008.12.023).
- [56] K. S. Yee, “Numerical Solutions of Initial Boundary Value Problems Involving Maxwell’s Equations in Isotropic Media”, IEEE Trans. Antennas Propag. **14**, 302–307 (1966).
[doi:10.1109/TAP.1966.1138693](https://doi.org/10.1109/TAP.1966.1138693).
- [57] R. Barthelmé, “Conservation de la charge dans les codes PIC”, C. R. Acad. Sci. Paris, Ser. I **341**, 689–694 (2005).
[doi:10.1016/j.crma.2005.09.008](https://doi.org/10.1016/j.crma.2005.09.008).
- [58] G. Deschamps, “Electromagnetics and differential forms”, Proc. IEEE **69**, 676–696 (1981).
[doi:10.1109/PROC.1981.12048](https://doi.org/10.1109/PROC.1981.12048).
- [59] A. Bossavit, “Whitney forms: a class of finite elements for three-dimensional computations in electromagnetism”, IEE Proc. A **135**, 493–500 (1988).
[doi:10.1049/ip-a-1.1988.0077](https://doi.org/10.1049/ip-a-1.1988.0077).
- [60] W. H. Press et al., “Numerical Recipes in C: the Art of Scientific Computing”, 2nd ed. (Cambridge University Press, Cambridge, New York, Port Chester, Melbourne, Sydney, 1992), ISBN: 0-521-43108-5.

- [61] F. Mackay, R. Marchand and K. Kabin, “Divergence-free magnetic field interpolation and charged particle trajectory integration”, *J. Geophys. Res. Space Phys.* **111**, A06205 (2006).
[doi:10.1029/2005JA011382](https://doi.org/10.1029/2005JA011382).
- [62] G. Tóth and P. Roe, “Divergence- and Curl-Preserving Prolongation and Restriction Formulas”, *J. Comput. Phys.* **180**, 736–750 (2002).
[doi:10.1006/jcph.2002.7120](https://doi.org/10.1006/jcph.2002.7120).
- [63] O. Buneman, “Time reversible difference procedures”, *J. Comput. Phys.* **1**, 517–535 (1967).
[doi:10.1016/0021-9991\(67\)90056-3](https://doi.org/10.1016/0021-9991(67)90056-3).
- [64] J. Boris, “Relativistic Plasma Simulation - Optimization of a Hybrid Code”, in Proc. 4th Conf. Num. Sim. Plasmas, 3–67 (1970).
<http://www.dtic.mil/cgi-bin/GetTRDoc?AD=ADA023511>.
- [65] E. Hairer, C. Lubich and G. Wanner, “Geometric Numerical Integration” (Springer, Berlin, 2006), ISBN: 3-540-30663-3.
- [66] M. Toggweiler et al., “A novel adaptive time stepping variant of the Boris-Buneman integrator for the simulation of particle accelerators with space charge”, ArXiv, 1211.3664 (2012).
<http://arxiv.org/abs/1211.3664>.
- [67] R. Wirz, “Discharge plasma processes of ring-cusp ion thrusters”, PhD thesis (Californian Institute of Technology, 2005).
http://thesis.library.caltech.edu/1974/1/Wirz_Thesis.pdf.
- [68] W. Oevel and M. Sofroniou, “Symplectic Runge-Kutta Schemes II: Classification of Symmetric Methods”, tech. rep. (1997).
- [69] H.-S. Mao and R. Wirz, “Comparison of Charged Particle Tracking Methods for Non-Uniform Magnetic Fields”, in 42nd AIAA Plasmadynamics and Lasers Converence, 2011–3739 (2011).
<http://www.wirz.seas.ucla.edu/pdf/pub57.pdf>.
- [70] B. Marder, “A method for incorporating Gauss’ law into electromagnetic PIC codes”, *J. Comput. Phys.* **68**, 48–55 (1987).
[doi:10.1016/0021-9991\(87\)90043-X](https://doi.org/10.1016/0021-9991(87)90043-X).
- [71] A. Langdon, “On enforcing Gauss’ law in electromagnetic particle-in-cell codes”, *Comput. Phys. Commun.* **70**, 447–450 (1992).
[doi:10.1016/0010-4655\(92\)90105-8](https://doi.org/10.1016/0010-4655(92)90105-8).
- [72] O. Buneman, “Fast Numerical Procedures for Computer Experiments on Relativistic Plasmas”, in *Relativistic Plasmas*, 205–233 (1968).
- [73] J. Villasenor and O. Buneman, “Rigorous charge conservation for local electromagnetic field solvers”, *Comput. Phys. Commun.* **69**, 306–316 (1992).
[doi:10.1016/0010-4655\(92\)90169-Y](https://doi.org/10.1016/0010-4655(92)90169-Y).
- [74] R. Morse and C. Nielson, “Numerical Simulation of the Weibel Instability in One and Two Dimensions”, *Phys. Fluids* **14**, 830–840 (1971).
[doi:10.1063/1.1693518](https://doi.org/10.1063/1.1693518).

- [75] T. Umeda et al., “A new charge conservation method in electromagnetic particle-in-cell simulations”, *Comput. Phys. Commun.* **156**, 73–85 (2003).
[doi:10.1016/S0010-4655\(03\)00437-5](https://doi.org/10.1016/S0010-4655(03)00437-5).
- [76] R. Barthélémy, “Le problème de conservation de la charge dans le couplage des équations de Vlasov et de Maxwell”, PhD thesis (Université Louis Pasteur, Strasbourg, 2005).
<http://scd-theses.u-strasbg.fr/998/01/barthelme.pdf>.
- [77] T. Esirkepov, “Exact charge conservation scheme for Particle-in-Cell simulation with an arbitrary form-factor”, *Comput. Phys. Commun.* **135**, 144–153 (2001).
[doi:10.1016/S0010-4655\(00\)00228-9](https://doi.org/10.1016/S0010-4655(00)00228-9).
- [78] T. Pointon, “Second-order, exact charge conservation for electromagnetic particle-in-cell simulation in complex geometry”, *Comput. Phys. Commun.* **179**, 535–544 (2008).
[doi:10.1016/j.cpc.2008.04.017](https://doi.org/10.1016/j.cpc.2008.04.017).
- [79] A. Taflove and S. C. Hagness, “Computational Electrodynamics: The Finite Difference Time Domain Method”, 3rd ed. (Artech House, Norwood, MA, 2005), ISBN: 978-1580538329.
- [80] A. Taflove and M. E. Brodwin, “Numerical Solution of Steady-State Electromagnetic Scattering Problems Using the Time-Dependent Maxwell’s Equations”, *IEEE Trans. Microw. Theory Tech.* **23**, 623–630 (1975).
[doi:10.1109/TMTT.1975.1128640](https://doi.org/10.1109/TMTT.1975.1128640).
- [81] A. D. Greenwood et al., “On the Elimination of Numerical Cerenkov Radiation in PIC Simulations”, *J. Comput. Phys.* **201**, 665–684 (2004).
[doi:10.1016/j.jcp.2004.06.021](https://doi.org/10.1016/j.jcp.2004.06.021).
- [82] J.-L. Vay et al., “Numerical methods for instability mitigation in the modeling of laser wakefield accelerators in a Lorentz-boosted frame”, *J. Comput. Phys.* **230**, 5908–5929 (2011).
[doi:10.1016/j.jcp.2011.04.003](https://doi.org/10.1016/j.jcp.2011.04.003).
- [83] R. Hampel, I. Zagorodnov and T. Weiland, “New Discretization Scheme for Wake Field Computation in Cylindrically Symmetric Structures”, in Proceedings of EPAC, THPLT036 (2004).
<http://accelconf.web.cern.ch/AccelConf/e04/PAPERS/THPLT036.PDF>.
- [84] J. Juntunen and T. Tsiboukis, “Reduction of numerical dispersion in FDTD method through artificial anisotropy”, *IEEE Trans. Microw. Theory Tech.* **48**, 582–588 (2000).
[doi:10.1109/22.842030](https://doi.org/10.1109/22.842030).
- [85] B. Finkelstein and R. Kastner, “Finite difference time domain dispersion reduction schemes”, *J. Comput. Phys.* **221**, 422–438 (2007).
[doi:10.1016/j.jcp.2006.06.016](https://doi.org/10.1016/j.jcp.2006.06.016).
- [86] T. Namiki, “A New FDTD Algorithm Based on Alternating-Direction Implicit Method”, *IEEE Trans. Microw. Theory Tech.* **47**, 2003–2007 (1999).
[doi:10.1109/22.795075](https://doi.org/10.1109/22.795075).

- [87] F. Zheng, Z. Chen and J. Zhang, “Toward the Development of a Three-Dimensional Unconditionally Stable Finite-Difference Time-Domain Method”, *IEEE Trans. Microw. Theory Tech.* **48**, 1550–1558 (2000).
[doi:10.1109/22.869007](https://doi.org/10.1109/22.869007).
- [88] D. W. Peaceman and H. H. Rachford, “The Numerical Solution of Parabolic and Elliptic Differential Equations”, *SIAM J. Appl. Math.* **3**, 28–41 (1955).
[doi:10.1137/0103003](https://doi.org/10.1137/0103003).
- [89] H. H. Wang, “A Parallel Method for Tridiagonal Equations”, *ACM Trans. Math. Soft.* **7**, 170–183 (1981).
[doi:10.1145/355945.355947](https://doi.org/10.1145/355945.355947).
- [90] S. Bondeli, “Divide and conquer: a parallel algorithm for the solution of a tridiagonal linear system of equations”, *Parallel Computing* **17**, 419–434 (1991).
[doi:10.1016/S0167-8191\(05\)80145-0](https://doi.org/10.1016/S0167-8191(05)80145-0).
- [91] X.-H. Sun, H. Zhang and L. M. Ni, “Efficient tridiagonal solvers on multicomputers”, *IEEE Trans. Comput.* **41**, 286–296 (1992).
[doi:10.1109/12.127441](https://doi.org/10.1109/12.127441).
- [92] T. M. Austin, M. Berndt and J. D. Moulton, “A memory Efficient Parallel Tridiagonal Solver”, *tech. rep. LA-UR 03-4149* (2004).
- [93] L. Yuan, H. Guo and Z. Yin, “On optimal message vector length for block single parallel partition algorithm in a three-dimensional ADI solver”, *Appl. Math. Comput.* **215**, 2565–2577 (2009).
[doi:10.1016/j.amc.2009.08.052](https://doi.org/10.1016/j.amc.2009.08.052).
- [94] F. Zheng and Z. Chen, “Numerical Dispersion Analysis of the Unconditionally Stable 3-D ADI-FDTD Method”, *IEEE Trans. Microw. Theory Tech.* **49**, 1006–1009 (2001).
[doi:10.1109/22.920165](https://doi.org/10.1109/22.920165).
- [95] A. P. Zhao, “Improvement on the Numerical Dispersion of 2-D ADI-FDTD with Artificial Anisotropy”, *IEEE Microw. Wirel. Compon. Lett.* **14**, 292–294 (2004).
[doi:10.1109/LMWC.2004.828002](https://doi.org/10.1109/LMWC.2004.828002).
- [96] N. V. Kantartzis, T. T. Zygiridis and T. D. Tsiboukis, “An Unconditionally Stable Higher Order ADI-FDTD Technique for the Dispersionless Analysis of Generalized 3-D EMC Structures”, *IEEE Trans. Magn.* **40**, 1436–1439 (2004).
[doi:10.1109/TMAG.2004.825289](https://doi.org/10.1109/TMAG.2004.825289).
- [97] M. Darms et al., “Dispersion and Asymmetry Effects of the ADI-FDTD Method”, *IEEE Microw. Wirel. Compon. Lett.* **12**, 491–493 (2002).
[doi:10.1109/LMWC.2002.805951](https://doi.org/10.1109/LMWC.2002.805951).
- [98] S. Garcia, T. Lee and S. Hagness, “On the Accuracy of the ADI-FDTD Method”, *IEEE Antennas Wirel. Propag. Lett.* **1**, 31–34 (2002).
[doi:10.1109/LAWP.2002.802583](https://doi.org/10.1109/LAWP.2002.802583).
- [99] D. N. Smithe, J. R. Cary and J. A. Carlsson, “Divergence preservation in the ADI algorithms for electromagnetics”, *J. Comput. Phys.* **228**, 7289–7299 (2009).
[doi:10.1016/j.jcp.2009.06.025](https://doi.org/10.1016/j.jcp.2009.06.025).

- [100] S. Kurz, “Lectures on: Relativistic Electrodynamics: Modelling and Simulation”, V0.5, ETH Zürich (2009).
- [101] I. Zagorodnov and T. Weiland, “TE/TM scheme for computation of electromagnetic fields in accelerators”, *J. Comput. Phys.* **207**, 69–91 (2005).
[doi:10.1016/j.jcp.2005.01.003](https://doi.org/10.1016/j.jcp.2005.01.003).
- [102] A. Cangellaris and D. Wright, “Analysis of the numerical error caused by the stair-stepped approximation of a conducting boundary in FDTD simulations of electromagnetic phenomena”, *IEEE Trans. Antennas Propag.* **39**, 1518–1525 (1991).
[doi:10.1109/8.97384](https://doi.org/10.1109/8.97384).
- [103] R. Holland, “Pitfalls of staircase meshing”, *IEEE Trans. Electromagn. Compat.* **35**, 434–439 (1993).
[doi:10.1109/15.247856](https://doi.org/10.1109/15.247856).
- [104] S. Dey and R. Mittra, “A Locally Conformal Finite-Difference Time-Domain (FDTD) Algorithm for Modeling Three-Dimensional Perfectly Conducting Objects”, *IEEE Microw. Guided Wave Lett.* **7**, 273–275 (1997).
[doi:10.1109/75.622536](https://doi.org/10.1109/75.622536).
- [105] I. Zagorodnov, R. Schumann and T. Weiland, “A Uniformly Stable Conformal FDTD-Method in Cartesian Grids”, *Int. J. Numer. Model.* **16**, 127–141 (2003).
[doi:10.1002/jnm.488](https://doi.org/10.1002/jnm.488).
- [106] T. Weiland, “Eine Methode zur Lösung der Maxwellschen Gleichungen für sechskomponentige Felder auf diskreter Basis”, *Electronic and Communication (AEÜ)* **31**, 116–120 (1977).
- [107] I. Zagorodnov, R. Schuhmann and T. Weiland, “Conformal FDTD-methods to avoid time step reduction with and without cell enlargement”, *J. Comput. Phys.* **225**, 1493–1507 (2007).
[doi:10.1016/j.jcp.2007.02.002](https://doi.org/10.1016/j.jcp.2007.02.002).
- [108] J.-P. Berenger, “A Perfectly Matched Layer for the Absorption of Electromagnetic Waves”, *J. Comput. Phys.* **114**, 185–200 (1994).
[doi:10.1006/jcph.1994.1159](https://doi.org/10.1006/jcph.1994.1159).
- [109] J.-P. Berenger, “Three-Dimensional Perfectly Matched Layer for the Absorption of Electromagnetic Waves”, *J. Comput. Phys.* **127**, 363–379 (1996).
[doi:10.1006/jcph.1996.0181](https://doi.org/10.1006/jcph.1996.0181).
- [110] G. Liu and S. D. Gedney, “Perfectly Matched Layer Media for an Unconditionally Stable Three-Dimensional ADI-FDTD Method”, *IEEE Microw. Guided Wave Lett.* **10**, 261–263 (2000).
[doi:10.1109/75.856982](https://doi.org/10.1109/75.856982).
- [111] S. Wang and F. L. Teixeira, “An Efficient PML Implementation for the ADI-FDTD Method”, *IEEE Microw. Wirel. Compon. Lett.* **13**, 72–74 (2003).
[doi:10.1109/LMWC.2003.808705](https://doi.org/10.1109/LMWC.2003.808705).

- [112] C. Kraus, A. Adelmann and P. Arbenz, “Perfectly matched layers in a divergence preserving ADI scheme for electromagnetics”, J. Comput. Phys. **231**, 39–44 (2012).
[doi:10.1016/j.jcp.2011.08.016](https://doi.org/10.1016/j.jcp.2011.08.016).
- [113] J. Schneider et al., *ToyFDTD, The If-I-Can-Do-It-You-Can-Do-It FDTD*, (Feb. 17, 2014)
<http://dougneubauer.com/wp-content/uploads/wdata/toyfdtd/toyfdtd.html>.
- [114] M. Heroux et al., “An Overview of Trilinos”, tech. rep. SAND2003-2927 (2003).
<http://trilinos.sandia.gov/TrilinosOverview.pdf>.
- [115] M. Gee et al., “ML 5.0 Smoothed Aggregation User’s Guide”, tech. rep. SAND2006-2649 (2006).
<http://trilinos.sandia.gov/packages/ml/mlguide5.pdf>.
- [116] D. Gregor and M. Troyer, *Message Passing Interface library, for use in distributed-memory parallel application programming*, (Feb. 20, 2014)
http://www.boost.org/doc/libs/1_55_0/libs/mpi/.
- [117] M. Smoot, *Templatized C++ Command Line Parser Manual*, (Feb. 20, 2014)
<http://tclap.sourceforge.net/manual.html>.
- [118] M. Howison et al., “H5hut: A High-Performance I/O Library for Particle-based Simulations”, in IEEE International Conference on Cluster Computing Workshops and Posters, 1–8 (2010).
[doi:10.1109/CLUSTERWKSP.2010.5613098](https://doi.org/10.1109/CLUSTERWKSP.2010.5613098).
- [119] M. Galassi et al., “GNU Scientific Library”, version 1.16, GNU (2013).
<http://www.gnu.org/software/gsl/manual/gsl-ref.ps.gz>.
- [120] S. J. Plimpton et al., “A load-balancing algorithm for a parallel electromagnetic particle-in-cell code”, Comput. Phys. Commun. **152**, 227–241 (2003).
[doi:10.1016/S0010-4655\(02\)00795-6](https://doi.org/10.1016/S0010-4655(02)00795-6).
- [121] H. Nakashima et al., “OhHelp: A Scalable Domain-Decomposing Dynamic Load Balancing for Particle-In-Cell Simulations”, in Proceedings of ICS, 90–99 (2009).
[doi:10.1145/1542275.1542293](https://doi.org/10.1145/1542275.1542293).
- [122] J. Blinn, “Floating-Point Tricks”, IEEE Comput. Graph. Appl. **17**, 80–84 (1997).
[doi:10.1109/38.595279](https://doi.org/10.1109/38.595279).
- [123] C. Lomont, *Fast inverse square root*, (Feb. 25, 2014)
<http://www.lomont.org/Math/Papers/2003/InvSqrt.pdf>.
- [124] id Software, *Quake III Arena*, (Sept. 11, 2014)
<ftp://ftp.idsoftware.com/idstuff/source/quake3-1.32b-source.zip>.
- [125] K. Bowers, “Accelerating a Particle-in-Cell Simulation Using a Hybrid Counting Sort”, J. Comput. Phys. **173**, 393–411 (2001).
[doi:10.1006/jcph.2001.6851](https://doi.org/10.1006/jcph.2001.6851).
- [126] Kitware Inc., “VTK File Formats”, version 4.2, Kitware Inc. (2003).
<http://www.vtk.org/VTK/img/file-formats.pdf>.

- [127] Department of Energy Advanced Simulation and Computing Initiative, *VisIt Visualization Tool*, (Feb. 26, 2014)
<https://wci.llnl.gov/codes/visit/home.html>.
- [128] Kitware Inc., *ParaView - Open Source Scientific Visualization*, (Feb. 26, 2014)
<http://www.paraview.org/>.
- [129] M. Borland, “A Universal Postprocessing Toolkit for Accelerator Simulation and Data Analysis”, in Proceedings of ICAP, FTU10 (1998).
<http://www.slac.stanford.edu/econf/C980914/papers/F-Tu10.pdf>.
- [130] J.-L. Vay, J.-C. Adam and A. Héron, “Asymmetric PML for the absorption of waves. Application to mesh refinement in electromagnetic Particle-In-Cell plasma simulations”, *Comput. Phys. Commun.* **164**, 171–177 (2004).
<doi:10.1016/j.cpc.2004.06.026>.
- [131] B. Donderici and F. Teixeira, “Improved FDTD subgridding algorithms via digital filtering and domain overriding”, *IEEE Trans. Antennas Propag.* **53**, 2938–2951 (2005).
<doi:10.1109/TAP.2005.854558>.